DISS. ETH NO 17350

EXTRACTION OF ULTRACOLD NEUTRONS FROM A SOLID DEUTERIUM SOURCE

A dissertation submitted to the

ETH ZÜRICH

for the degree of

Doctor of Sciences

presented by

TOMASZ BRYŚ

Master of Science, Jagiellonian University, Kraków, Poland

Diploma Engineer, University of Science and Technology, Kraków, Poland

born 13.12.1973

citizen of Poland

accepted on the recomendation of

Prof. Dr. Alexander Wokaun, examiner
Prof. Dr. Kazimierz Bodek, co-examiner
Prof. Dr. Urs Langenegger, co-examiner
Dr. Klaus Kirch, co-examiner

2007

Contents

Abstract

Ultracold neutrons (UCN) are a powerful tool to test physics beyond the Standard Model of particle physics, as well as for fundamental properties of the neutron, surface sciences and biological studies. As current experiments using UCN are limited by the low available intensities and densities (typically less then 40 cm^{-3}), over the last few years increased efforts have been made to built more powerful sources of UCN. At the Paul Scherrer Institut (PSI), a new source with orders of magnitude higher intensity is under construction, using solid Deuterium (sD$_2$) as a material to convert thermal neutrons to UCN energies ($\leqslant$ 250 neV), based on a pulsed spallation neutron source. While the energy conversion part is well understood, the efficiency of neutron extraction from sD$_2$ is needed to be investigated. In this work, the effects of crystal quality and repeated thermal stress of crystalline sD$_2$ have been measured for different ranges of incident neutron energies. These measurements provide crucial information for the specific thermal operating conditions as well as the neutron scattering distribution. It allows better understanding of observed discrepancies between theory and measured total cross section for UCN scattering on sD$_2$ at 5 K.

Three experiments to investigate energy dependent scattering of neutrons on sD$_2$ crystals have been carried out using cold neutrons ($\lambda = 5 \div 36$ Å) at the instrument SANS I at PSI, very cold neutrons ($\lambda = 20 \div 120$ Å) and ultracold neutrons ($\lambda = 100 \div 600$ Å) at the instrument PF2 at ILL, Grenoble. All three experiments used position sensitive detectors. Either velocity selection or a time of flight method was employed to measure wavelength-dependence. For the case of cold neutrons, the observed scattering behavior is best described with small angle scattering (SANS) in the so-called Porod-approximation, where the momentum transfer $Q \to \infty$. The experiment using very cold neutrons confirms these results, however, with much lower accuracy due to larger systematic effects. In the UCN regime, the Porod approximation alone cannot properly describe the observed scattering behavior and an additional wavelength-independent cross section parameter has to be added. This cross section originates from cracks in the sD$_2$ crystal structure.

Due to their low energies, UCN can be totally reflected from cracks and so can be isotropically scattered. In addition to the measurements at static temperatures, the sample temperature was very fast cycled between 5-10-5 K and 5-18-5 K, simulating pulsed operation of the PSI UCN source under different conditions. The observed behavior can be well described using a combination of the Porod approximation, with $P_c = (3.94 \pm 1.05) \cdot 10^{21} \mathrm{cm}^{-5}$ and the crack-scattering model with $I_c = (11.76 \pm 0.38)$ barn.

Based on these results, a detailed Monte Carlo simulation model of the sD_2 source using (i) absorption on Deuterium and Hydrogen contaminations, (ii) thermal up-scattering, (iii) incoherent scattering, (iv) small angle scattering, (v) para-Deuterium up-scattering and (vi) additional scattering on crystal cracks has been built. The model allows simulation of UCN extraction from solid Deuterium in the pulsed PSI UCN source.

Zusammenfassung

Ultrakalte Neutronen (UCN) bieten die Möglichkeit physikalische Theorien jenseits des Standard Modells zu testen, die fundamentalen Eigenschaften des Neutrons zu untersuchen, sowie Oberflächenphysik oder biologische Studien zu betreiben. Da derzeitige UCN-Experimente durch die kleinen Intensitäten und Dichten (typischerweise kleiner als 40 cm^{-3}) beschränkt sind, wurde in den letzten Jahren der Bau neuer intensiverer UCN Quellen stark vorangetrieben. Am Paul Scherrer Institut (PSI) entsteht eine UCN-Quelle, mit um Grössenordnungen höheren UCN-Dichten, in der Neutronen durch Spallation erzeugt, in D_2O moderiert und anschliessend mittels festem Deuterium (sD_2) in den UCN-Energiebereich gestreut ($\leqslant 250$ neV) werden. Die Streuung thermischer und kalter Neutronen in den ultrakalten Energiebereich ist gut verstanden, doch die Extraktion der UCN aus dem sD_2 Kristall benötigte eine Untersuchung. In der vorliegenden Arbeit wurde die Kristallqualität des kristallinen sD_2 unter Einfluss thermischer Belastung für verschiedene Neutronenenergien untersucht. Diese Messungen liefern wichtige Informationen zu den thermischen Betribsbedingungen und geben auf Aufschluss über die Neutronenstreuverteilungen. Desweiteren tragen sie zum besseren Verständnis der experimentellen und theoretischen Streuquerschnitte von sD_2 bei 5 K bei.

Drei Experimente zur energieabhängigen Streuung von Neutronen in sD_2 wurden durchgeführt. Für kalte Neutronen ($\lambda = 5 \div 36$ Å) wurde das SANS I Instrument am PSI genutzt, für sehr kalte Neutronen (VCN) ($\lambda = 20 \div 120$ Å) und ultrakalte Neutronen ($\lambda = 100 \div 600$ Å) wurde das PF2 am ILL, Grenoble, genutzt. In allen Experimenten wurden ortsauflösende Detektoren verwendet. Die Wellenlängenabhängigkeit wurde entweder durch Geschwindigkeitsselektion oder Flugzeitmessung untersucht. Für kalte Neutronen wird das beobachtete Streuverhalten am besten durch die Porod-Näherung der Kleinwinkelstreuung mit $Q \to \infty$ beschrieben. Diese Beobachtung wurde mit VCN bestätigt, wobei die Genauigkeit der Messung kleiner war und es grössere systematische Unsicherheiten gab. Im Bereich von ultrakalten Neutronen können die Daten nicht alleine durch die Porod-Näherung

beschrieben werden; zusätzlich muss ein wellenlängenunabhängiger Wirkungs-querschnitt addiert werden, der durch Risse im D_2-Kristall verursacht wird. Aufgrund ihrer geringen Energie werden UCN an diesen Rissen total reflektiert, was, gemittelt über den Kristall, zu einer isotropen Streuung führt. Zusätzlich zu den Messungen bei konstanten Temperatur wurde der Einfluss von Temperaturzyklen, 5-10-5 K und 5-18-5 K, auf das UCN-Streuverhalten untersucht. Das beobachtete Verhalten kann gut durch die Porod-Näherung mit $P = (3.94 \pm 1.05) \cdot 10^{21} \mathrm{cm}^{-5}$ und den isotropen „Riss-Querschnitt" $I_c = (11.76 \pm 0.38)$ barn beschrieben werden.

Basierend auf diesen Resultaten konnten detaillierte Monte Carlo Simulationen durchgeführt werden, bei denen (i) die Absorption an D_2- und H_2-Kontaminationen, (ii) thermisches Up-Scattering, (iii) inkohärente Streuung, (iv) Kleinwinkelstreuung, (v) para-D_2-Up-Scattering und (vi) die Streuung an Rissen im D_2 berücksichtigt werden. Dies erlaubt die Simulation der Extraktion von UCN aus dem sD_2 der gepulsten PSI UCN-Quelle.

List of abbraviations and symbols

Table 1: List of abbreviations

Abbreviation	
ADC	Analog-to-Digital Converter
ASCII	American Standard Code for Information Interchange
CCD	Charge-Coupled Device - synonym for a type of image sensor
CN	Cold Neutrons
CP	Charge and Parity symmetry
DAC	Digital-to-Analog Converter
DLC	Diamond-Like Carbon
EDM	Electric Dipole Moment of Neutron
F1, F2	fiber optic
FPGA	Field-Programmable Gate Array
FWHM	Full Width at Half Maximum
Geant4	GEometry ANd Tracking (Monte Carlo methods of simulation particles through matter)
GPIB	General Purpose Interface Bus
GUI	Graphical user interface
I/O	Input-Output
ISA	Industry Standard Architecture
L1, L2, L3, L4	optics and support in the laser head
LPT	Line PrinTer (parallel port interface)
mfp	Mean Free Path
MC	Monte Carlo
MSCB	Midas Slow Control Bus
MSGC	Micro-Strip Gas Counter
OFHC	Oxygen Free High Conductivity
PC	Personal Computer
PCI	Peripheral Component Interconnect

Abbreviation	
PID	Proportional-Integral-Derivative controller
PSF	Point Spread Function
R1, R2, R3, R4	optics and support in the Raman collector
RAID	Redundant Array of Independent Drives (or disks) - data storage schemes that divide and/or replicate data among multiple hard disks
RMS	Root Mean Square
ROOT	object-oriented software package
S1, S2, S3	optics and support in the spectrometer coupling
SANS	Small Angle Neutron Scattering
SANS I	Small Angle Neutron Scattering Instrument at PSI
SC	Slow Control
sD_2	solid Deuterium
SLR	Single Lens Reflex camera (ger. Spiegelreflexkamera)
SM	Standard Model
SUSY	SUper-SYmmetry model
TOF	Time-Of-Flight
TTL	Transistor-Transistor Logic (type of digital logic-gate circuits)
UBS	Upper-Bound Spectrum Algorithm
USB	Universal Serial Bus
UCN	UltraCold Neutrons
VCN	Very Cold Neutrons

Chapter 1

Introduction

Three experiments to measure transmission and scattering cross sections of cold neutrons (CN), very cold neutrons (VCN) and ultracold neutrons (UCN) on solid Deuterium have been performed. The goal was to grow Deuterium crystals of high quality and measure cross sections as a function of temperature, and their structure. These parameters fix the lifetime (τ_{UCN}) and mean free path (mfp) of UCN in Deuterium and are essential data for estimation of the density of UCN in the new source being built at PSI [1, 2]. This thesis will concentrate on small angle neutron scattering (SANS) on solid Deuterium, thermal stress analysis and a simulation performed on a model of the extraction of UCN from solid Deuterium (sD_2) under different conditions.

1.1   Ultracold neutrons

Ultracold neutrons are neutrons with very low kinetic energy. Usually the energy is defined as being smaller than the effective strong interaction potential V_F (Fermi potential) of Beryllium, which is equal to 258 neV. Because of their low kinetic energy, UCN are strongly affected by gravity; the potential energy for a neutron per meter in height is 102.57 neV. UCN have a magnetic moment and interact with magnetic fields. The interaction is defined by the scalar product of the spin of the neutron with the field vector and corresponds to an energy of $\pm$ 60.31 neV/T. When UCN reach the surface of a material with energy less than its Fermi potential they will be reflected under any angle of incidence. The reflecting properties together with gravity and magnetic fields led to the idea of building traps for UCN, in which they can be stored for a long time. The UCN, with a long observation time can be used as an excellent probe for studying fundamental physics. However,

many experiments are limited by the available density of UCN.

In UCN physics, it is often convenient to use temperature, velocity, momentum, wavevector wavelength, or height to which UCN can rise as a alternative to energy. The equations below show the applicable relation:

$$E = k_B T = \frac{mv^2}{2} = \frac{p^2}{2m} = \frac{\hbar^2 k^2}{2m} = \frac{h^2}{2m\lambda^2} = mgH \qquad (1.1)$$

Inserting the values for the neutron mass $m = 1.675 \cdot 10^{-27}$ kg, the Boltzmann constant $k_B = 1.381 \cdot 10^{-23}$ J/K and the Planck constant $h = 6.626 \cdot 10^{-34}$ Js, standard gravitational acceleration $g_n = 9.81$ m/s^{-2} the following useful relation can be obtained:

$$E = 0.08617T = 5.227v^2 = 2.072k^2 = 81.81\frac{1}{\lambda^2} = 10.26 \cdot 10^{-5}H \qquad (1.2)$$

where E is energy in millielectronvolt, T is temperature in Kelvin, v is velocity in kilometer per second, k is the wavevector in Angstroem^{-1} and λ the wavelength in Angstroem. The equation with temperature gives the neutron classification for "hot"($T \simeq 2000$ K), "thermal" ($T \simeq 300$ K), "cold" ($T \simeq 30$ K) and "ultracold" ($T \simeq$ millikelvin). Hence UCN being neutrons with an energy of less than 300 neV, they have temperatures of a few millikelvin, a velocity of less than 6.8 m/s, and a wavelength of more than 600 Å.

1.2   UCN sources

The conventional method for obtaining UCN is to extract them via a neutron guide from a cold source placed inside a reactor. The velocity spectrum of neutrons in the cold source is similar to a Maxwell distribution. There will be a small fraction of UCN in the low energy tail of the spectrum. The spectrum of neutrons in thermal equilibrium with a moderator at temperature T_0 is given by:

$$\rho(v)dv = \frac{2\Phi_0}{\alpha} \frac{v^2}{\alpha^2} \exp\left(-\frac{v^2}{\alpha^2}\right)\frac{dv}{\alpha}, \qquad (1.3)$$

where Φ_0 is the total neutron flux and $\alpha = \sqrt{2k_B T_0/m}$ is the mean velocity. Integration of the Eq. (1.3) for the energies between zero and the critical velocity $v_c = \sqrt{2V_F/m}$, corresponding to the Fermi potential V_F, gives the maximum UCN density:

$$\rho_{UCN} = \int_0^{v_c} \rho(v)dv = \frac{2}{3}\frac{\Phi_0}{\alpha}\left(\frac{V_F}{k_B T_0}\right)^{\frac{3}{2}} \qquad (1.4)$$

2

Methods to increase the UCN yield from a cold neutron source include vertical extraction [3], using gravity to decelerate neutrons of higher velocities into the UCN regime; and mechanical deceleration [4], using collisions of neutrons with a moving scatterer. The UCN production methods mentioned above are limited according to Liouville's theorem. This means that any energy transformations carried out on a beam of neutrons (gravity or reflection) cannot increase the phase space density above its value in the primary source moderator [5]. An alternative UCN production is based on the conversion of cold neutrons into UCN in cold converter materials like superfluid helium (^{4}He) [6] or solid Deuterium (sD$_2$) [7, 8]. Solid D$_2$ has the potential to produce high UCN intensities at densities of about $10^3 - 10^4$ cm^{-3} [9]. This is two orders of magnitude more than the currently most intense source at the Institut Laue-Langevin. A pulsed spallation ultracold neutron source with sD$_2$ as a converter material is being built at the Paul Scherrer Institut.

1.2.1   The PSI UCN source

A detailed description of the source can be found in Ref. [1, 2]. A diagram of the source is shown in Fig. 1.1 and some basic information is given below. Fast neutrons are produced by a short pulse of the high intensity proton beam (590 MeV, $I_p \geq 2$ mA) onto a spallation target. The proton beam will be operated on a 1% duty cycle, e.g. with an 8 s long beam pulse every 800 s. On average, one proton produces $\sim$11 neutrons. Neutrons from the spallation target are slowed down to thermal energies in the heavy water (D$_2$O) moderator. In addition to neutron moderation, D$_2$O also provides a very effective shielding of the sD$_2$ against an excessively large power deposition during a proton beam pulse. Fast neutrons produced in the spallation target have energies of the order of 2 MeV. They can be efficiently moderated with elastic scattering in light materials (like Deuterium), where a neutron dissipates its energy through multiple collisions and comes to thermal equilibrium, e.g for heavy water after about 35 collisions [10]. The resultant energy spectrum is described by a Maxwell-Boltzmann distribution with neutron energies around 25 meV (T$_{D_2O} \approx$ 300 K). Thermal neutrons are further cooled inside the solid ortho-D$_2$ and can be downscattered into the UCN regime by phonon creation [11, 7]. The phonons are permanently "pumped" away by a cooling machine. The reverse process, up-scattering, is also possible but the probability depends on the phonon density and thus on the temperature of the converter. At low temperature the probability is suppressed. The cross section for gaining energy due to up-scattering is determined by the detailed
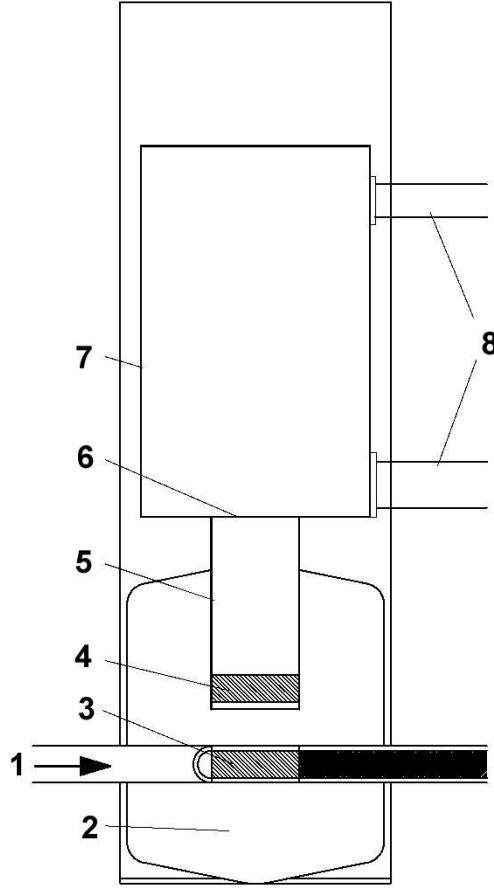
Figure 1.1: The diagram of the PSI UCN source; 1-proton beam; 2-heavy water moderator; 3-lead spallation target; 4-UCN converter at 5K; 5-vertical neutron guide; 6-UCN shutter, closed for storage, open for production; 7-UCN storage volume; 8-neutrons guides to the experiments. The total height of the setup is about 6m.

balance:

$$\sigma_{up} = \frac{E_{UCN} + \Delta}{E_{UCN}} \cdot \exp\left(-\frac{\Delta}{k_B T}\right) \cdot \sigma_{down} \qquad (1.5)$$

where Δ is the excitation energy. Finally, UCN are extracted from the solid Deuterium and guided into a large storage volume with a diamond-like carbon (DLC) surface coating.

The principle of a super-thermal sD$_2$ source has been tested at a reactor [12] and at spallation sources [13, 14, 15]. Some useful information concerning the PSI UCN source is collected in Table 1.1.

Table 1.1: Some important values for the UCN source taken from [15, 2], *values from [13]

spallation process	proton current	2 mA
	proton energy in pulse	590 MeV
	target material	Pb [16]
	temperature of the target	300 K
	neutrons per proton	~11
	fast neutron energy	~ MeV
	pulse length (1% duty cycle)	4 - 8 s
	time between pulses	400 - 800 s
	power deposition in sD$_2$	~ 400 W/mA
D$_2$O moderator	thermal neutron energy	~25 meV
	temperature	300 K
	moderator volume	~3.3 m^3
sD$_2$ converter	converter volume	~0.03 m^3
	temperature	5 - 8 K
	UCN energy	> 100 neV
	UCN lifetime	40 ms*
	UCN density	>3000 cm^{-3}
	UCN mean free path	2 - 8 cm*
storage vessel	storage lifetime	400 - 500 s
	coating material	DLC
	storage volume	~2 m^{-3}

UCN lifetime in solid Deuterium

The limiting UCN density, ρ_{UCN}, is given by the product of the UCN production rate R_p and the lifetime of UCN in the sD$_2$, τ_{UCN}:

$$\rho_{UCN} = R_p \cdot \tau_{UCN} \qquad (1.6)$$

Several effects determine the lifetime of UCN in sD$_2$: up-scattering by phonons [11], up-scattering from para-Deuterium molecules in the sD$_2$ crystal [17], absorption by Deuterium and by Hydrogen impurities (additional losses, e.g. caused by the β-decay of the free neutron, can be neglected). The total lifetime is given by:

$$\frac{1}{\tau_{UCN}} = \frac{1}{\tau_{phonon}} + \frac{1}{\tau_{ortho/para}} + \frac{1}{\tau_{Dabs}} + \frac{1}{\tau_{Habs}} \qquad (1.7)$$

Because the maximum achievable density (see Eq. 1.6) is given by the product of the down-scattering rate and the lifetime of the UCN in the converter [18], it is crucial to maximize the neutron lifetime in the Deuterium.

5

In order to minimize losses due to upscattering (see Eq. 1.5) the temperature of the crystal should be kept low (e.g. $\tau_{phonon} = 150\,\text{ms}$ at 4K, $\tau_{phonon} = 40\,\text{ms}$ at 8K [11]).

Neutrons can pick up energy from a D_2 molecule; particularly from any para-D_2 with nuclear spin S=1 and an orbital angular momentum J=1 and transfer the excitation energy of about $7\,\text{meV}$ to the kinetic energy of the neutron $\langle S = 1; J = 1 \rangle \rightarrow \langle S = 0, 2; J = 0 \rangle + 7\,\text{meV}$ (e.g. $\tau_{ortho/para} = 150\,\text{ms}$ for 1% para fraction [17]).

Nuclear absorption of neutrons on deuterons, cannot be avoided. The thermal neutron cross section [19] is $0.519\,\text{mbarn}$ and this gives an absorption time τ_{Dabs} of $150\,\text{ms}$. Contaminants in the Deuterium also lead to losses of UCN which are proportional to their amount. The most important is hydrogen; 0.2% of hydrogen already causes an absorption time τ_{Habs} of $150\,\text{ms}$.

Although $\tau_{UCN} \sim 75\,\text{ms}$ should be achievable (limited by nuclear absorption and temperature up-scattering), the best values obtained so far are around $40\,\text{ms}$ [13].

Mean Free Path

The mean free path (mfp) of UCN in sD_2 is another extremely important issue. The UCN created inside Deuterium could leave the crystal on a straight trajectory see Fig. 1.2 a) or they could scatter many times and finally be absorbed, Fig. 1.2 b). The mfp can be 8 cm at most, which is given by
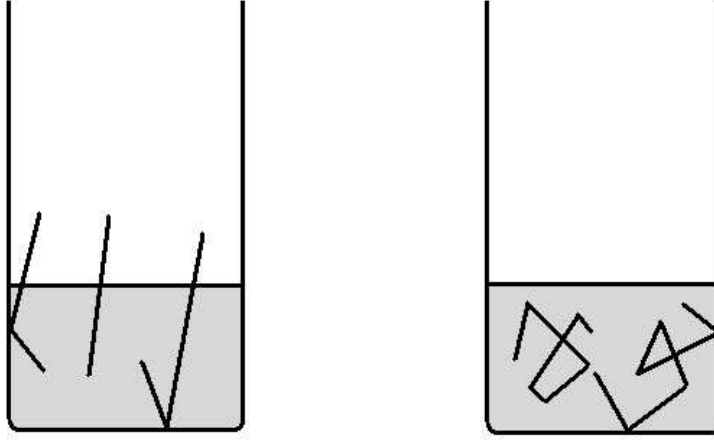
Figure 1.2: The picture shows the part of the PSI UCN source with the Deuterium crystal and the UCN extraction guide. Two different behaviors of UCN are schematically drawn; on the left, UCN can rapidly escape without scattering; on the right, can scatter many times and be absorbed.

the 2 barn incoherent scattering cross section of deuterons. The mfp from experiments in Los Alamos was found to be between 2 and 8 cm [13]. The mfp was not investigated in detail, however, the previous experiments yielded contradictory results whether the mfp strongly depends on the method of freezing [20] or not [21].

Monte Carlo Simulations

A simple Monte Carlo simulation with varying parameters τ_{UCN} and mfp is used to illustrate the difference in UCN numbers obtained from a source. The simulations were performed using the Geant4 and UCN package [22, 23] (see Appendix A) and a simplified geometry of the real UCN source. The
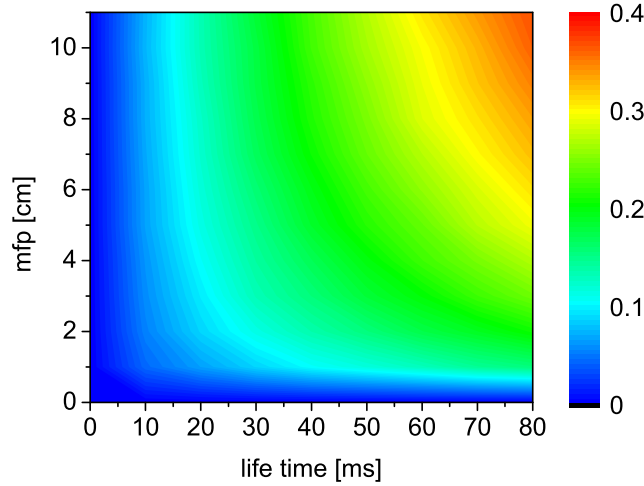
Figure 1.3: The graph shows the ratio between extracted and generated UCN from the solid Deuterium in dependence on mean free path and lifetime for a typical velocity of UCN (5 m/s).

walls and the bottom part of the simulated Deuterium container had ideally reflecting surface. On the top of the container neutrons were counted. The UCN were initially homogeneously distributed inside the Deuterium crystal with a constant velocity of 5 m/s and isotropically distributed. Neutrons could travel inside the crystal and could be scattered, absorbed or detected. The ratio between counted and generated neutrons was calculated as a function of mfp and UCN lifetime. The result is shown in Fig. 1.3. In Fig. 1.4 the cut through this 2-dimensional extraction function is ploted for the UCN life time of 40 ms.

7
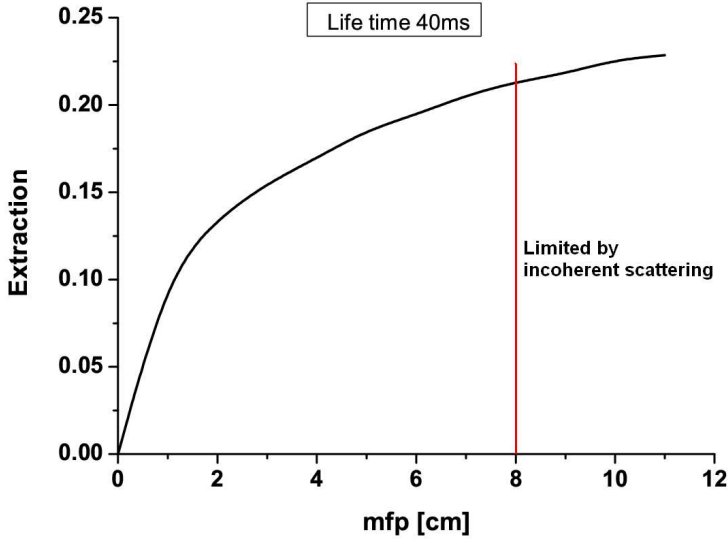
Figure 1.4: The graph shows the cut of the two dimentional extraction function of UCN (see Fig. 1.3) for 40 ms life time of UCN in Deuterium.

In the following, the properties and the behavior of solid Deuterium used as a cold neutron moderator and ultracold converter will be investigated. Special emphasis is made on the measurement of small angle neutron scattering to obtain information about the crystal quality. As a result a model will be developed which will describe the UCN production and extraction out of the solid Deuterium thus providing essential information for the planned PSI UCN source.

1.3 Applications of UCN

The development of a new intensive UCN source gives a tool for studying fundamental physics interactions. UCN are useful because they can be readily stored in material bottles for a relatively long time and can be spin polarized. Additionally, the low velocity of UCN and their interaction with magnetic and gravitational fields allow for many interesting experiments [5, 24].

1.3.1 The Electric Dipole Moment (EDM) of the neutron

After many years of investigation of CP violation and its relation to the excess of matter and antimatter in the Universe one question always remains in

particle physics and astrophysics. The CP violation in the Standard Model (SM) (see e.g. [25]) is too small to explain the observed dominance of matter in the Universe. Therefore, search for additional CP violation arising from particle physics beyond the SM is of great importance. A particularly sensitive probe for CP violation is offered by searches for particle electric dipole moments, in particular the neutron EDM [25].

A nonzero particle EDM violates parity (P) and time (T) symmetry when space or time is inverted. That implies also CP violation assuming CPT conservation. Shapiro [26] and Lushikov et al. [27] suggested that UCN could be used to search for the neutron EDM. A storage experiment could give orders of magnitude higher sensitivity due to a longer interaction time, ($\sim 10^2$ s) and suppresses systematic effect due to non-parallel $\mathbf{E}$ and $\mathbf{B}$ fields. The experiments at PNPI [8] and ILL [28] and the planned experiment at PSI [29] use Ramsey's method of separated oscillatory fields and measure the Larmor frequency of polarised neutrons [30] for parallel and for antiparallel magnetic $\mathbf{B}$ and electric $\mathbf{E}$ fields. In the simplified Hamiltonian of the system:

$$H = -(\mu \cdot \mathbf{B} + d_n \cdot \mathbf{E}) \tag{1.8}$$

where μ and d_n are magnetic and electric dipole moments. The Larmor frequency in the magnetic field is $\omega_L = 2\mu B/\hbar$. If the neutron has an EDM d_n, an electric field E applied parallel to B will produce a shift in this frequency of $\pm 2d_n \cdot E$ where the sign depends on the relative orientation B and E. If the measurement is done twice and E is flipped relative to B, this will produce a shift of $4d_n \cdot E$. One advantage of PSI EDM experiment is the number of polarised UCN used for measurement, taken directly from the high intensity source, which decrease the statistical uncertainties. The big issue is stability and homogeneity of the fields. The ultimate goal of a new experiment at PSI is to improve the sensitivity by about two orders of magnitude while the currently most precise value is $d_n < 2.9 \cdot 10^{-26}$ e·cm [28]. The theoretical prediction of the EDM in the SM is about 10^{-31} e·cm, see e.g. [31], while in Super Symmetry models (SUSY) d_n values between $10^{-25} - 10^{-28}$ e·cm are predicted, see e.g. [31].

9

Chapter 2

Neutron physics

In this chapter the most relevant aspects of interaction of neutrons with matter will be discussed. Full description is available in the literature (e.g. [32, 33, 34, 35, 36, 37]). The theoretical description of neutron scattering in condensed matter usually starts from the interaction of neutrons with a single nucleus and applies this to the scattering on systems of atoms. Usually exact solution of problems cannot be obtained and approximation have to be used (the Born approximation). At the end of the chapter, the Small Angle Neutron Scattering will be discussed with a special emphasis for the limit when the momentum transfer Q of the scattered neutron goes to infinity.

2.1 Neutron interaction with materials

2.1.1 Scattering of neutrons by a single fixed nucleus

The wavelength of thermal, cold and ultra cold neutrons is of the order 10^{-10} - 10^{-7} m [5], and much larger than the range R of the nuclear force (10^{-14} to 10^{-15} m). Thus the potential:

$$V(r) = \begin{cases} V_0 & , \quad r < R \\ 0 & , \quad r > R \end{cases} \tag{2.1}$$

can be used to describe the scattering process.

For slow neutrons with de Broglie wavelength λ satisfying

$$kR = \frac{2\pi R}{\lambda} \ll 1 \tag{2.2}$$

the wavefunction of the scattered neutron for $r > R$ has the form of a spherical wave $\sim \exp(ikr)/r$. For $r < R$, the wavefunction $u = r\psi$ has the form

(for the spherical square-well potential)

$$u \sim A \sin Kr \qquad\qquad K = \sqrt{\frac{2m(E + V_0)}{\hbar^2}} \qquad\qquad (2.3)$$

satisfying the boundary condition $u = 0$ at $r = 0$. In general $KR \gg 1$ so that u makes several oscillations inside the potential well before joining the external wavefunction at $r = R$; thus we can write for the total wavefunction outside the well (incident plane wave $\exp(i\mathbf{k} \cdot \mathbf{r})$ plus scattered wave).

$$\psi = \exp(i\mathbf{k} \cdot \mathbf{r}) + f(\theta)\frac{\exp(ikr)}{r} \qquad\qquad (2.4)$$

where $f(\theta)$ is a scattering amplitude and is determined by the boundary conditions at $r = R$. With condition Eq. (2.2) the scattering is predominantly s wave (orbital angular momentum, $l = 0$). This follows from the small range of the strong interaction with respect to the neutron wavelength. Classically, we can argue that a neutron travelling a distance d from a nucleus will have angular momentum mvd, (m is the neutron mass and v its velocity) and for this to be equal to $\hbar$ (l=1) we require

$$d \sim \hbar/mv = \lambda \qquad\qquad (2.5)$$

where λ is the neutron wavelength. Since λ is much greater than the range of the nuclear forces a neutron travelling a distance λ from the nucleus will not be scattered; thus we have

$$f(\theta) = constant = a \qquad\qquad (2.6)$$

This parameter a can be complex, and the real part may be either positive or negative. The imaginary part of the scattering represents absorption. In general, the scattering length differs not only for each atom but also for each isotope, and furthermore the scattering length depends on the relative orientation of the neutron and nuclear spins. The differential cross section per unit solid angle is

$$\frac{d\sigma}{d\Omega} = |f(\theta)|^2 = a^2 \qquad\qquad (2.7)$$

and

$$\sigma = 4\pi a^2 \qquad\qquad (2.8)$$

2.1.2 Born approximation and "Fermi's golden rule"

This approximate method is applicable when the energy of the incident particle is large in comparison to the potential on which the particle is scattered.

This is applicable to UCN scattering with an additional assumption. For nuclear scattering of slow neutrons the potential is much higher than the energy of the free neutron but the range of nuclear forces is a few orders of magnitude smaller than the wavelength of the scattered neutrons. The neutron is always far from the scattering potential of the nucleus and thus perturbation theory can be used. A potential that is valid for the low energy limit in Born approximation, is referred to as Fermi pseudo-potential:

$$V_F = \frac{2\pi\hbar^2}{m} a\delta(\mathbf{r}).$$
(2.9)

The basic equation for a differential cross section can be written:

$$\left(\frac{d^2\sigma}{d\Omega dE'}\right)_{\lambda\to\lambda'} = \frac{k'}{k} \left|\langle \mathbf{k}'\lambda' | V_F | \mathbf{k}\lambda\rangle\right|^2 \delta(E_\lambda - E_{\lambda'} + E - E')$$
(2.10)

where $\mathbf{k}, \mathbf{k}'$ represent incident and final neutron state, and λ, λ' characterize initial and final state of the target, respectively.

2.1.3 Scattering on a system of atoms

Next consider the scattering from a rigid array of N nuclei. First the scattering amplitude for a free nucleus, a, must be replaced by the scattering amplitude for a bound nucleus, b, in accordance with the formula

$$a \to b = \frac{a(A+1)}{A}$$
(2.11)

where A is the atomic weight of the nucleus. In the Born approximation the scattering amplitude is proportional to the reduced mass of scattered particle and the target. When the neutron is scattered by a free nucleus the reduced mass is $\mu = A/(A+1)$. When the nucleus is bound to the lattice we can assume that its mass becomes infinite so that $\mu = 1$. This leads directly to the result given by Eq. (2.11).

The cross section Eq. (2.10) relates to specific initial and final target states. In general there will be a range of accessible initial states. The weight for the state $|\lambda\rangle$ is denoted by p_λ, and we choose a normalisation

$$\sum_\lambda p_\lambda = 1$$
(2.12)

p_λ is the product of the thermodynamic factor $\exp(-E_\lambda/k_B T)$, where T is the sample temperature, and k_B Boltzman constant. Moreover, if the final states are not selected by some discrimination they will all be observed. The

equation for the double differential cross section evaluate to the expression depending on the initial and final states of the target

$$\left(\frac{d^2\sigma}{d\Omega dE'}\right)_{\lambda\to\lambda'} = \frac{k'}{k}\left(\frac{m}{2\pi\hbar^2}\right)^2 \sum_{\lambda\lambda'} \overline{p_\lambda \left|\langle \mathbf{k}'\lambda' \left|V_F\right| \mathbf{k}\lambda\rangle\right|^2 \delta(E_\lambda - E_{\lambda'} + E - E')}.$$

(2.13)

The horizontal bar in Eq. (2.13) stands for any relevant average not included in the weights p_λ. For example, we do not include in p_λ the distribution of isotopes, the nuclear spin orientation, or the precise position of the nuclei.

As a scatterer potential V_F we put a sum of Fermi's potential originating from all l nuclei in the target:

$$V_F(\mathbf{r}) = \frac{2\pi\hbar^2}{m} \sum_l b_l \, \delta(\mathbf{r} - \mathbf{R}_l)$$

(2.14)

Thus

$$\frac{d^2\sigma}{d\Omega dE'} = \frac{k'}{k} \sum_{\lambda,s} p_\lambda p_s \sum_{\lambda',s'} \overline{\left|\left\langle s'\lambda' \left|\sum_l b_l \exp(i\mathbf{Q}\cdot\mathbf{R}_l)\right| s\lambda\right\rangle\right|^2} \delta(\hbar\omega + E_\lambda - E_{\lambda'})$$

(2.15)

where $|s\rangle |s'\rangle$ labelled the initial and final spin of the neutron, respectively. The matrix element in Eq. (2.15) describes a scattering process in which the neutron transfers the momentum $\hbar\mathbf{Q}$, to the target sample.

2.1.4   Coherent and incoherent scattering

Since the nuclei are rigidly bound, $\exp(i\mathbf{Q}\cdot\mathbf{R}_l)$ in Eq. (2.15) is not an operator and if we have only elastic scattering $E_\lambda = E_{\lambda'}$. It follows that the matrix element in Eq. (2.15) is proportional to

$$\langle \lambda|\lambda'\rangle = \delta_{\lambda,\lambda'}.$$

(2.16)

which means that there is just one term in the sum over $\lambda' = \lambda$. The expression Eq. (2.15) for scattering reduces to

$$\frac{d\sigma}{d\Omega} = \sum_s p_s \sum_{ll'} \exp(i\mathbf{Q}\cdot(\mathbf{R}_l - \mathbf{R}_{l'})) \left\langle s \left|\overline{b_{l'}^* b_l}\right| s\right\rangle$$

(2.17)

The quantity $\overline{b_{l'}^* b_l}$ is the value of $b_{l'}^* b_l$ averaged over random nuclear spin orientations and random isotope distributions. Simplified last equation only

13

for potential which is independent on spin we can write:

$$\frac{d\sigma}{d\Omega} = \sum_{ll'} \exp(i\mathrm{Q} \cdot (\mathrm{R}_l - \mathbf{R}_{l'})) \overline{b_{l'}^* b_l} \qquad (2.18)$$

In general b_l will depend on the isotope composition at the positions $\mathbf{R}_l$ and their nuclear spin. The sum in Eq. (2.18) can be written as a dependence on l

$$\overline{b_{l'}^* b_l} = \left| \overline{b} \right|^2, \qquad l' \neq l \qquad (2.19)$$

$$\overline{b_{l'}^* b_l} = \overline{b^2}, \qquad l' = l$$

and in general form

$$\overline{b_{l'}^* b_l} = \left| \overline{b} \right|^2 + \delta_{ll'}(\overline{b^2} - \left| \overline{b} \right|^2).$$

Substituting the last equation into Eq. (2.18), the cross section can be written as the sum of two parts

$$\frac{d\sigma}{d\Omega} = \left| \overline{b} \right|^2 \sum_{l \neq l'} \exp(i\mathrm{Q} \cdot (\mathbf{R}_l - \mathbf{R}_{l'})) + \sum_{l=1}^{\mathrm{N}} \left(\overline{|\mathrm{b}|^2} \right) \qquad (2.20)$$

where the *coherent cross section* is $(l' \neq l)$

$$\left(\frac{d\sigma}{d\Omega} \right)_{coh} = \left| \overline{b} \right|^2 \left| \sum_l \exp(i\mathrm{Q} \cdot \mathrm{R}_l) \right|^2 \qquad (2.21)$$

and the *incoherent cross section* is $(l' = l)$

$$\left(\frac{d\sigma}{d\Omega} \right)_{incoh} = N \overline{\left| b - \overline{b} \right|^2} \qquad (2.22)$$

with N the number density of molecules.

In the case of coherent scattering there is strong interference between the waves scattered from each nucleus, so strong that we find coherent scattering from a crystal only if strict geometrical conditions are satisfied. In the case of incoherent scattering there is no interference at all, and angular distribution is isotropic. For a real lattice, i.e. a lattice in which the nuclei can move, the description is more complicated.

14

2.2 The correlation function in nuclear scattering

The cross section for neutron scattering can be expressed as a thermal average of operators belonging to the scattering system. The thermal average is known as the *correlation function*. These functions are not only useful for calculating various properties of the scattering system, but also provide insight into the physical significance of the terms that occur in the scattering cross sections. The functions were formulated by Van Hove [38] and provide a general way to describe any system, solid, liquid, or gas where the scattering can be separated into a coherent and an incoherent part.

The differential cross section for a system of N nuclei of the same type and with zero spin is

$$\frac{d^2\sigma}{d\Omega dE'} = b^2 \frac{k'}{k} S(\mathbf{q}, \omega) \tag{2.23}$$

2.3 Small angle neutron scattering

Small angle neutron scattering (SANS) is a technique for the determination of structures on a length scale from a few Angstrom to few hundred Angstrom. The scattering vector is so small that atomic resolution is not obtained and the structure is thus described by a continuous density distribution. The aim of the experiment is to determine this distribution and to relate it to the properties of the system.

The analysis of small angle scattering data is usually done by either model-independent approaches or by direct modeling. The model-independent approach usually consists of a Fourier transformation of the experimental scattering curve, which provides the pair distance distribution function or equivalently the correlation function. For randomly oriented particles the correlation function is the self convolution of the excess scattering length density distribution $\delta\rho(r)$ averaged over all orientations. In the direct modeling methods the model of the system must be known and is fit to the data.

2.3.1 Structure factor and form factor

Important information about particle size and shape, the distribution of sizes of particles, and the strength of interparticle interactions can be extracted from small angle scattering curves. In most cases, the estimation of the particle size depends on the model used.

In the absence of multiple scattering, neglecting incoherent scattering, the measured intensity $I(Q)$ is proportional to the coherent differential scattering cross section, see Eq. (2.21),

$$\frac{d\sigma}{d\Omega} \sim I(Q) = \left| \sum_l b_l \exp(iQ \cdot R_l) \right|^2 \tag{2.24}$$

where the sum is over all the atoms in the sample, the b_l are the scattering lengths of atoms located at r_l from an arbitrary origin, and Q is the scattering vector and has a magnitude

$$Q = \frac{4\pi}{\lambda} \sin \frac{\theta}{2} \tag{2.25}$$

where λ is the neutron wavelength and θ is the scattering angle. To simplify the scattering expression, it is useful to divide the sample into N_p cells, each of which contains one particle along with structureless solvent of mean scattering density ρ_s. The particle itself may have internal structure, so the scattering length density inside the particle may vary with position. If b_{lN} is the averaged bound scattering length of atoms l in cell N and R$_{lN}$ is the location of atom l relative to the center of mass of the particle N, the scattering length density of the particle is

$$\rho_N(R) = \sum_l^{n(N)} b_{lN} \delta(R - R_{lN}) \tag{2.26}$$

The sum is over all atoms n in cell N, $\rho_N(R)$ has units of cm^{-2}. With this result, the scattering amplitude of the particle is defined as

$$F_N(Q) = \int_{particle N} dR[\rho_N(R) - \rho_S] \exp(iQ \cdot R) \tag{2.27}$$

and

$$F_N(Q) = \sum_n f_n(Q) \tag{2.28}$$

here the scattering amplitude is written as a function of the momentum transfer Q not scattering angle θ. This is more general and more convenient in small angle scattering applications. The correlation between θ and Q is shown in Eq. (2.25).

If the system under investigation consist of N identical atoms (or more generally molecules, cells or particles) with scattering length amplitude $f(Q)$.

Thus, from Eq. (2.20), the intensity of scattering by the whole ensemble is given by:

$$I(Q) = \sum_{i=1}^{N} \sum_{j=1}^{N} f_i(Q) f_j(Q) \exp(iQ(R_i - R_j)) \qquad (2.29)$$

where R_i and R_j are the coordinates of atoms or vectors describing the positions of the sets. Separating the terms with $i = j$ and averaging over the ensemble, the following equation is obtained:

$$
\begin{aligned}
\langle I(Q) \rangle &= \left\langle \sum_{i=1}^{N} f_i^2(Q) \right\rangle + \left\langle \sum_{i=1}^{N} \sum_{j=1,j \neq i}^{N} f_i(Q) f_j(Q) \exp(iQR_{ij}) \right\rangle (2.30) \\
&= \langle N \rangle \left\langle f^2(Q) \right\rangle + \langle f(Q) \rangle^2 \left\langle \sum_{i=1}^{N} \sum_{j=1,j \neq i}^{N} \exp(iQR_{ij}) \right\rangle \qquad (2.31)
\end{aligned}
$$

where $R_{ij} = R_i - R_j$. The value $\langle N \rangle$ is written here instead of N, because the number of particles can also fluctuate in the general case. Thus, the scattering from a collection of particles is made up of the sum of two terms, the first of which depends on intra-particle scattering and the second on inter-particle scattering. Intra-particle scattering is simply the average of the square of the particle amplitude factor and can be calculated for particles of any geometry. This term depends on both the shape of the particle and the distribution of atomic species within it. The inter-particle term, however, can be evaluated in a closed form only if major assumptions about the correlations between the spacing of the particles and their sizes and orientations are made. The simplest assumption is that the sample contains a monodisperse population of spherical scatterers where $f_i(Q) = f_j(Q) = f(Q)$, for which Eq. 2.31 may be simplified to the form

$$
\begin{aligned}
I(Q) &= \langle N \rangle F^2(Q) \left(1 + \frac{1}{\langle N \rangle} \left\langle \sum_{i=1}^{N} \sum_{j=1,j \neq i}^{N} \exp(iQR_{ij}) \right\rangle \right) \\
&= \langle N \rangle P(Q) S(Q). \qquad (2.32)
\end{aligned}
$$

The parameter $P(Q)$ is the particle form factor, and $S(Q)$ particle structure factor. Details about $P(Q)$ and $S(Q)$ properties can be found in e.g. [34, 35, 39]. Here only few properties will be discussed.

The form factor depends on the size and shape of the particle, while the structure factor, which is essentially the Fourier transform of the radial distribution function, depends on the relative locations of the individual droplets ($S(Q) = 1$ at infinite dilution). The limiting forms of $P(Q)$ and $S(Q)$ are especially interesting. When Q goes to zero, $P(Q)$ approaches 1 and the

scattering depends only on $S(Q)$, while at large Q, the dependence is only on $P(Q)$ because $S(Q)$ reaches 1.

There is fundamental structural information obtainable from the scattering curve when the Q is large. This behaviour is independent of any models and the only assumption which has to be made is that the boundary between objects and solvent is sharp. This is called Porod limit [40], and for a three dimensional object with sharp boundary the form factor is proportional to Q^{-4}.

2.3.2 Porod law

It is possible to write an explicit equation for the averaged scattering intensity, the coordinates of atoms within a system being given. If there are N atoms with scattering lengths $f_i(\mathbf{Q})$ (which may be regarded as constant in the small angle region: $f_i(\mathbf{Q}) = f_i(0) = f_i$) and coordinates $\mathbf{r_i}$ within a particle, then, average intensity can be written:

$$I(Q) = \sum_{i=1}^{N} \sum_{j=1}^{N} f_i f_j \frac{\sin(Q r_{ij})}{Q r_{ij}} \tag{2.33}$$

where $r_{ij} = |\mathbf{r_i} - \mathbf{r_j}|$ while the sum is taken over all the atoms in a system. This equation was derived by Debye [41] and provides an exact expression for the small angle scattering intensity by a particle. If a density distribution function $\rho(\mathbf{r})$ is taken instead of particle the Eq. (2.33) takes the form:

$$I(Q) = \int_V \int_V \rho(\mathbf{r_1}) \rho(\mathbf{r_2}) \frac{\sin(Q r_{12})}{Q r_{12}} d\mathbf{r_1} d\mathbf{r_2} \tag{2.34}$$

In the continuous distribution of function $\rho(\mathbf{r})$ the variable $\mathbf{r_2}$ can be replaced by $\mathbf{r} = \mathbf{r_2} - \mathbf{r_1}$. Then when the order of integration is changed and a spherical polar coordinate system is used for the integration over $\mathbf{r}$, the Debye scattering can be transformed:

$$I(Q) = 4\pi \left\langle \rho(\mathbf{r})^2 \right\rangle V \int_0^l r^2 g(r) \frac{\sin(Qr)}{Qr} dr \tag{2.35}$$

with

$$g(r) = \frac{1}{4\pi \left\langle \rho(\mathbf{r})^2 \right\rangle V} \int_0^{2\pi} d\beta \int_0^{\pi} \sin\alpha \, d\alpha \int_V \rho(\mathbf{r_1}) \rho(\mathbf{r_1} + \mathbf{r}) dV_1 \tag{2.36}$$

and

$$\left\langle \rho(r)^2 \right\rangle = \frac{1}{V} \int_V \rho(\mathbf{r_1})^2 dV_1. \tag{2.37}$$

18

The integration in Eq. (2.35) is done from 0 to l, where l is the diameter of the scatterer - the length of the longest straight-line segment for which both ends can be contained within the scatterer. The angles α, β are coordinates that specify the orientation of the vector $\mathbf{r}$ in the spherical polar coordinate system.

The function $g(r)$ is called correlation function. In the volume integral in Eq. (2.35), $\mathbf{r_1}$ represents a point in the scatterer, and $\mathbf{r_1} + \mathbf{r}$ is a second point in the scatterer that is displaced by the vector $\mathbf{r}$ from the first point. Since the diameter l is the largest distance, $g(r) = 0$ when $r > l$. The function $g(r)$ has many other properties. From Eq. (2.35) states that $QI(Q)$ is proportional to the Fourier sine transform of $rg(r)$. Thus in principle $g(r)$ can be evaluated by a numerical Fourier transform of measured data.

Although this result may at first seem very useful, there are some factors that limit its application. Evaluation of $g(r)$ requires intensity data for all Q, and effect of termination of the numerical integration can be difficult to estimate.

Other properties of the function $g(r)$ stays that

$$g(r) \approx 1 - \frac{S}{4V}r \qquad (2.38)$$

where S is specific surface of the particle (detailed analysis of $g(r)$ can be found in e.g. [34, 35, 39]).

The function $QI(Q)$ is proportional to a Fourier sine transform of $rg(r)$. Thus for large Q an approximation of the Fourier transform $F(x)$ for large x [42] can be used to evaluate $I(Q)$. One of the properties of a Fourier transform $F(x)$ of a function $f(x)$ is that the behavior of the transform at large x is determined by the values of $f(x)$ and its derivatives near the end points of the integral and in the neighborhood of any points in the interior of the interval of integration at which $f(x)$ or one of the derivatives is discontinuous. When Eq. (2.35) is twice partial integrated, the following equation is obtained:

$$I(Q) = -\frac{4\pi \left\langle \rho(r)^2 \right\rangle V}{Q^3} \int_0^l [rg(r)]^{(2)} \sin Qr dr. \qquad (2.39)$$

The superscript (i) denotes derivatives of order i. The result makes use of the fact that under quite general conditions, $g(l)^{(1)} = g(l) = 0$. Although further integration by parts cannot be performed an arbitrary number of times, the

integral often can be integrated once more by parts. The results is

$$
\begin{aligned}
I(Q) &= \frac{4\pi \left\langle \rho(r)^2 \right\rangle V \left(-2g^{(1)}(0) + l g^{(2)}(l) \cos Ql \right)}{Q^4} \\
&\quad - \frac{4\pi \left\langle \rho(r)^2 \right\rangle V}{Q^4} \int_0^l [rg(r)]^{(3)} \cos Qr \, dr
\end{aligned}
\tag{2.40}
$$

The last was obtained with the assumption that $g^{(1)}(r)$ and $g^{(2)}(r)$ are continuous for $0 \leq r \leq l$, and that $g^{(3)}(r)$ is integrable over this interval. When these conditions are fulfilled Eq. (2.40) is exact.

According to general property of Fourier integrals, the integral on the right side of Eq. (2.40) approaches zero when Q approaches infinity. Therefore there is the limit for large Q and Eq. (2.40) takes the form:

$$
I(Q) = \frac{4\pi \left\langle \rho(r)^2 \right\rangle V \left(-2g^{(1)}(0) + l g^{(2)}(l) \cos Ql \right)}{Q^4}.
\tag{2.41}
$$

Using [35]

$$
g^{(1)}(0) = -\frac{S}{4V}
\tag{2.42}
$$

and $g^2(l) = 0$ which is valid for most solids bounded by a smooth surface (a sphere is one of the few exceptions), the limit of $I(Q)$ for large Q has the form:

$$
I(Q) = \frac{2\pi (\rho_0)^2 S}{Q^4}
\tag{2.43}
$$

Chapter 3

Setup of the experiment

3.1   Introduction

The properties of solid Deuterium as a moderator and UCN converter with cold, very cold and ultracold neutrons have been measured. To cover this wide range of neutron wavelengths we used energy-dependent transmission and scattering at the small angle scattering instrument at SINQ using cold neutrons (CN) with a wavelength in the range of 5 to 36 Å. The experiments with the very cold (VCN) and ultracold neutron (UCN) beams were done at PF2 at ILL with wavelength 20-200 Å and 140-600 Å, respectively. The setup of these experiments was similar; it was possible to use the same cryostat with the same target cell, the preparation of the samples was done in a similar way. The detectors, the wavelength selection and the scattering angle determination were different for the different measurements.

In this chapter, details and the properties of the experimental setup, the method of sample preparation, the Deuterium gas system, optical investigation, Raman spectroscopy, detectors, data acquisition systems and slow control are described (see also [43]).

3.2   The cryogenic sD_2 target cell

The main and the most important part is the cell for solid Deuterium, (see Fig. 3.1 and 3.2). It has an inner volume of $40\,cm^3$ and is made of AlMg3 alloy. In the neutron beam axis the cell has an entrance and an exit window, $10\,mm$ apart, each with a thickness of $0.15\,mm$ and a diameter of $25\,mm$. These thin windows (together with the flanges) have been machined out of the solid so that they form single pieces. The sealing to the cell body is realized by squeezing $1\,mm$ diameter indium wire into a rectangular $1.1 \times 0.5\,mm^2$

Figure 3.1: The major mechanical pieces of the cryogenic target cell are displayed: The cell body, the reentrant neutron beam windows, the optical sapphire windows with Al press rings. The vertical axis of the cell is for cooling (from below) and gas connections (from above) as well as thermometry and heating. All flange connections are sealed with indium.

groove. The horizontal axis perpendicular to the neutron beam axis is the optical axis. Two parallel sapphire windows, 72 mm apart, allow Raman spectroscopy and simultaneous optical inspection and image collection. The sapphire windows, 3 mm thick and 29.95 mm in diameter, are sealed to the body of the cell using an Aluminium press ring. A 0.1 mm thick teflon foil is used to uniformly distribute the force on the sapphire, the sealing of the sapphire windows to the cell being realized by indium seals. The cell has a top part with an Aluminium-stainless steel friction weld. A stainless steel service port, flanged to this transition piece, carries the dual inlet capillaries into the cell via a low thermal conductivity path. The temperature of the inlets can be kept above the freezing point of Deuterium with a minimal heat input to the cell, controlled by a heater and thermometer inside the cell on the very ends of the capillaries.

The cell is mechanically connected to the Copper bottom part of a vertical ^{4}He flow cryostat and cooled via two OFHC Copper rods of 12 mm diameter each. The flow cryostat can be cooled down from room temperature to 20 K in 3 hours using 14 liter of liquid Helium. It has a single thermal shield at 80 K with two permanent openings of 10×24 mm^2 for optical access. The Helium consumption is 0.6 l/h at 20 K, 1.5 l/h at 5 K, with an average of less

thermal shield connection

inlet capillaries

bottom part of He flow cryostat

friction weld

thermal yoke

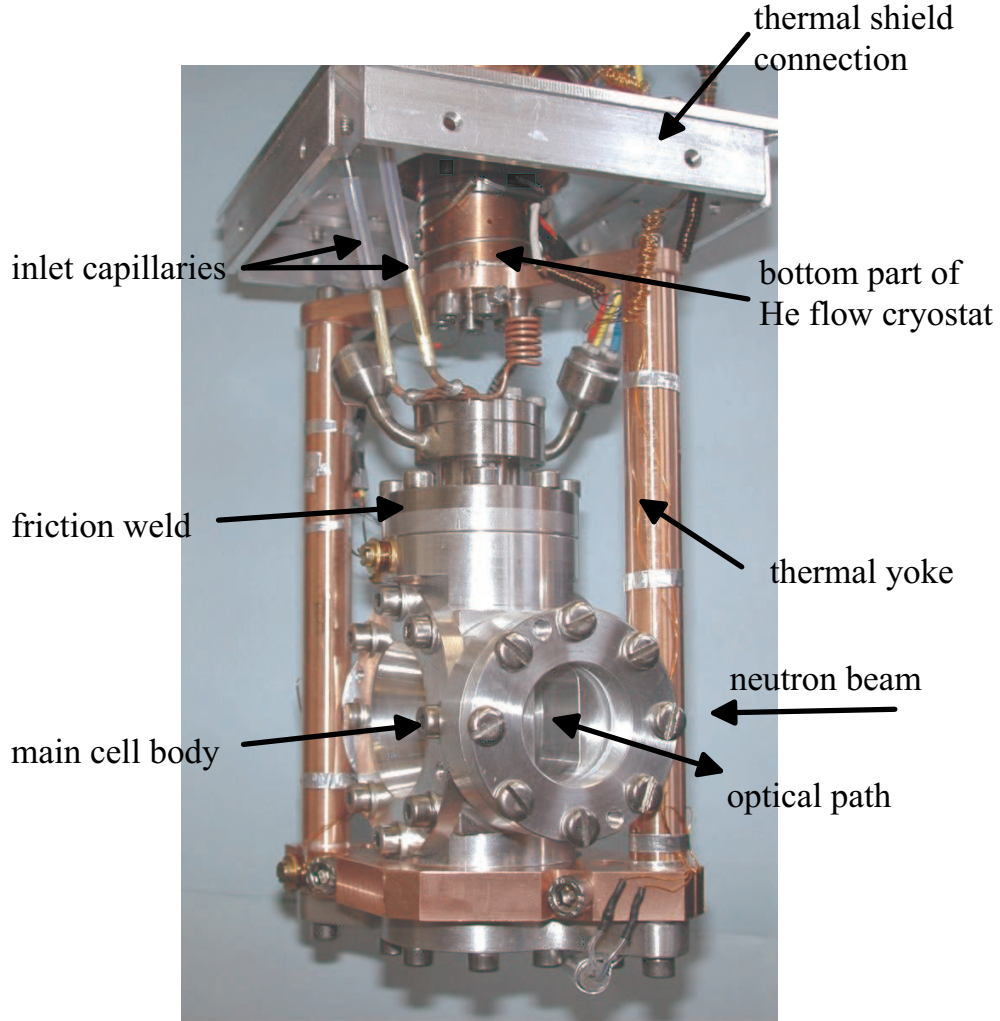neutron beam

main cell body

optical path

Figure 3.2: The target cell mounted on the cryostat. The thin Al thermal shielding is dismounted. Details are given in the text.

than 250 l in 7 days.

Four Si-diode thermometers and two heaters are installed on the cryogenic system. The temperature read-out and heaters are remote-controlled and relevant data are continuously logged.

3.3 The Deuterium gas system

Figure 3.3 shows a schematic lay-out of the D_2 gas system. Deuterium is available in pressurized gas cylinders in different qualities, 99.8% and 99.95%
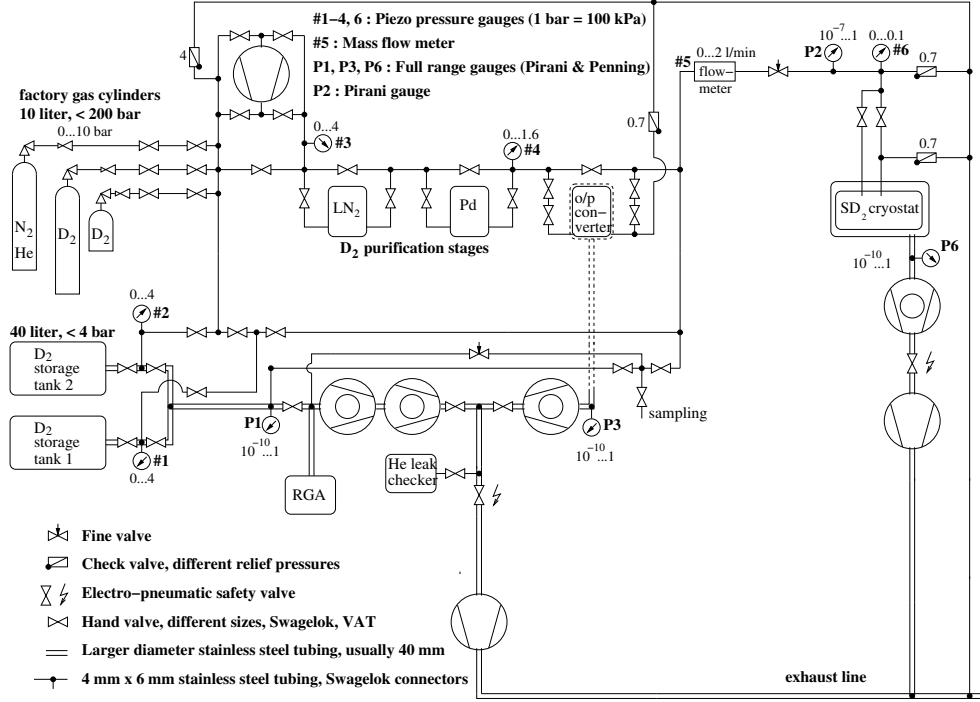
Figure 3.3: A schematic layout of the D_2 gas handling system.

purity, respectively. During regular experimental procedures, D_2 is filled into one of the two available storage tanks. The size of the storage container 40 liter was chosen such that the volume of D_2 slightly above atmospheric pressure is sufficient to fill the cryogenic target cell with liquid or solid D_2. The storage containers are made from aluminum in order to avoid ortho-D_2 relaxation in collisions with magnetic surfaces. The tubing of the gas system in most parts is made from stainless steel (4 mm ID) and uses standard stainless steel connectors and bellow valves. The tubing has been cleaned in an ultra-sonic bath and was baked before assembly. Suitable overpressure protection of the warm parts of the system is done by check valves which open at 4 bar overpressure on the "high pressure" input side of the system and at 0.7 bar overpressure at all other locations. A fine adjustment valve is used to regulate the in-flow into the cryogenic target cell. The operation of the gas system is monitored using piezo-electric pressure gauges for pressures between 0 and 4 bar absolute pressure and combined pirani and penning vacuum gauges below 1 mbar. The in-flow into the cryogenic target cell is monitored via pressure drop in the storage container and with the help of a mass-flowmeter. All gauges are continuously read out from a slow control PC. The gas system can be evacuated using a dry pumping system with a

24

turbo pump backed by a turbo drag pump for increased performance when pumping Hydrogen/Deuterium and a piston roughing pump. The rest gas of the system can be analyzed using a quadrupole mass spectrometer, which is also used for leak checking the system with argon and to monitor the leak tightness during operation.

A Palladium membrane is used for Deuterium purification. It can be heated and is typically operated at 100-150°C in this experiment. Care has to be taken because the ortho-concentration of the D_2 gas after passing through the membrane corresponds to the high temperature limit of $2/3$. Thus the Pd membrane can only be used for normal D_2 or at the input of the device to prepare higher ortho-concentrations ("ortho-para converter", see below).

An encapsulated metal-membrane compressor is used to push D_2 from one part of the gas system to another, for example increase the Pd membrane input pressure, or to add more D_2 into the cryostat, or to transfer D_2 from one storage container to the other one. The compression ratio depends on pressure, but usually is around 2.5.

A special ortho-para (o/p) converter allows preparation of higher ortho-D_2 concentrations, up to $c_o = 98.5\%$, working with liquid D_2 close to the triple point (18.7 K). The thermal equilibrium c_o-values are 66.7%, 95% and 98.5% for 300 K, 25 K and 18.7 K, respectively. Because the natural conversion of para- to ortho-D_2 into thermal equilibrium takes of the order of months, the process needs to be accelerated with a suitable catalyst. We used OXISORB® [44, 45] in order to catalyze the conversion. OXISORB® consists of silica gel impregnated with chromic oxide (CrO_3), the oxide being bonded to the silica structure via hydroxyl groups. The chromic oxide provides paramagnetic centers with strongly inhomogeneous magnetic fields allowing a dephasing of the nuclear spins within the D_2 molecule coming close to this site. The conversion rate can thus be highly accelerated, also taking advantage of the large surface of the silica gel. The converter consists of a $150 \, cm^3$ volume OFHC copper cylinder which can be connected on one side to a cryo cooler, (see Fig. 3.4). The second side allows access for filling the catalyst and can be connected to a stainless steel part which holds a $150 \, \mu m$ thick, 70 mm diameter Al (Alcoa) window as a bursting disk. The copper - stainless steel flanges have trapezoidal ridges in order to squeeze a $100 \, \mu m$ thick Kapton ring for cryogenic sealing. Cup springs guarantee the proper pressure on the sealing even for large temperature changes. The exit gas line is located at the upper end of the Cu cylinder wall, the input gas line on the stainless steel part. The catalyst is located between the gas input and outlet inside the Cu cylinder and held in place by two stainless steel sinter-disks ($10 \, \mu m$ mesh). The volume outside the sinter-disks, which is accessible for liquid D_2, has been minimized in order to guarantee good contact with the
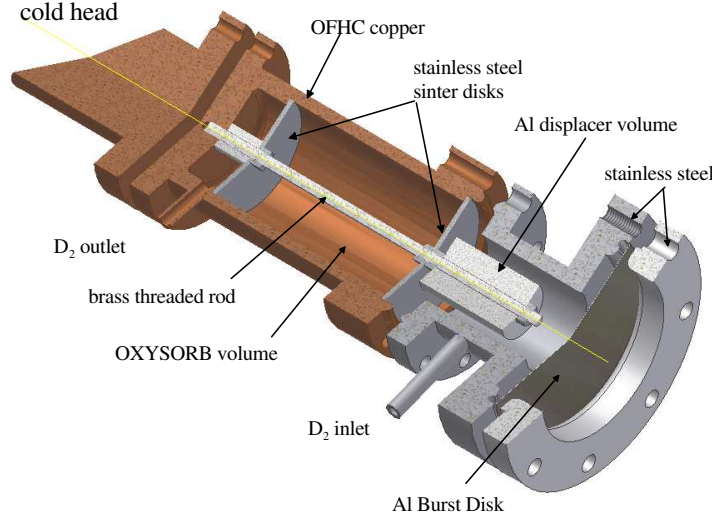
cold head

OFHC copper

stainless steel
sinter disks

Al displacer volume

stainless steel

D_2 outlet

brass threaded rod

OXYSORB volume

D_2 inlet

Al Burst Disk

Figure 3.4: Cut through the o/p converter cell.

catalyst. The content of one mini-cartridge OXISORB® (about $40\,cm^3$) was used for a fill of the copper cell. The converter was filled and assembled in an argon glove box in order to avoid the exposure of the catalyst to air. The two gas lines were closed by two welded stainless steel bellow valves with removable valve handles. The converter cell was then mounted hanging on the cold head of a closed cycle refrigerator. The gas lines were connected to the gas system and evacuated before the two valves were opened. The valve handles were removed and the valves were mounted together with the converter in an insulating vacuum vessel. The valves tolerate cryogenic temperatures in their open position and can again be regularly used after warming. The cold head has a cooling power of up to $10\,W$ at 10-12 K. The temperature is measured by means of a hydrogen thermometer and can be manually varied between 14 and $26\,K$ using a heater on the output gas connection. Cooling down the empty o/p converter from room temperature to below $14\,K$ takes less than $4\,h$. Filling the o/p cell with liquid D_2 can be rather fast if the flow rate is not limited by the Pd membrane. Using the Pd membrane it takes typically 2-3 h to fill the o/p cell with 40-60 cm^3 liquid D_2.

The converter can in principle work in flow-through mode and in residence mode. It is, however, usually used in residence mode. A certain amount of D_2 (typically $60\,dm^3$ at the atmospheric pressure, correspond to about $60\,cm^3$ liquid) is liquefied into the converter cell and kept at the triple point (18.7 K). We have observed $c_o = 85\%$ after conversion times of about $3\,h$,

suggesting a conversion time constant of about $\tau_{o/p} \approx 3 - 3\frac{1}{2}$ hours, $c_o(t) = c_o^{18.7K} - (c_o^{18.7K} - c_o^{300K}) e^{-t/\tau}$. After more than 12 h, gaseous ortho-D_2 with c_o up to 98.5% can be extracted through the outlet of the converter, e.g. by freezing from the vapour into the colder target cryostat, compare Fig. 3.3. Because the catalyst soaks up some gas and some fraction of the D_2 can only be recovered at higher temperature (and correspondingly lower c_o), it turned out to be important to fill more D_2 into the converter than we actually would use in the target cell (roughly $40 \, cm^3$).

No deterioration in the performance of our catalyst material was observed during the more than few years inside the experimental apparatus and conversion of several liters of liquid D_2.
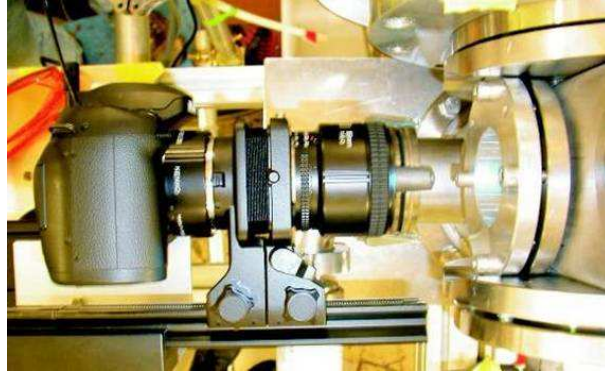
3.4   The optical photography system

Figure 3.5: Setup of the camera system. One can see the mirror reflex camera in the front. The camera is mounted on an Aluminum plate and screwed to the cryostat plate using Aluminum profiles. A tripod-head and a strong Aluminum angle hold the camera in position.

For optical imaging a digital SLR camera with a 23.7 x 15.6 mm^2, 6MPixel CCD-Chip, which is well matched to the visible area of the optical target window, is used. The 85 mm lens, together with extension bellows and tubes allows the reproduction scale to be extended to a maximum of 6.2:1. With the given pixel size of 7.8 μm, structures of a few μm can be resolved. Usually, however, the entire crystal is monitored at a reproduction scale of about 1:1. The shutter of the camera is remotly controlled from the slow control PC, while the focus is set manually. Images are stored on the RAID system of the slow control. The system is mounted on a modified tripod-head, allowing movements in both horizontal directions. A stable Aluminum frame supports

the tripod and can be moved in the vertical direction with threaded bolts. The frame itself is fixed to the cryostat-support. During operation the camera is shielded from stray light. The illumination of the crystal is usually done by the Raman laser (see below) which is simultaneously operated. Although not perfectly homogeneous, this light source is stable at the 1%-level and suitable for our application.

As an example for the monitoring of the freezing process, a series of pictures are given in Fig. 3.6 showing the growth of a clear crystal from the liquid. Clear, fully transparent crystals can be grown over a time period
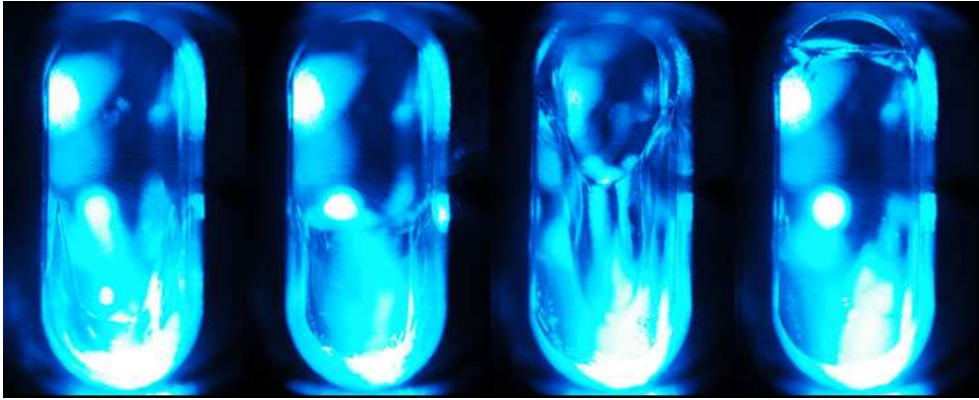

Figure 3.6: The sequence of photographs, working from left to right, shows how an optically transparent crystal grows from the liquid held close to the triple point. The first image shows the cell full of liquid Deuterium but with the U-shaped solid-liquid phase boundary visible in the lower half. The rest of the pictures show the phase boundary rising towards the top of the cell. It is interesting to note that the refractive index of the liquid and solid Deuterium are almost equal as may be seen from the unchanged position of the laser reflection spots on the first and last images.

of about 12 h at temperatures close to the triple point. The quality of the resulting crystals strongly depends on the speed of crystal growing. It will be very important for the later neutron transmission studies to quantify the amount of D_2 within the beam region. The amount is known best when the whole region is homogeneously filled, which is confirmed by the corresponding photographs.

The brightness of the optical images is a direct measure of the crystal light transmission, when camera parameters like aperture or shutter speed are not varied and the illumination of the crystal is stable.

3.5 The Raman spectroscopy system

The Raman system consists of three main parts: the laser light source, the Raman head, and the Raman spectrometer. These components can be spatially separated using optical fibers, in our case up to 15 m long.

3.5.1 Laser source

A transportable 60 mW (cw) argon-ion-laser (Uniphase) is used. It operates at 487.98 nm optical wavelength in the blue-green visible part of the spectrum; only about 1% of the laser power is emitted in different additional lines, some of which are useful for spectrometer calibration. The stability of the main line does not limit the resolution of the Raman measurements.

Directly on the laser, the light is coupled into a 1 mm multimode fiber using a commercial integrated lens device. Different fiber lengths for different setups are used. The measured intensity losses are about 10% due to the coupling and slightly less than 10% per meter fiber length.

3.5.2 Raman head

The Raman head consists of two optical sections on a common, adjustable support, the laser head for the light input and the Raman collector for the scattered light, see Fig. 3.7 and 3.8. It is mounted close to the target cell but outside the warm vacuum window. Although mounting inside the vacuum or even on the cold parts would allow increased solid angle for light collection, it would be considerably more complicated and less versatile. The whole philosophy of the setup was to allow simple and fast adjustment, including exchange of lenses and relative positions. The selection of a Raman backscattering geometry is a compromise; it clearly leads to an increased background from fluorescence and Rayleigh-scattered laser light from the optical windows in the light path but it needs only one of the optical access ports of the target cell.

The laser head focusses the laser light coming from the fiber through the outer vacuum window (5 mm thick, boron-silicate) and the target cell window (3 mm sapphire) into the sample. Different areas of the target volume can be reached by varying the position of the laser head and the focal length. The size of the focus can be adjusted down to a diameter with a 1 mm for 60 mm focal length.

The Raman collector is mounted on the same support as the laser head. It is placed closer to the warm window than the laser head in order to increase the solid angle for light collection. The Raman collector can be moved

29

Figure 3.7: The Ar laser light is coupled to the laser head via optical fiber. The simple but stable and easily adjusted setup of the laser head (upper) and Raman collector (lower) is displayed.

vertically and horizontally by manual screws. Positions are reproducible with accuracies better than 1 mm (i.e. within the focus) over a scan distance of 50 mm.

The position of the Raman collector has to be optimized in order to achieve both high signal intensity and reasonable signal-to-background ratio. In addition the laser head and the collector can be separately rotated in order to change their relative angle.

3.5.3 Raman spectrometer

A SPEX14018 (3/4)-m double-grating monochromator with 2-dimensional liquid nitrogen cooled CCD-camera and motor driven mirrors is used.

The Raman light from the signal-transfer fiber is focussed onto the spectrometer entrance slit. The slit width can be varied manually with a reproduceable precision of $2.5\,\mu$m. For normal measurements with high spectral
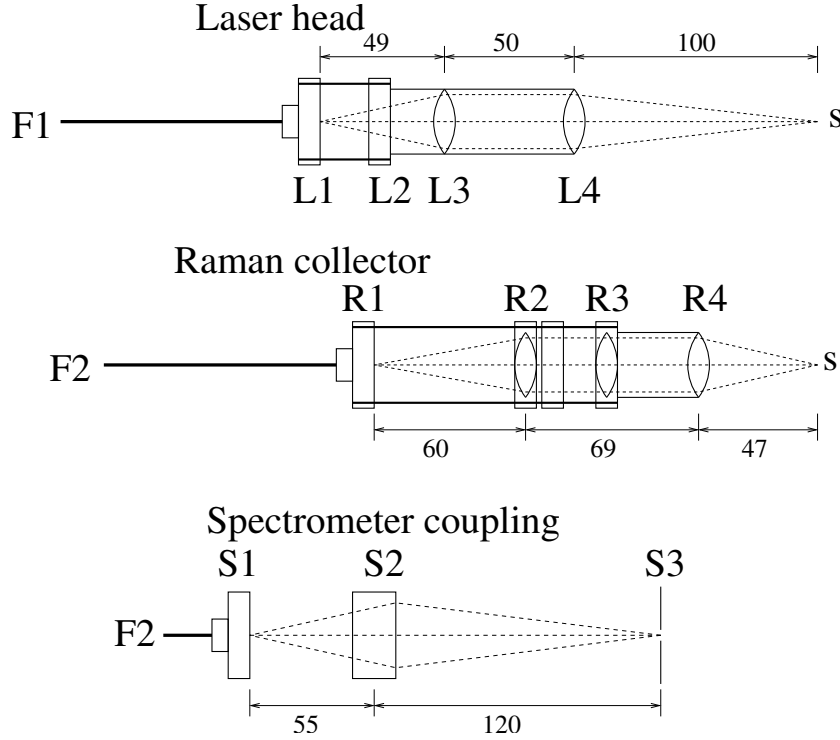
Figure 3.8: Scheme of the optical setup: Fiber F1 (about 2 m length, 1 mm core diameter) connects the laser to the laser head. F1 is mounted in the fiber fixation L1. A frame L2 mechanically stabilizes the laser head; L3 (biconvex lens (BL), f=38 mm) and L4 (BL, f=100 mm) focus the laser onto the sample S. The Raman light is collected from S via R4 (BL, f=50 mm) and R3 (BL, f=60 mm); R2 (BL, f=38 mm) focusses the light into fiber F2, sitting in fiber fixation R1; F2 (about 15 m long, 1 mm core) brings the light to the spectrometer fiber fixation S1. The aspheric biconvex lens S2 (f=60 mm) focusses the light onto the entrance slit S3 of the monochromator.

resolution, slit widths of 50-100 μm were used, in some cases a slit width of 500 μm was chosen in order to increase intensity. Depending on the slit width, 10% to 27% of the signal light passes through the first monochromator. The spectral resolution of the spectrometer is limited by the CCD pixel size, which corresponds to 0.47 wavenumbers in the region of interest. The entrance slit has an additional effect on resolution, however, no variation below 100 μm slit width is observed. The overall energy resolution is better than 1 cm^{-1} for the 100 μm slit. The spectral intensity increases by a factor of 8 when opening the slit from 100 to 500 μm.

The light is reflected between two gratings and different mirrors, each monochromator stage has one grating and corresponding shielding box for suppression of scattered light. The gratings have effective areas of roughly 100 × 100 mm^2 and 1200 rulings per mm. The transfer window width between
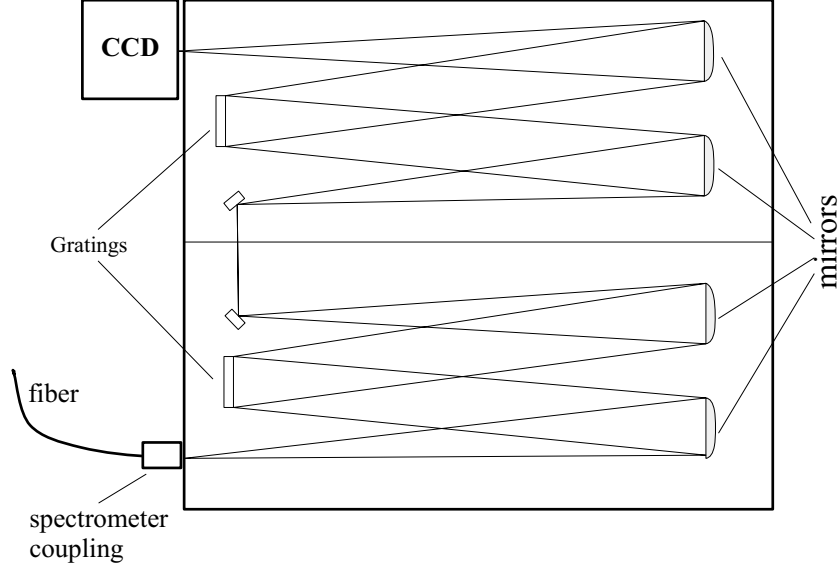
Figure 3.9: Top view of the Raman spectrometer setup.

the two stages can be controlled by an internal slit, but is used fully open in our case. At the exit of the spectrometer the light is detected by a CCD-detector (512×512 pixels, $20 \times 20 \, \mu\text{m}^2$ each). The CCD is cooled by liquid N_2; its integrated dewar has to be refilled every 7 hours for continuous operation. The working temperature is 154 K stabilized by electrical heating to better than 1 K. The (electronic) background of the CCD chip is not very sensitive to temperature below 175 K.

The CCD is connected via an external electronic unit to a dedicated Raman PC; the electronic unit supplies the operating power and manages the readout and data transfer. The PC card allows remote control of the Raman data acquisition. A regular mode of operation is to read out the CCD every 30-200 s and continuously take data in between. All CCD raw data files, together with all other data (temperatures, pressures, optical images) are stored with proper time synchronization on the RAID disk system of the slow control PC.

In the configuration of the spectrometer as described one can cover a spectral area of 231 wavenumbers between $78 \, \text{cm}^{-1}$ and $319 \, \text{cm}^{-1}$ relative to the laser line, without changing the position of the spectrograph. This position is optimized for the simultaneous investigation of the lowest two rotational lines of D_2. Other regions of the spectrum can be measured after changing the position of the spectrometer mirrors which is done by two stepper motors; their pulsed low voltage power supply is controlled from the PC via an external programmable card. Different positions are reproduced to better

than $1\,\mathrm{cm}^{-1}$.

3.5.4 Data treatment

The raw data files taken by the CCD detector provide count rate information in form of two-dimensional (512×512) arrays. With a good mechanical alignment of the CCD-chip on the spectrometer, each CCD column corresponds to a certain wavenumber, rows do not provide any physical information. Thus one needs the total count rates for every column in order to achieve a regular Raman spectrum. However, some data treatment is needed before useful spectra can be extracted.

Usually, raw data files are contaminated by spectral artifacts, caused e.g. by cosmic radiation, and it is necessary to detect and remove all of them. For this purpose, a 2-dimensional modification of the Upper-Bound Spectrum algorithm (UBS) was used (see [46] for details) as a first step. The main principle of the algorithm is to compare two different data files measured one after the other and search for pixels with a count rate difference greater than a reasonable threshold. In this way cosmic spikes are detected. Afterwards the contaminated pixels from one of the files are replaced by the corresponding pixels from the other one, multiplied by a suitable normalization coefficient to account for intensity variations of the Raman spectrum between the measurements. Another algorithm analyzes the mean and RMS values and controls whether spikes in the two compared data sets accidentally overlap, which occurs in a few percent of all cases. This is then flagged and can be corrected by comparison with another reference file. In the next step the constant electronic offset, which is always present in the CCD data, is subtracted. Assuming a purely statistical readout noise, the real mean count rate in the spectrum must be close to the RMS value squared. We thus select a relatively flat subrange of the spectra and determine the offset by requiring a regular counting statistics for the resulting spectrum after subtracting the offset.

Finally, the two-dimensional pixel arrays are projected into one row and become Raman spectra free of spikes and bias, but not yet calibrated.

3.5.5 Raman spectra

In order to demonstrate the quality of the Raman data and to show what kind of information can be obtained we display some example spectra, (see Figs. 3.10 and 3.11).

The first one is for normal D_2 ($c_o = 2/3$) in the liquid phase. The $S_0(0)$ and the $S_0(1)$ lines for D_2 are seen, corresponding to the transitions between
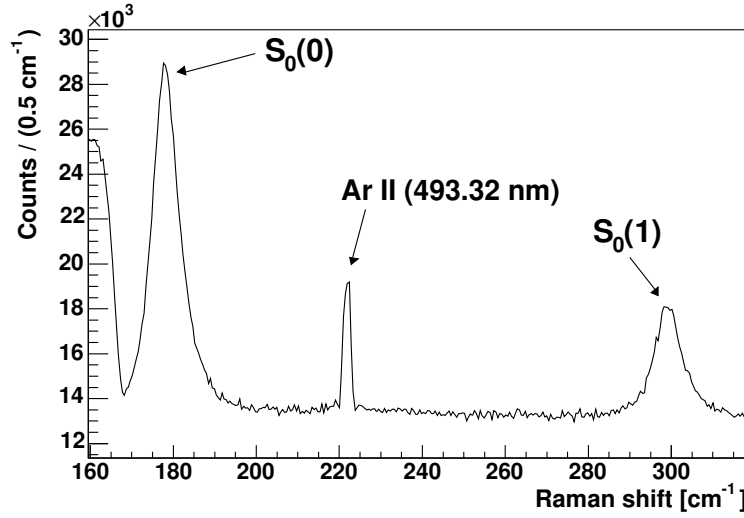
Figure 3.10: Rotational Raman spectrum of liquid normal D_2 (66.7% ortho-D_2). The spectrum contains data from 79 single files with 60 s exposure time each. The $S_0(0)$ and the $S_0(1)$ lines for D_2 correspond to the transitions between purely rotational states $J = 0 \rightarrow 2$ and $J = 1 \rightarrow 3$, respectively. The Ar calibration line gives the resolution of the spectrometer, thus the width of the D_2 peaks is easily identified as a feature.

purely rotational states $J = 0 \rightarrow 2$ and $J = 1 \rightarrow 3$, respectively. The Ar calibration line gives the resolution of the spectrometer, thus the width of the D_2 peaks is easily identified as a feature. In the left part of the spectra, the background from the Rayleigh scattered light is visible. The spectrometer is set such that the background is cut by the internal slit slightly outside the region of interest.

Fig. 3.11 shows a similar spectrum, but for solid ortho-D_2 with $c_o = 98.6(4)\%$. As compared to normal D_2, ortho-D_2 shows Raman lines which are considerably more narrow. Due to the interaction of the ortho molecules with neighbouring (para-)molecules, the different possible nearest neighbour configurations lead to different shifts of the energy levels and to line broadening. The resolution is sufficient to see the splitting of the $S_0(0)$ line in the ortho solid (see [47]). The hcp symmetry of D_2 crystals makes the $J = 2$ level form three energy bands belonging to $m = \pm 1\,(\alpha)$, $m = \pm 2\,(\beta)$, and $m = 0\,(\gamma)$, respectively. The line intensity ratios within the multiplet contain information about the relative orientation of the crystal (or crystallites) with respect to the direction of the Raman collector [47, 43].
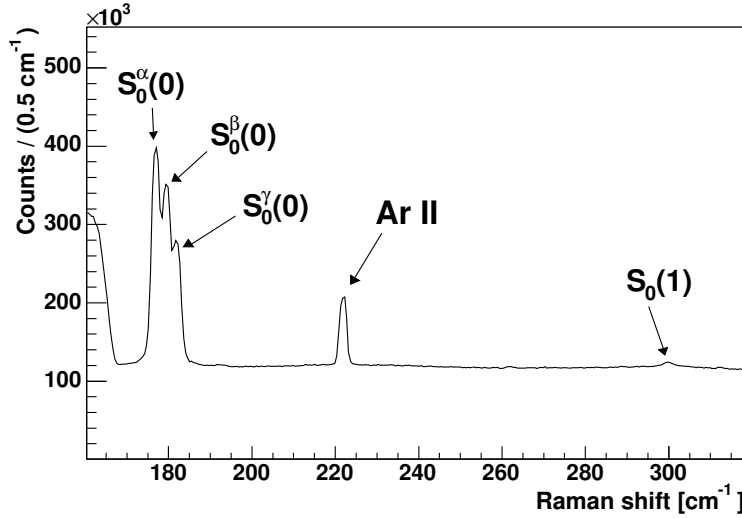
Figure 3.11: Same as Fig. 3.10 but for solid o-D_2 (98.6%). The multiplet structure of the $S_0(0)$ line is due to the splitting of the $J = 2$ band in the hcp crystal. The spectrum contains data from 356 single files with 200 s exposure time each.

3.5.6 Ortho-D_2 concentration

From the intensity ratio of the $S_0(0)$ and the $S_0(1)$ lines the ortho-D_2 concentration can be calculated taking into account the proper transition matrix elements and the efficiency of the spectrometer. As a cross-check, the intensity ratio of the two lines is compared in a measurement of the known value $c_o = 2/3$ for normal D_2. The most dangerous source of systematic uncertainties, which significantly limits the accuracy of our measurement, is the background contribution from fluorescence of the optical windows; this is difficult to avoid in backscattering geometry. For high ortho concentrations the intensity of the $S_0(1)$ line is small and it is easily affected by background. In order to solve this problem, the exact shape of the background has been determined with special long duration measurements with the empty cell. It was confirmed that the background shape does not depend on the position of the laser focus point within the cell. The Raman spectrometer was used before for the investigation of D_2 gas samples. The corresponding results concern the ortho-D_2 equilibrium in a liquid D_2 moderator under irradiation and have been published in [48]. Generally this method was similar to the one described in [49], however, given high enough resolution we were able to analyze the ro-vibrational Raman Q-branch rather than pure rotations. For the in-situ spectroscopy of liquid and solid D_2 inside the cryogenic target cell, we returned to spectroscopy of pure rotational lines as was shown above in
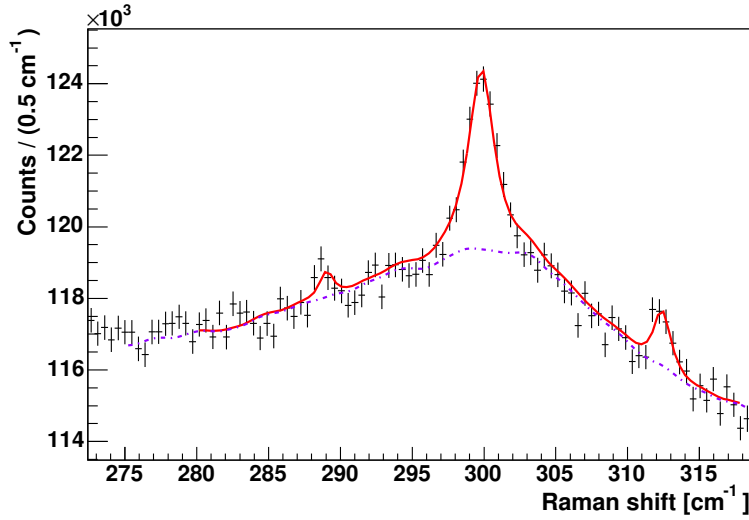
Figure 3.12: Background subtraction for the $S_0(1)$ D_2 line for the same data as in Fig. 3.11

.

the example spectra. The reason is that, due to the Boltzmann distribution of the state population within the even and odd J bands, at low temperatures only $J = 0$ and $J = 1$ states are populated. The two remaining Q-branch lines ($\nu = 0 \to 1, J = 0 \to 0$ and $\nu = 0 \to 1, J = 1 \to 1$) cannot be reliably resolved any more, thus information about the ortho-concentration cannot easily be extracted from ro-vibrational Raman spectroscopy.

3.6   Sample preparation

The crystal was always frozen from the liquid phase (freezing from the gas phase was not possible with the cell used). Gaseous D_2 is stored in two Aluminum storage containers, where one container is used for normal and the second for ortho Deuterium. The preparation of ortho Deuterium was done before the experiments and is described in sec. 3.3. The gaseous D_2 flows into the cell and is subsequently liquefied. The process of freezing is carried out at a temperature close to the triple point (18.7K) and takes typically about 12h. The crystal created this way is fully transparent and clear. In Fig. 3.6 a series of pictures shows the slow phase transition from the liquid to the frozen state. The optical properties of the crystal depend strongly on the speed of the freezing process.

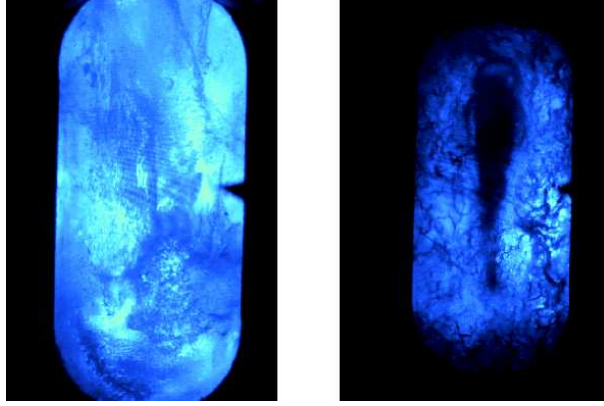Figure 3.13 shows crystals grown at two cooling speeds. The difference

Figure 3.13: Two crystal at 5K that have been grown at two cooling speeds. The right picture shows a crystal grown at 2K/h and the left one at 14K/h.

is clearly visible. An annealing technique was developed in which the Deuterium was kept at a constant temperature for several hours. This annealing procedure greatly improved the crystal homogeneity. Once the crystal reached a temperature of 18 K it was cooled down further to a temperature of 5 K. This last step in the process of creating the final form of the solid Deuterium was performed at a reduced cooling speed: in most cases with a typical cooling speed of $2\,\mathrm{K/h}$. Finally, the temperature of the crystal was varied between 5-10-5 K, and 5-18-5 K. The variation between 5-10 K had almost no effect while between 5-18 K the crystal changed dramatically. The light transmission through the sample as well as the photographs of the crystal slowly cooled and after temperature cycling between 5-10-5 K and 5-18-5 K are shown in the Appendix B.

3.7 Overview of the CN experiment setup

A first experiment to measure the transmission of neutrons through Deuterium was carried out at PSI at the Small Angle Neutron Scattering (SANS-I) instrument [50]. Different target conditions (liquid and solid D_2, for the temperatures 5 K and 18 K, and ortho concentration 67% and 98.5% ortho) were investigated for wavelengths between 5 and 36 Å. The beamtime was one week long.

The incoming neutrons are monochromatized by a mechanical velocity selector and collimated over a length that varied from 1 to 18 m. The monochromator itself has a helical slot, which can rotate along the neutron beam axis. By choosing a defined rotation speed of the velocity selector, only

neutrons within a narrow range in wavelength traverse the slot, while the rest is absorbed in the velocity selector. The selector allows choice of wavelength between 4.5 Å and 40 Å. We chose 5,6,8,10,12,13,17,20,25,29,36 Å for our measurements. The resolution of the wavelengths was 10%(FWHM).

The SANS-I instrument is equipped with a two-dimensional ^{3}He-detector with 128 x 128 elements of 7.5 x 7.5 mm^2 each. The detector can be positioned at any distance between 1.4 and 20 m from the sample. Additionally it can be displaced laterally by 0.5 m inside the large vacuum vessel to increase the accessible range of momentum transfer. Three different positions of the detector were used for the measurements. For small angle scattering a distance of 18 m was used, for the transmission measurement 6 m, and 1.5 m for the scattering.

The measured intensity I of each pixel has to be corrected for dead time. The corrected intensity $\bar{I}$ is [51]

$$\bar{I} = \frac{I}{1 - D_t \frac{I}{t}} \tag{3.1}$$

where I is the number of registered neutrons, D_t the deadtime of the detector $\sim 3.5\,\mu$s and t is the measuring time.
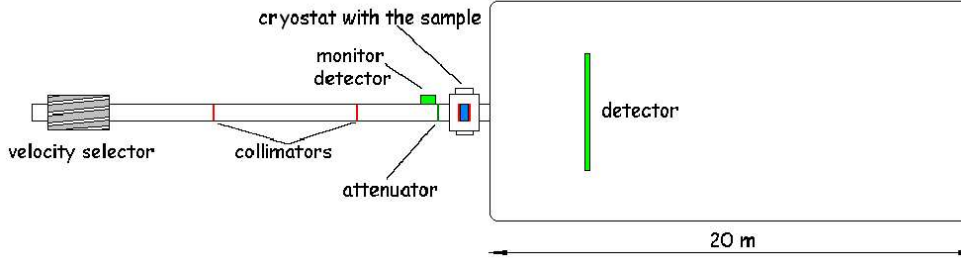
3.7.1 Geometry of the CN experiment

Figure 3.14: The scheme of the CN setup.

A schematic view of the experimental setup is shown in Fig. 3.14. The cold neutrons from SINQ first pass the selector and then are collimated in the neutron flight tube. Neutrons with wavelength of 20 Å and less had to be attenuated for the transmission measurements before they reached the sample. The target cell has two additional collimators made from Cadmium plates, which are mounted on the thermal shielding of the cryostat. An additional monitor detector was mounted close to the beam. This detector

allows measurement of the relative intensity of the beam; the obtained value has been corrected for deadtime.

3.8 Overview of the setup of the VCN/UCN experiment

This experiment was carried out at the Intitute Laue-Langevin (Grenoble, France) on the VCN and UCN beam-lines. A total of 2 reactor cycles (reactor cycle 135-VCN and 136-UCN, 50 days each) had been allocated for these experiments.

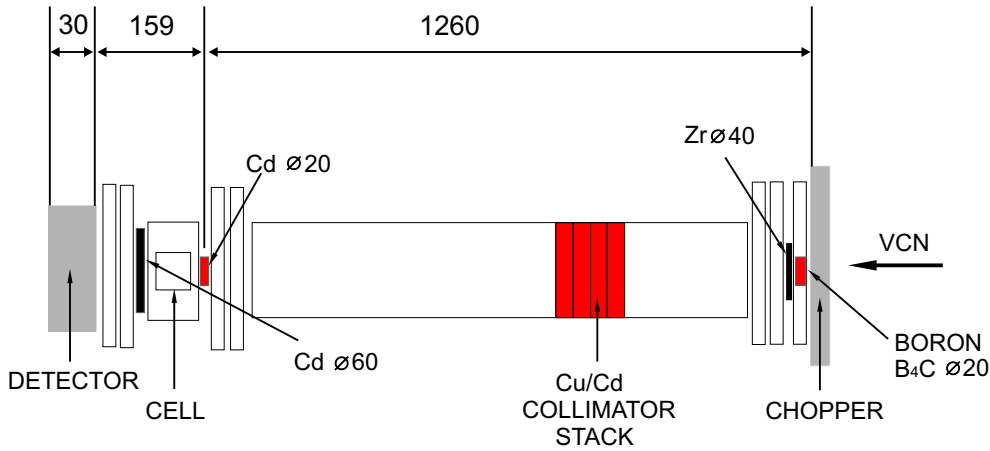### 3.8.1 Geometry of the VCN experiment

Figure 3.15: The scheme of the VCN setup. All values are in mm.

Figure 3.15 shows a schematic view of the experimental setup at the VCN beam position. Neutrons with wavelengths in the range 20Å to 200Å pass through the setup as packets created by the neutron chopper and are detected in a position sensitive micro-strip gas counter. The sD_2 crystal in the target cell with an approximate thickness of 10 mm is placed in the flightpath[1]. During the experiment the detector was located at two positions, "front" and "extended". For the "front" detector position the total length of the flight path is 1434 mm. The collimator assembly has a length of 1260 mm and consists of: (i) a 20 mm diameter boron collimator placed directly after the chopper, (ii) a 20 mm diameter Cadmium collimator placed

---

[1]Distance between the chopper and the middle of the neutron detector.

before the target cell and (iii) four Cd/Cu collimators of total length 150 mm placed 600 mm after the chopper. The reasons for having the detector at two position are (i) to allow calibration of the timing of the trigger for the time-of-flight measurement and (ii) determination of small angles in the scattering measurements.
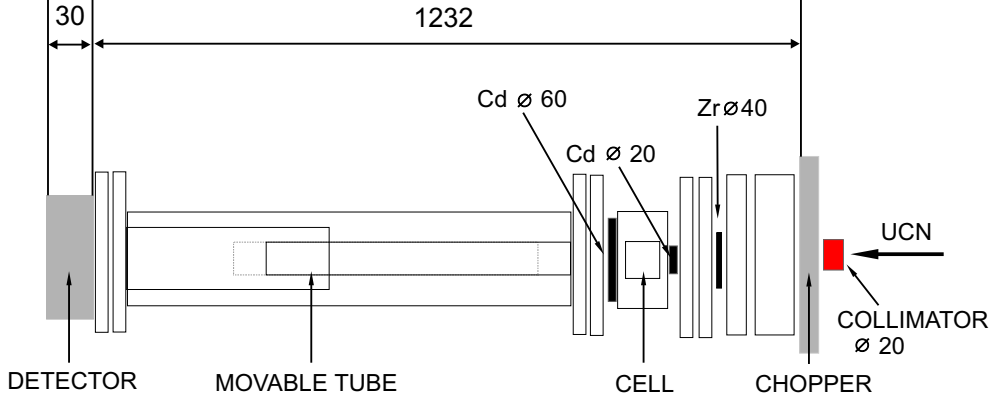

Figure 3.16: The scheme of the UCN setup.

A similar setup was used for the UCN experiment, see Fig. 3.16. For these measurements the cryostat with the sD_2 crystal was placed in the flight path of length 1247 mm directly after the chopper. For the neutron scattering measurements a collimator with a length of 30 mm and a diameter of 20 mm was placed upstream of the chopper. After passing through the cell the neutrons enter a moveable neutron guide. This tube allows for variable the angular acceptance of transmitted and scattered neutrons. The measurement were performed for four different positions of the reflecting neutron guide (0, 20, 60, 100 mm). The distance was measured from the last Cadmium collimator ($\phi 60$ see the Figs. 3.16 and 3.17) so the tube position to the sample was 50, 70, 110, 150 mm, respectively. The diameter of the tube was 68 mm, so the corresponding scattering angles were: 30.96°, 25.90°, 17.175° and 12.77°. The solid angles Ω_n were calculated according to the equation:

$$\Omega_n = \int_0^{2\pi} \int_0^{\theta_n} \sin\theta \, d\theta \, d\phi = 2\pi \int_0^{\theta_n} \sin\theta \, d\theta = 2\pi \left(1 - \cos\theta_n\right) \qquad (3.2)$$

thus $\Omega_1 = 0.89$ sr, $\Omega_2 = 0.63$ sr, $\Omega_3 = 0.28$ sr and $\Omega_4 = 0.16$ sr which correspond to the 0, 20, 60 and 100 mm tube position respectively.

3.8.2 Chopper

All the measurements of the neutron transmission through the crystal have been performed at specific neutron wavelengths selected using a neutron
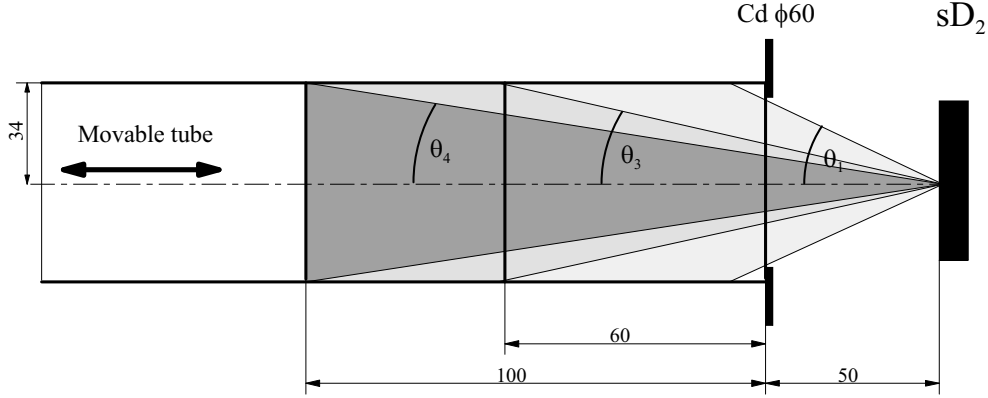
Figure 3.17: The picture shows the part of the UCN setup with the movable tube (see also Fig. 3.16). The θ_1, θ_3 and θ_4 define the neutron scattering angles for 0, 60 and 100 mm tube position respectively. Different gray shading denotes the solid angles for different tube position. For clarity the tube position tube of 20 mm is not drown.

chopper and time-of-flight techniques. For the UCN and VCN measurements different choppers have been used.

3.8.3   VCN chopper

The VCN chopper uses a rotating disk made of Aluminum coated with neutron absorbing Gd and ^{6}LiF layers. It has two slits through which neutrons can pass. A 20 mm diameter boron collimator is placed directly after the chopper and is centered on the beam axis. The chopper was operated at a rotation frequency of $\nu = 7$ Hz. A 5 μs long TTL signal was generated before the slit reached the neutron beam centre. This signal triggers the data acquisition system. The cross section area of the beam that is cut by the chopper slit and the collimator at a given time defines the chopper opening function. It can be calculated by integrating the overlapping area of the slit and collimator as the slit moves through the beam area. The width of the TOF channel (80 μs) defines the time step for this calculation. The chopper opening functions have been calculated for the nominal chopper frequency of $\nu = 7$ Hz and also for a chopper frequency of $\nu = 3$ Hz (some of the measurement were carried out at 3 Hz). The transmission profiles obtained by the opening functions can play an important role in the interpretation of the TOF spectra that are measured: the transmission profiles have been used to deconvolute the raw data.

3.8.4 UCN chopper

The UCN chopper [52] consists of three rotating disks made from polycarbonate: one disk rotates slowly while two other disks rotate at higher speed, where the ratio of the speeds is fixed at 1:6. The 'slow' disk opens a time window of 22 ms with a typical operation frequency of about 3 Hz and produces a neutron pulse. The two fast disks sharpen the rising and falling slope of the pulse. The disks in the chopper are driven by a stepping motor, which is computer-controlled through a "PCI 7324" card and LabView software. The trigger signal needed for the TOF measurements is provided by the light being reflected by one of the reflection sensors mounted on the wheel of the slow disk. It is detected by infrared diodes. The reflector is a 7 mm long piece of Aluminum which together with the rotation speed determines the length of the pulse. To correct for this effect, a shaping stage was applied. The length of the TTL signal, after passing this stage is 5 μs. A full chopper turn takes 864 steps. The stepping motor can be run at a slow enough speed that allows for an experimental determination of the chopper opening function. The stepping motor can also be operated in a way so as to obtain a precise calibration of the TOF spectra.

Detector

The neutron detector, Bidim80 [53], used in both the VCN and UCN experiments was a 2-dimensional micro-strip detector that consists of an MSGC plate placed in a sealed cylindrical metal container filled with a mixture of 50 millibar of ^{3}He and 1 bar of CF_4. The MSGC is made of a semiconductive glass plate with a chromium pattern of strips, the total sensitive area is 80x80 mm^2. The 10 μm wide anodes are engraved on the front side of the plate, the 980 μm cathodes are placed on the rear side of the plate orientated perpendicular to the anodes. The detector use a charge division readout for determine the position. The X and Y position of the detected neutron is determined from pulse height asymmetries of signals from the electrodes in the following way:

$$X = \frac{A_0 - A_1}{A_0 + A_1} \cdot f_x \tag{3.3}$$

$$Y = \frac{A_2 - A_3}{A_2 + A_3} \cdot f_y \tag{3.4}$$

The values of f_x and f_y were found experimentally to be 3.9 cm and 3.65 cm respectively. For details see sec. 4.2.1.

3.8.5 Data Acquisition and Slow Control

In all three experiments the Slow Control setup was identical. All the temperature and pressure data were saved in ASCII format without any compression. The pictures from the Nikon Camera were stored in jpg format in 1500×1000 pixels usually one picture per few minutes. The Raman data were stored in binary format where all pixels from the CCD were written to file one after the other. The neutron data acquisition and the stored data formats were different in the CN experiment and the VCN/UCN experiments.

Slow Control

A scheme of the Slow Control (SC) system is shown in Fig. 3.18. The main part is the Slow Control PC working on Windows OS and controlling the mass spectrometer, the Nikon camera, the temperature and pressure multimetres. A second computer (Raman PC) working on Linux was connected to this PC by standard TCP/IP. A solution with two computers with two operating systems was necessary because the spectrometer was working only under Linux, while Nikon camera only under Windows OS.

The mass spectrometer was connected via a serial port (RS 232p) and application software from Pfeiffer Vacuum was used to control it.

The Maxi Gauge multimeter for pressure readout was connected to second serial port. The LabView application with the library delivered with the device was used to control the multimeter.

The LakeShore temperature controller was connected via the GPIB bus to the PCI GPIB card in the PC. The LabView application, using a LabView library delivered with the device, was used to control the multimeter. This allowed for readout of data from five temperature sensors as well as the setting of the PID parameters for the heaters of the target cell.

The Midas Slow Control Bus (MSCB) system [54] uses RS485 communication protocol to transfer data between MSCB card and MSCB master controller. The master controller itself is connected to the PC via the parallel port. The library delivered with the MSCB system allows for easy access to the devices from the LabView application. The MSCB cards with an 8051 family microcontroller with 8 ADC converters, 2 DAC converters and 8 digital I/O read the signals from pressure gauges, flowmeter, powersupply of the laser and light converter.

The LabView application synchronises all devices, provides the correct file names and timestamps, and saves the data on the RAID drive. The data is saved on a separate directories for temperature, pressure, MSCB, and laser. The corresponding filename was updated every day automatically.

The LabView program also has an electronic logbook where all settings of the PID parameters with date and time are saved.
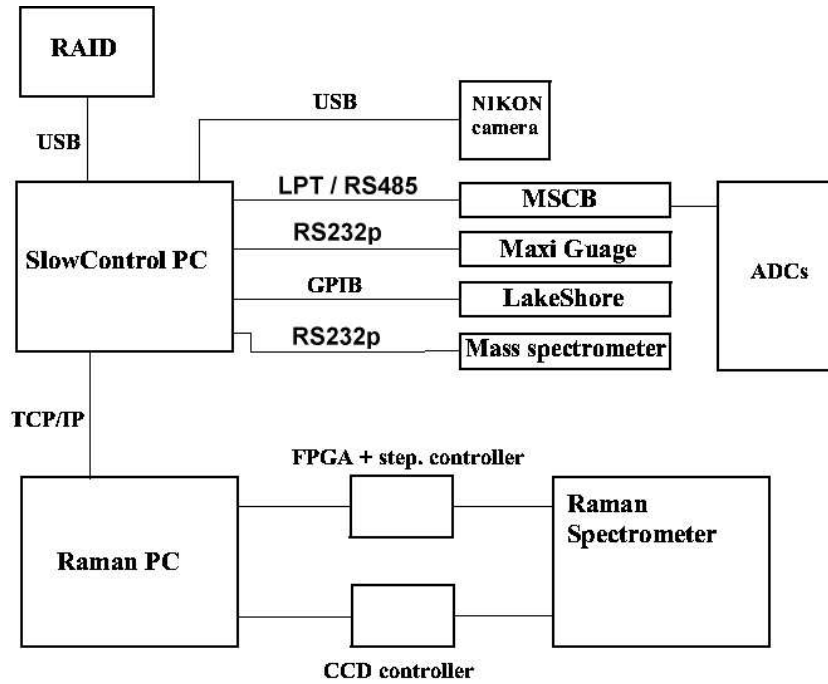

Figure 3.18: Scheme of the slow control system. Two connected computers control all devices used in the experiments. The SlowControl PC and LabView application read all temperature, pressure data and intensity of the laser. The Nikon camera and the mass spectrometer are controlled by software delivered by the producer. The RamanPC cares for Raman spectrometer, controls stepping motor and CCD. Via TCP/IP all Raman data are sent to the RAID system.

The electronic card with FPGA chip was developed for working with stepping motor controlled systems. The card sends the TTL pulses to the motor controller to move the gratings in the spectrometer. The card is connected to the PC via the LPT port. The program for controlling the motors is written in C and was operated from the command line.

The CCD camera works with a dedicated controller which is used for shutter speed control, exposure time, data transfer to the PC, etc. The controller is connected to an ISA card in the Raman PC. The software for control CCD camera was taken from the "Mojo project" (see. Ref. [55]). It was necessary to install a driver in the kernel system. The driver works with kernel version 2.2; the source code version is not accessible. By using the library delivered from the mojo project, Borland Kylix (for GUI - Graphical User Interface) and ROOT (Object Oriented Data Analysis Framework) we built an application for the data analysis of the Raman spectra.

44

Chapter 4

Neutron Scattering on Solid Deuterium

4.1 Cold Neutron Scattering

4.1.1 Measurement and Treatment of the Data

The experiment to measure scattering of cold neutrons on solid Deuterium (sD_2) has been performed at the SANS I instrument at SINQ (PSI). Neutrons scattered inside a sD_2 sample were detected in a position sensitive two dimensional (2D) detector which could be placed at different distances from the sample. The 2-dimentional images of the measured neutrons for different detector position are shown in Fig. 4.1. The analysis is based on the assumption that all scattering is symmetric around the beam axis; this allows the two dimensional information from the detector image to be reduced to one dimension. The scattered intensity as a function of the radius on the detector relative to the beam axis corresponds to the projection of a ring in the two dimensional picture. From this angular distribution of the scattered neutrons $I(\theta)$, or in the general case, $I(Q)$ where Q is the momentum transfer, can be determined. This scattering function contains the information on the structure of the sD_2 crystal and the scattering processes that occur inside.

Before the raw data of the two dimensional detector image can be reduced, two corrections have to be applied. This is done by subtracting: (i) a constant value of the background and (ii) scattering distribution from the empty target cell. The data from the empty cell measurement was corrected for the attenuation of the beam through the Deuterium crystal of $1\,cm$ thickness by using a transmission factor. At a temperature of around $18\,K$ the transmission factor for the empty cell measurement is about $T_r = 0.9$ (see
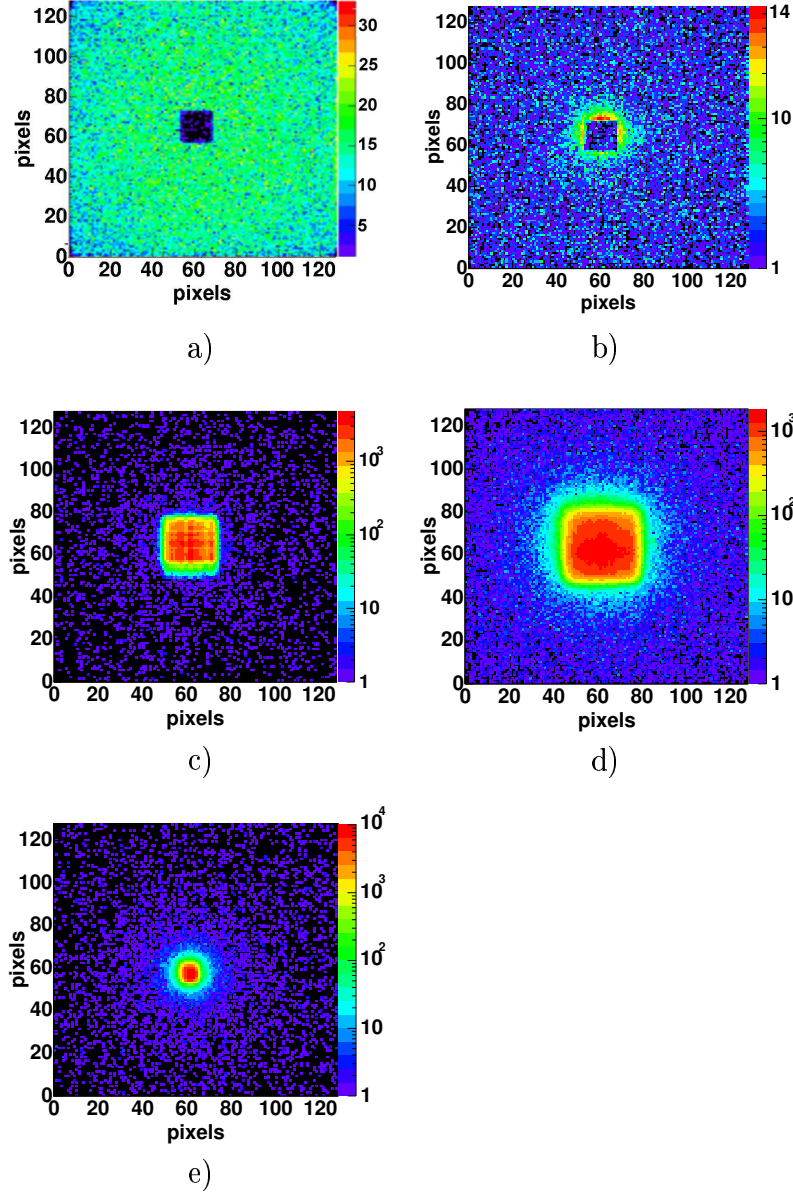
Figure 4.1: Two dimensional images of the measured count rate of the SANS detector, taken during the measurement of the solid Deuterium sample for different configurations of the setup: a) 8 Å, 1.5 m, b) 36 Å, 1.5 m, c) 8 Å, 6 m, d) 36 Å, 6 m, and e) 17 Å, 18 m. The dark square in the middle of the images a) and b) is due to the beam stopper in front of the detector. The square-like structure of the beam spot in Fig. c) is made by attenuator sandwich. The beam stopper and the attenuator was used for reduction of the neutron beam. The sizes and shape of the beam spot change due to different collimation lengths. Bright colors denote higher count rates (each picture has an individual scale).

Eq. B.1). This calculation has been performed for each sample condition, i.e.

for each temperature and ortho-para ratio. The constant background was measured without beam, i.e. when the main shutter was closed. Equation 4.1 shows the data treatment for each pixel of the detector:

$$I_{cor}^{(i)} = (I_{full}^{(i)} - I_{bg}) - T_r \cdot (I_{empty}^{(i)} - I_{bg})$$ (4.1)

where $I_{full}^{(i)}$ and $I_{empty}^{(i)}$ are the intensities of a single pixel from the full and empty cell, respectively; T_r is the transmission factor. The parameter I_{bg} is the average constant background per pixel measured with the main shutter closed, multiplied by the duration of the measurement.

The count rate of each pixel $I_{full}^{(i)}$ and $I_{empty}^{(i)}$ were corrected for the dead time of the detector and normalized to corresponding solid angle Ω. The subtracted values were normalized by the measuring time (for background subtraction) and by the counts of the monitor detector (for the empty cell measurement). The two dimensional data of the detector were then reduced.

Reducing is usually done by defining concentric rings around the beam axis with the same value of $Q + \Delta Q$, where the intensity is the sum of the counts inside the ring normalized to the area of the ring. However, here the data reduction has been done by calculating the scattering angle θ relative to the beam axis and the corresponding momentum transfer Q for each pixel of the detector. This turned out to be more convenient for this analysis due to the finite size of the pixels. This data can be shown as a histogram $I(Q)$ with a suitable bin size ΔQ. Normalization is done by dividing each bin content by its number of pixels. Neutron counts that are in the beam spot area or close to the edge of the detector were removed from the data in the analysis. The handling of pixels with a negative value after background subtraction is described in sec. 4.1.2.

The accessible Q range is defined by the different wavelengths of the incoming neutrons and the different detector positions and can be calculated from the equation:

$$Q = \frac{4\pi}{\lambda} \sin \frac{\theta}{2}$$ (4.2)

where λ is the neutron wavelength and θ is the scattering angle.

As an example, in Fig. 4.2, intensity distributions as a function of Q without corrections are shown for data presented in Fig. 4.1. Such data after correction from different sets of measurements were taken for the further analysis.
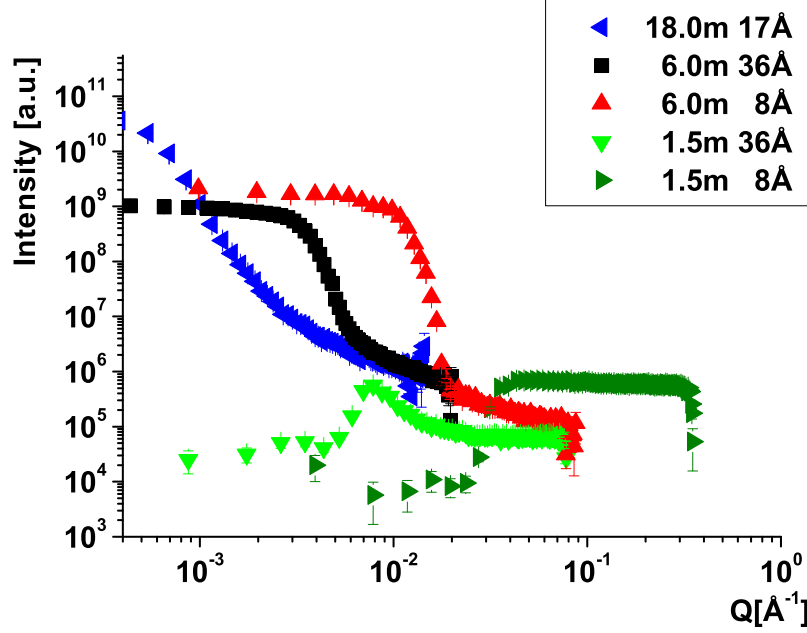
Figure 4.2: Combined average of scattered neutron intensities from different measurements of normal-Deuterium at 18 K as a function of the momentum transfer Q. The graph shows five independent measurements taken at different times and detector positions before normalization by the incident neutron flux, without background and empty cell corrections (2D images are in Fig. 4.1).

4.1.2 Background Treatment

The measurement of the background was performed with the main shutter closed. The incident neutrons are homogeneously distributed over the whole detector area. To obtain the background value for correcting the experimental data, the average value of the intensity per pixel, normalized by the time of the measurement, was used. Only two consecutive measurements of the background were made, both with the detector at a distance of 1.5 m. The results show a rather large difference (see Fig. 4.3) in the averaged intensity per pixel of the detector, $0.513 \cdot 10^{-3}\,\mathrm{s}^{-1}$ and $0.341 \cdot 10^{-3}\,\mathrm{s}^{-1}$.

Based on the background measurement, we assume that the background changed for different measurements and was different for the empty and the full cell measurements. Therefore the proper background correction is not known a priori. The background then has been estimated using two assumptions: (i) the real background value should not be much different from the two measured values and (ii) the scattering intensity from the 18 m
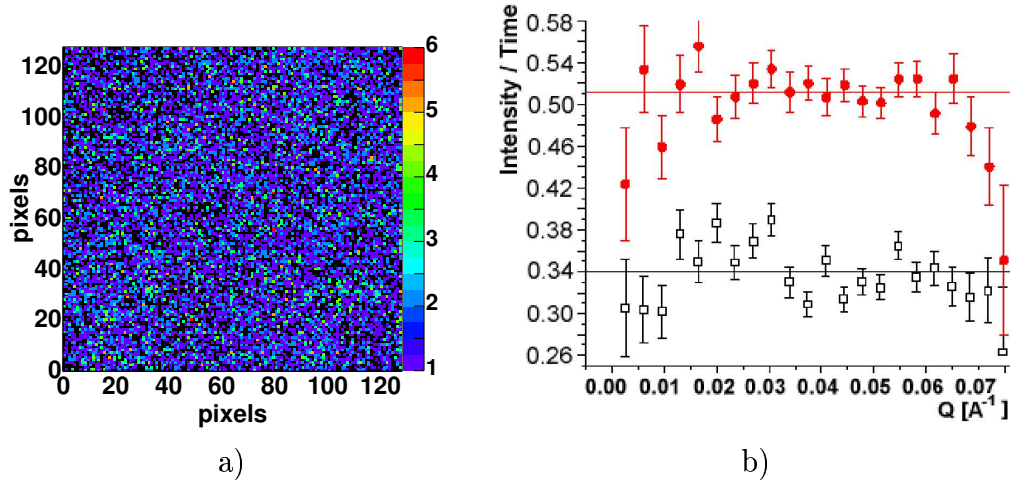
Figure 4.3: a) Two dimensional detector image during a background measurement and b) the related data for the two background measurements. Both graphs are normalized by the number of pixels and the measuring time.

detector distance must overlap the ones obtained at 6 m and 1.5 m distance. By varying the values for the constant background both conditions were fulfilled.

4.1.3 Overlapping

The scattering intensity, $I(\theta)$, for different wavelength of the incoming neutrons and for different detector positions has been measured. The analysis of several hundred data files had to be consistent in order to understand the behavior of the sample. The optical investigations of the crystal showed that the sample changed with time; the influence of the changes on the scattered neutron intensity needs to be checked.

The sD$_2$ crystal was always prepared from the liquid phase. Gaseous Deuterium was liquefied at the triple point (18.7 K) and slowly frozen to 18 K. After measuring at 18 K (different detector positions, different wavelengths of the incoming neutrons) the sample was slowly cooled down to 5 K and then the measurement procedure was repeated. Figures 4.4 and 4.5 show the time dependence of the scattered neutron intensities. For the detector distance of 1.5 m, the intensity changes with time but the slope stays the same. The data has not be normalized to the incoming neutron flux or to the amount of the Deuterium material in the cell, so the levels for different measurements can change while the slope should be the same. For the 18 m position the situation is similar, although for the larger momentum transfers the discrepancy

becomes larger because of low statistics. This has a significant influence on the negative values of the averaged intensity, so these points are discarded. Only regions where the curves overlap are taken into account. The momen-
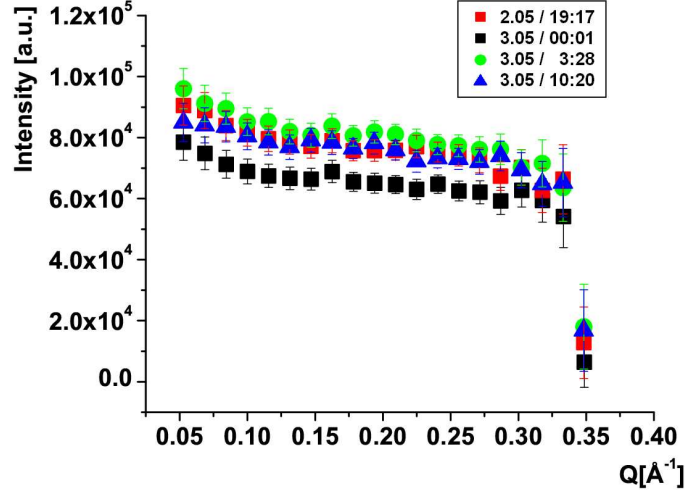

Figure 4.4: Time dependence of the stability of the crystal. The graphs show the intensity distribution as a function of the momentum transfer Q for the 1.5 m detector position measured at different times (denoted by different colors).
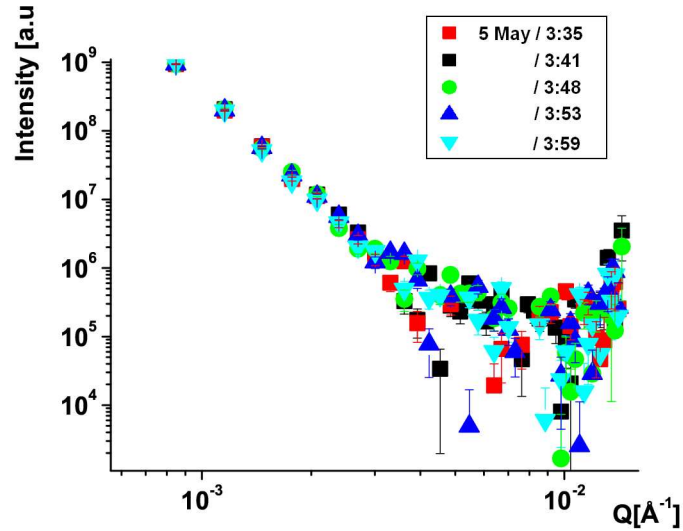

Figure 4.5: Time dependence of the stability of the crystal. The graph shows the intensity distribution as a function of the momentum transfer Q for the 18 m detector position measured at different times (denoted by different colors). The points above the $0.003 \, \text{Å}^{-1}$, because of unknown background, are excluded from the analysis.

50

tum transfer, Q, is measured by varying the neutron wavelength λ and the detector position. An important test is to check if the curves originating from different measurements overlap. In Fig. 4.6 the behavior of different wavelengths for one detector distance can be compared. For 1.5 m distance the curves overlap very well. However, the situation for measurements at 6 m distance is slightly worse. The reason is that the collimation of the neutron beam was set to 1.5 m, which is optimized for transmission measurements (for which high statistic is more important than low divergence).

Usually in a scattering experiment the beam is collimated to have the smallest possible size, otherwise the measurements of the scattering intensity are convoluted with neutrons coming from different position in the beam. For large Q and a small beam spot such a convolution can be omitted and the beam can be assumed to be thin and parallel. For the transmission experiment the collimation is not so crucial. In the experiment the main concern was to enlarge the beam spot sufficiently in order to decrease the count rate per pixel. The neutron count rates for some wavelengths were too high and for the wavelength below 25 Å additional attenuators were placed in the beam before the sample position. The attenuator consist of a sandwich of Cadmium and Boron plates with an array of holes. The resulting structure in the beam profile makes it more difficult to extract accurate information. Fortunately, the necessary scattering information can be obtained from measurements using other settings, at 1.5 m and 18 m detector distance. Therefore the data measured at the detector distance 6 m are excluded from the scattering analysis. The analysis shows that the measurements at different Q ranges are consistent. This means that the data sets overlap. Figures 4.6 and 4.7 show a compilation of the results for a wide range of Q. Measurements with different wavelengths typically have a large overlap in Q, Therefore only the maximum and minimum wave length for each detector distance is used here. The final selected wavelengths were 17 Å at 18 m, and 36 Å and 8 Å at 1.5 m.

4.1.4 Scattering Cross Section

The measurements of transmission and scattering are complementary. In the first, the intensity with and without the sample in the beam spot area are measured. The second method is based on counting neutrons scattered outside the beam spot with and without a sample in the beam. Here, the scattering is discussed while the transmission result are given in Appendix B and ref. [56]

The incoherent cross section can be determined from the measurement at 1.5 m detector distance. Incoherent scattering results has an isotropic

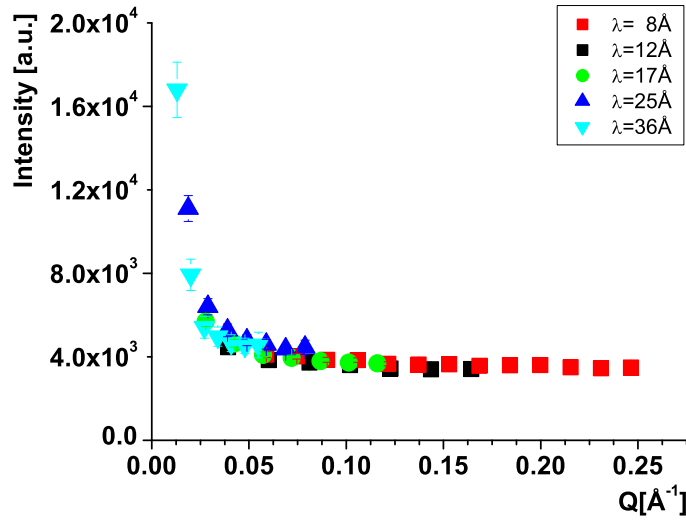distribution of scattered neutrons. Thus, at larger Q after correcting for

Figure 4.6: Intensity distribution of scattered neutrons as a function of momentum transfer Q, measured at a detector distance of $1.5\,\mathrm{m}$ for different incoming neutron wavelengths.
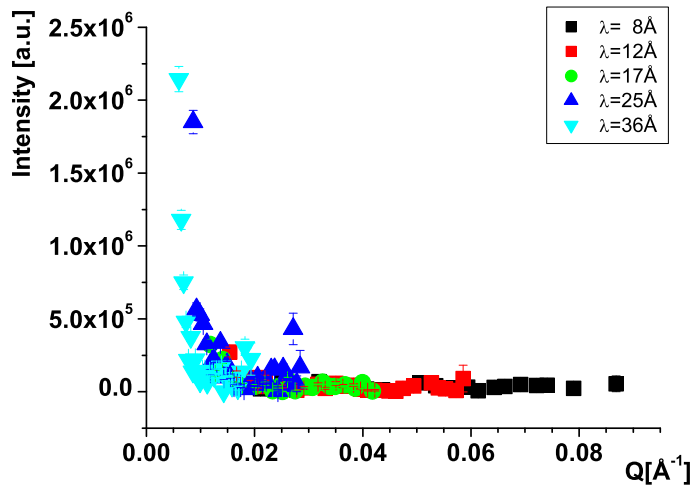

Figure 4.7: Intensity distribution of the scattered neutrons as a function of momentum transfer Q measured at a detector distance of $6\,\mathrm{m}$ for different incoming neutron energies.

the spherical distribution on the flat detector, a flat distribution of scattered neutrons on the one dimensional plot should be found (see Fig. 4.6 or 4.7). Using this flat part, the incoherent cross section σ_{inc} can be calculated:

$$\sigma_{inc} = \frac{\ln(I_{empty}) - \ln(I_{empty} - I_{full})}{d\rho} \tag{4.3}$$

where I_{empty} is the number of neutrons at the sample position, d and ρ are the length and density of the Deuterium and I_{full} is the number of incoherently scattered neutrons. The flat part of the graph of the $I(Q)$ is above $0.1\,\text{Å}^{-1}$, see Fig. 4.6, while below this value other processes dominate which significantly increase the cross section.

The incoming neutron flux could not be measured directly because of the beam stopper placed before the detector. At the 1.5 m position the count rate would have been too high without this. However, at a detector distance of 6 m and for long wavelength ($\lambda = 25\,\text{Å},\ 36\,\text{Å}$) the beam divergence is large enough to reduce the count rate per pixel, so that no beam stopper or attenuator was needed. The flux for the 1.5 m detector distance was estimated from the 6 m detector position (see Fig. 4.8).
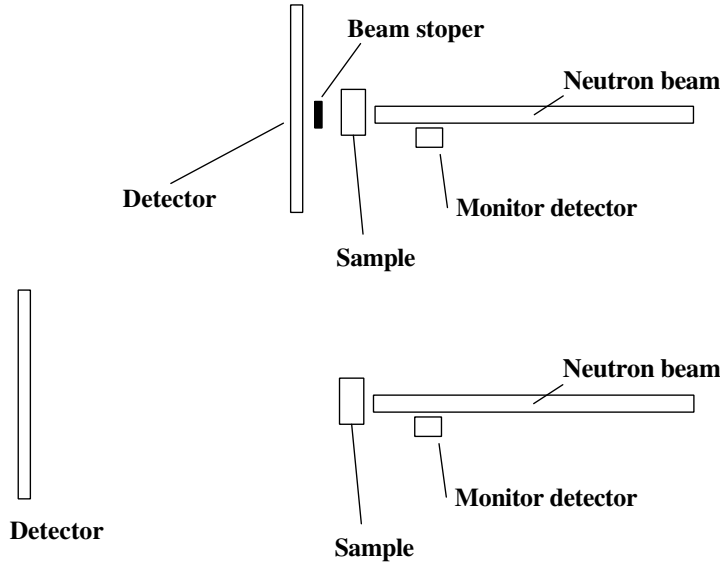

Figure 4.8: Schema of two detector positions. The upper one for the 1.5 m detector position and the beam stopper, and the lower one for the 6 m detector position without beam stopper. If for the same wavelength (e.g. 28 Å) the monitor detector counts in both cases are equal, the neutron flux must be the same. The flux for the 6 m detector position was measured; from that the neutron flux at 1.5 m detector distance was determined.

The influence of multiscattering in the sample was determined using a Monte Carlo (MC) simulation. In the simulation, a geometry similar to the

one used in the experiment was modeled. The momentum of the incoming neutron flux was homogeneous along the beam axis without divergence and the neutron wavelength was set to 25 Å. The distance of the detector from the cell was 1.5 m. Scattering was simulated by applying a scattering function with the literature value for incoherent scattering in Deuterium of 4.1 barn/molecule [19]. When the simulated data was analysed in the same way as the measured data (using Eq. 4.3 and including multiple scattering) the scattering cross section was found to be 4.5 ± 0.5 barns/molecule. To obtain the correct value for the single scattering cross section the multiscattering contribution needs to be extracted. The cross section from the transmission measurement was found to be in a good agreement with the upscattering model (for details see [57, 56] and Appendix B).

4.1.5 Results of the CN experiment

The measurements were performed using two different samples, one with a concentration of ortho-Deuterium of 98.5% and one with a concentration of 66% ortho- and 33% para-Deuterium (normal Deuterium at room temperature). Photographs of the samples at different temperatures are shown in Fig. 4.9. All of the pictures were taken using the same illumination conditions

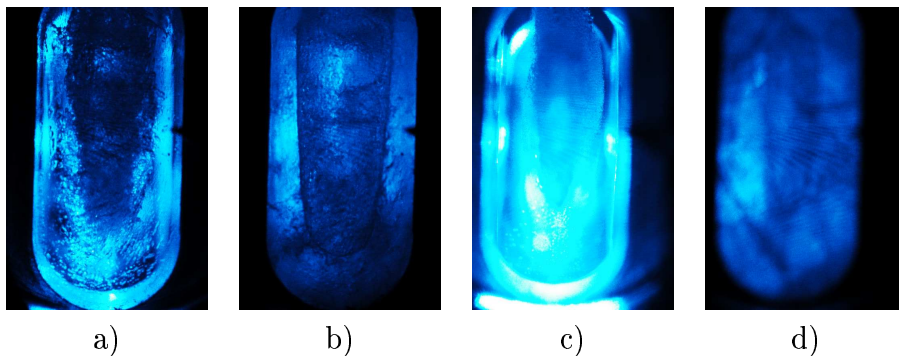a)   b)   c)   d)

Figure 4.9: The photographs show two different samples at two different temperatures; a) ortho Deuterium at 18 K, b) ortho Deuterium at 5 K, c) normal Deuterium at 18 K, and d) normal Deuterium at 5 K.

and camera settings; the brightness of the pictures comes from the properties of the sample itself. The pictures at 5 K have a lower transparency due to cracks. The cracks also have an influence on the scattered neutron intensity. The intensity of the scattered neutrons as a function of momentum transfer for ortho-Deuterium samples is shown in Figs. 4.10 and 4.11 and can be described by:

$$I(Q) = I_{incoh} + P_c \cdot Q^{-4} \tag{4.4}$$

The inverse 4th power of Q is expected for a scattering system where objects have a potential with sharp edges [34] see also sec. 2.3.2. The cracks in the D_2 lead to sharp boundaries between the D_2 ($V_F = 104$ neV) and vacuum. At low Q values, it is important to convolute the power law function Eq. (4.4) with the finite beam size, as seen in Figs. 4.10, 4.11. The value of the parameter P_c (Porod constant), obtained by minimization of the χ^2 are shown in table 4.1. The graphs were normalised to have $d\Sigma/d\Omega = 0.12/4/\pi$ cm^{-1} for the large Q and thus $\sigma_{inc} = 4.1$ barn/molecule.

Table 4.1: Result of fitting the power law function (Eq. 4.4) to the different samples of ortho- and normal-Deuterium.

sample	P_c [cm^{-5}]	χ^2/ndf
ortho-D_2 at 18K	$(1.54 \pm 0.24) \cdot 10^{21}$	2.3
ortho-D_2 at 5K	$(6.57 \pm 0.47) \cdot 10^{21}$	1.9
normal-D_2 at 18K	$(8.48 \pm 0.58) \cdot 10^{21}$	0.6
normal-D_2 at 5K	$(13.3 \pm 1.2) \cdot 10^{21}$	0.7

The specific surface for the ortho-Deuterium crystal at 5 K is about 4 times larger than at 18K ($P_c(o, 5K)/P_c(o, 18K) \sim 4$). It means that there are either four times more crack due to cooling sample to 5 K, or the surface of existing cracks are four times larger. Since the measured scattering function does not have a constant maximum (see the Top part in the Fig. D.1) the origin of increasing specific surface cannot be determined.

4.2 Analysis of very cold neutron scattering

To measure scattering of VCN on solid Deuterium, an experiment was performed at the Institut Laue-Langevin (ILL) on the VCN beamline at the PF2 instrument. The main differences to the experiment described in sec. 4.1 are: (i) a time-of-flight (TOF) method instead of a velocity selector, (ii) a position sensitive detector and vacuum flight path optimized for the VCN spectrum was assembled, (iii) an optimized sample preparation procedure has been developed to avoid excess cracks and to achieve higher transparency at 18 K and (iv) the temperature of the crystal was cycled during the measurement. By cycling the temperature during the measurements, immediate and cumulative effects of cracks and tension produced in the crystal on the neutron scattering as a function of temperature were investigated. This is crucial information for the thermal conditions of the moderator of the new PSI pulsed UCN source. Additionally, two samples with Helium added (0.1 % and 1 %
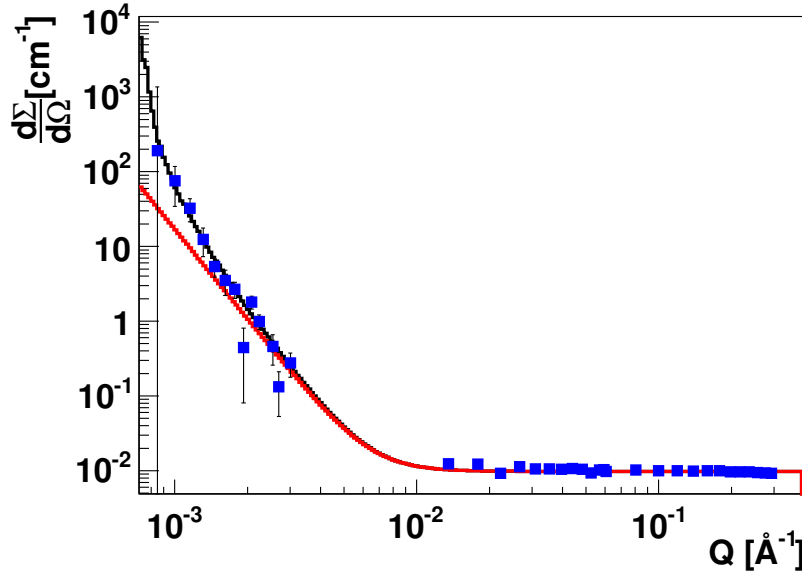
Figure 4.10: The graphs show the differential scattering cross section as a function of momentum transfer Q for the ortho-Deuterium at 18 K. The blue points are measured data. The red curve is the power law function $\sim Q^{-4}$ from which the black curve is obtained by convolution with the finite size of the beam.

of the gas Helium to the gas Deuterium at 300K) were prepared and investigated.

Normal SANS analysis tools cannot be applied to the VCN experiment because of (i) the large effect of gravity, and (ii) the large beam spot with inhomogeneous intensity distribution, where the scattering happened mostly inside the beam and thus the measured angular distribution of scattered neutrons was hidden. The analysis was carried out using an extended version of the Monte Carlo model applied to the CN analysis including gravity and Porod scattering as in Eq. (4.4).

4.2.1 Detector resolution

The first and most important task was the calibration of the detector. Details of the detector are described in sec. 3.8.4 and [53, 56]. The calibration includes measurement of the detector orientation (top, bottom, left, right), as well as the response to the position of the detected neutrons. This was done using a cadmium mask placed in front of the detector. The mask had circular holes distributed asymmetrically (see. Fig. 4.12). The large effect of gravity on the neutron trajectories made the knowledge of the spatial orientation important. The position of the peaks in the two dimensional (2D)
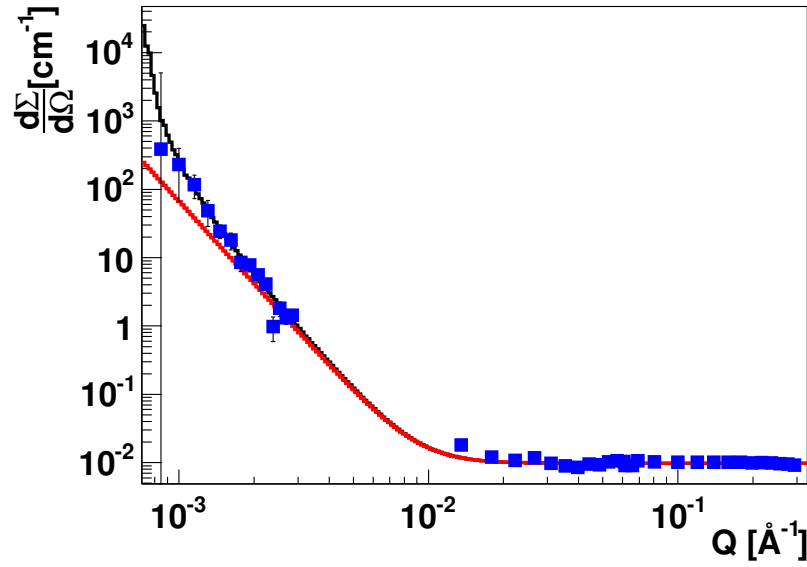
Figure 4.11: The graphs show the differential scattering cross section as a function of momentum transfer Q for the ortho-Deuterium at 5 K. The blue points are measured data. The red curve is the power law function $\sim Q^{-4}$ from which the black curve is obtained by convolution with the finite size of the beam.

detector data was then compared to the holes position on the mask, and determined the linear scaling factors given in Eq. 3.3 and 3.4: $f_x = 3.9$ cm and $f_y = 3.65$ cm.
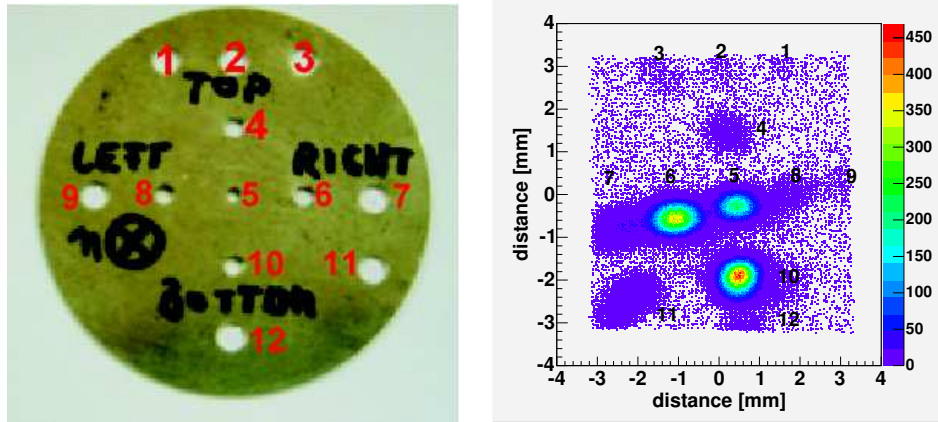

Figure 4.12: The photograph on the left shows the Cadmium mask used for calibration of the detector. The 2D histogram on the right shows the detector image. The numbers denote corresponding holes.

Although the holes in the mask were sharp, the corresponding peaks

57

were broadened due to the finite resolution of the detector. To determine the resolution in each direction, the peaks in the 2D data were projected onto 1D histograms to obtain the maximum intensity in each direction. At the planes of maximum intensity, the 2D data was fit using 1D Gauss functions, in the horizontal (x) and vertical (y) directions and gave peak widths of $\sigma_x = 0.278$ cm, $\sigma_y = 0.1804$ cm.

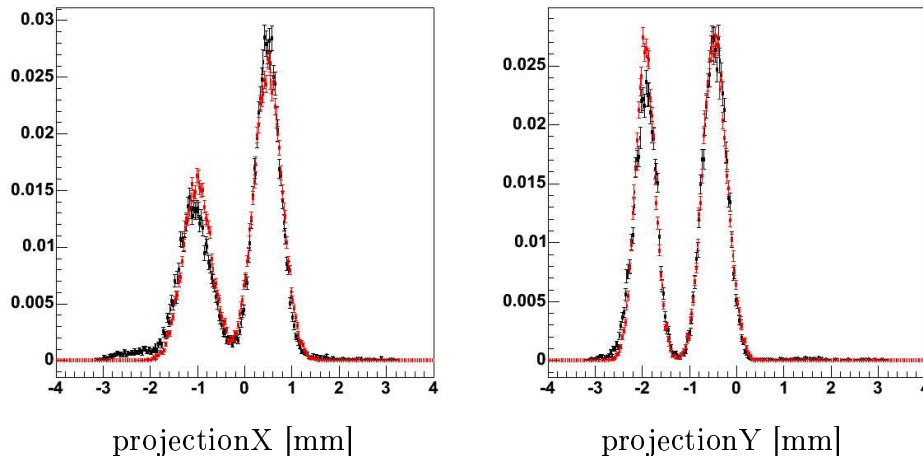projectionX [mm]   projectionY [mm]

Figure 4.13: Projection of the histogram from Fig. 4.12 black points, together with the simulation red points. The left graph shows the projection to the axis-X, and the right one to the axis-Y. The small black bump around (-2;-3) in the left graphs shows the projection of holes number 7 and 11 not taken into account in the simulation.

4.2.2   Beam simulation

To simulate the VCN beam, four aspects had to be taken into account: (i) the neutron wavelength spectrum, (i) inhomogeneous intensity distribution over the beam cross section, (iii) the divergence of the beam and (iv) the influence of gravity. The geometry in the simulation included details of the equipment (collimators, cryostat, detector etc.). The parameters of the simulations were determined by fitting calculated data to the experimental results using a last square fit method.

Initial parameters

The experimental setup was modeled neglecting irrelevant details. The initial wavelength distribution was deduced from a measured TOF spectrum.

Details about the TOF measurement, can be found in ref. [56]. Due to the large spatial inhomogeneity of the beam, (as also found in other independent experiments [58, 59] see Fig. 4.14), the correct optimalization of the initial condition was challenging and the solution might not be unique. Because
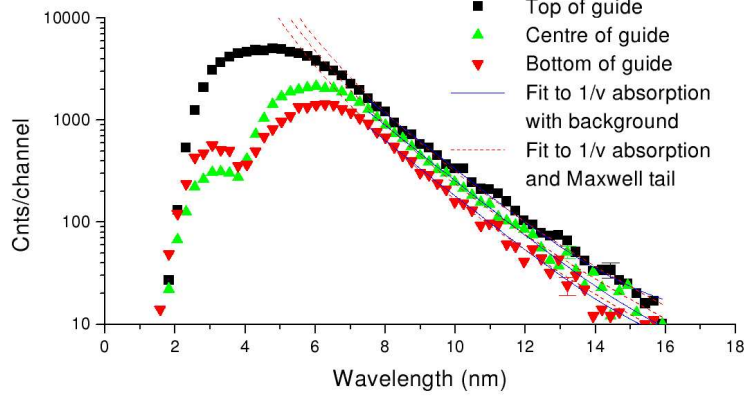

Figure 4.14: Time-of-flight measurement of the spectrum at the exit of the vertical neutron guide from Ref. [58]. The spectrum is clearly not homogeneous over the beam cross section in the $\lambda = $ 2-5 nm (20-50 Å) range.

the only experimental information of the beam were the neutron's x and y positions on the detector plane and their wavelength from the time-of-flight, the simulation was based on "back propagation" of the neutrons from the detector through the setup to the VCN guide. The "back propagation" algorithm consisted of two steps, deconvolution of the 2D data images and then the actual "back propagation". Details of the deconvolution and "back propagation" procedure are given in Appendix C.

4.2.3 VCN scattering in sD$_2$

To simulate scattering of the VCN beam in the sD$_2$ target, a model for the sD$_2$ crystal was built consisting of two processes: (i) incoherent scattering with a cross section of 4.1 barn/molecule [19] and small angle scattering, as was derived from the CN analysis. The SANS process was described by one parameter, the Porod constant. The calculation of the cross section as a function of wavelength was required for the Geant4 simulation. The result of the CN data analysis was the differential scattering cross section as a function of momentum transfer $d\Sigma/dQ$, which was then transformed into the corresponding wavelength dependent cross section for a SANS process $\Sigma(Q)$.

The transformation required a cutoff for small momentum transfer. Details of the calculations and the cutoff at small Q are given in Appendix D.

4.2.4 Method of Analysis

The data analysis was made by finding the value of the Porod constant that gives the minimum χ^2 when the simulated distribution are compared to the measured one. The minimum of the χ^2 and corresponding Porod constant was found by fitting a quadratic function as shown in Fig. 4.15. If the reduced χ^2 is about $\chi^2/ndf \approx 1$, the statistical uncertainty of Porod constant can be found by calculating $\chi^2 + 1$. In the analyzed samples χ^2/ndf was usually between 4 and 20, indicating large systematic uncertainties which were dominating the statistic uncertainties.

The VCN beam distribution was simulated independently for several wavelengths (see Appendix C); The analysis was carried out using the χ^2/ndf for the optimized Porod constant as a function of the wavelength. The result for the Deuterium sample at 18 K and 5 K is seen in Fig. 4.16. For a few points below 45 Å where $\chi^2/ndf = 0$, the simulation is deemed to have failed and the points were rejected from the analysis. It seemed that for wavelengths below 45 Å, the beam parametrization was not working properly. So the analysis was continued only for neutrons with wavelength above 45 Å. For a few samples (after temperature cycling 5-18 K) the points above 110 Å had to be discarded because the fit did not converge.

The Porod constants were obtained by calculating the RMS value in an appropriate range, see Fig. 4.17. The model of the small angle scattering assumed the Porod constant to be constant for all wavelengths. However, the result of the simulations indicated a wavelength dependence for some of the samples. This effect was not visible for the samples with a nicely prepared crystal of Deuterium at 18 K, as almost no scattering was observed and the Porod constant was consistent with zero. The uncertainty of the Porod constant was estimated as a minimum and maximum value for the range of the validated reduced χ^2, see Fig. 4.16 and Fig. 4.17.

The wavelength dependency of the Porod constant suggests that either neutrons with different wavelengths see "different crystals" or there is a systematic effect not taken into account. A possible explanation is that the model of Deuterium assumes cylindrical symmetry. Because cracks in the crystals break the symmetry, a discrepancy between the symmetrical model and the data appeared. This effect was not present for crystals at 18 K where there were visually no cracks present. Cooling down the sample caused cracks to appear due to the 2% increase in density for crystalline Deuterium at 5 K compared to 18 K. The inhomogeneity in the distribution of the cracks across
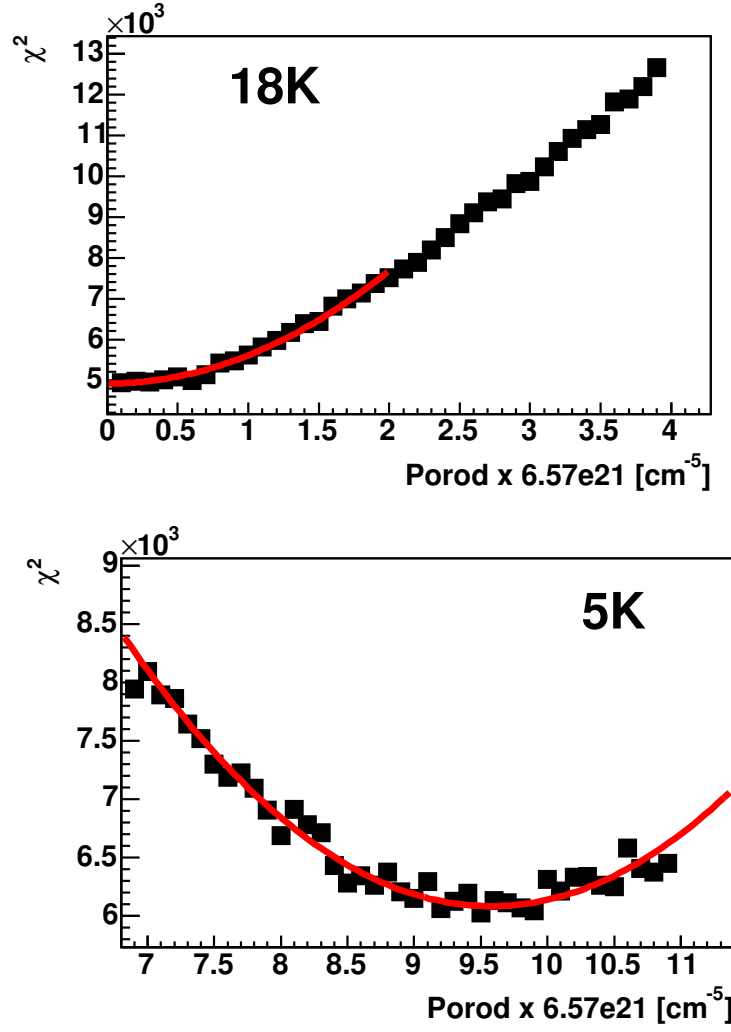
Figure 4.15: The graph shows the χ^2 calculated between 2D histograms measured with Deuterium sample at 18 K and simulations with different Porod constant. On the top for Deuterium at 18K and the bottom for Deuterium at 5K. The number of degree of freedom (*ndf*) is given by the number of pixels of the 2D histogram and typically ∼900.

the crystal could cause asymmetric neutron scattering.

Detailed analysis of the asymmetry as a function of wavelength showed that a few bins were spoiled in the 2D data images. However, after adding up all the wavelengths the effect increased. The influence of the asymmetry was tested by removing the more spoiled bins from the data and the simulations. Removing the bins was done in two independent ways; first by cutting out bins with 10 and second 5 standard deviations between counts in the simulation and the data. This cut led to a more symmetrical output and
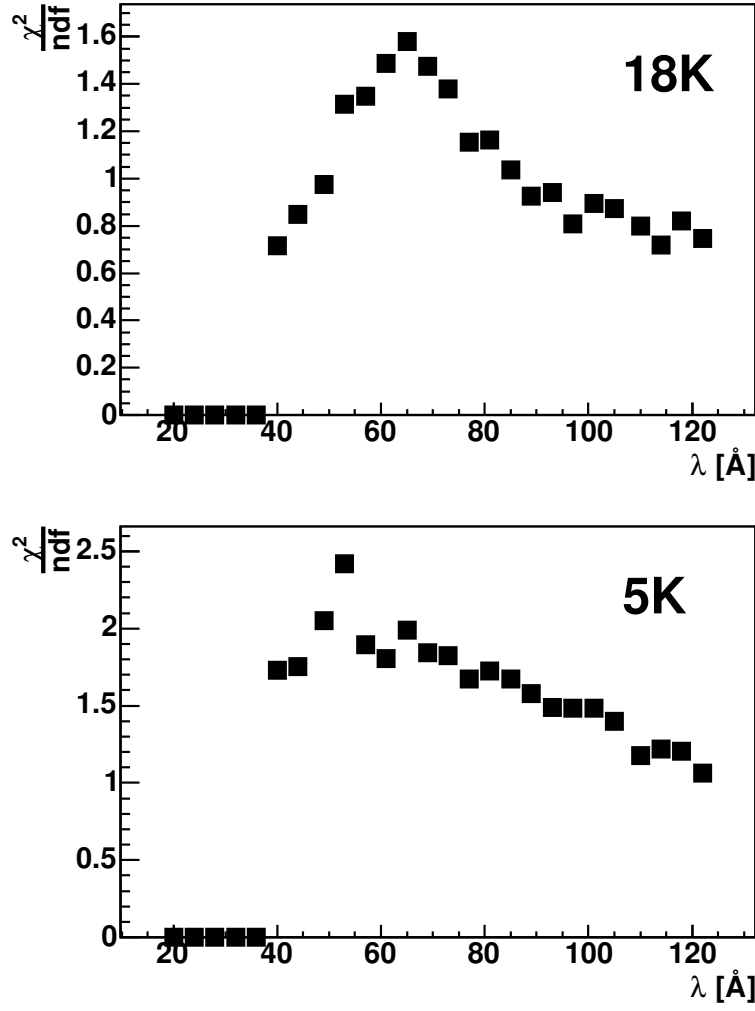
Figure 4.16: The graph shows χ^2/ndf as a function of lambda for Deuterium at 18 K (top) and 5 K (bottom).

with the χ^2/ndf closer to one. Unfortunately, such a procedure could not be applied to all samples. For the samples with the largest observed asymmetry, the removal of more bins was necessary; this made a comparison of simulation and data problematic. As this procedure did not lead to a significant improvement it was not applied for extracting the final result.

4.2.5 Results and conclusion

During the VCN experiment several samples of solid Deuterium at different temperatures were measured. An overview of the various samples together
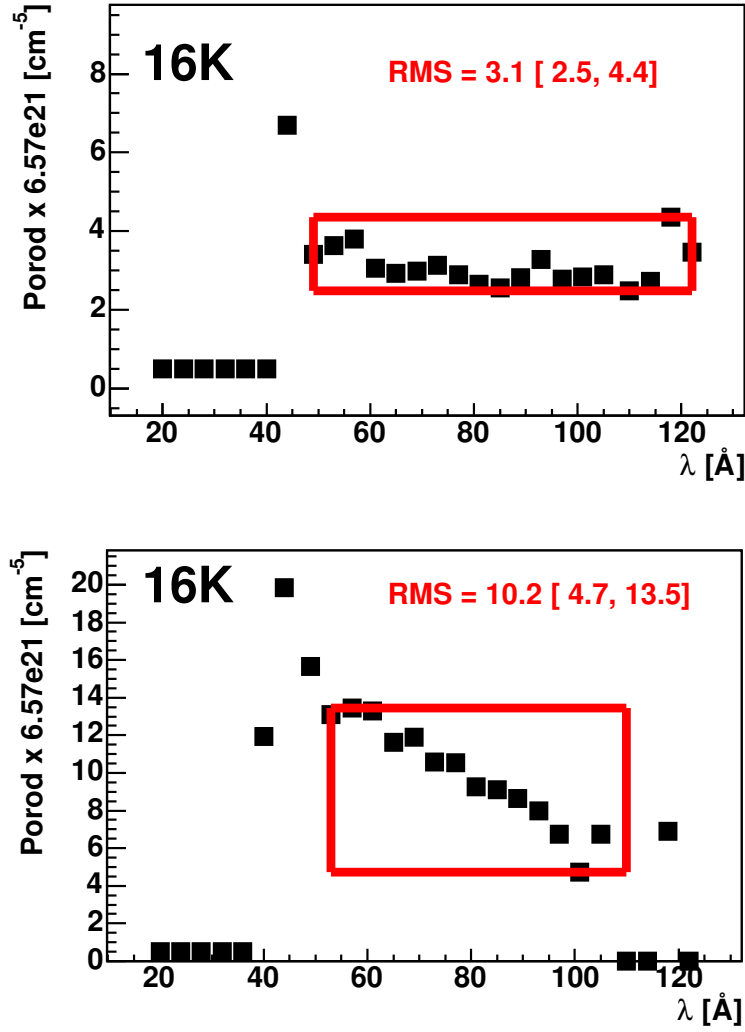
Figure 4.17: The graph shows the Porod constant (RMS) obtained from simulations as a function of wavelength for one data measurement and different wavelengths. The top graph is for Deuterium at 16 K, the bottom graph for Deuterium at 5 K.

with the obtained Porod parameter is given in Table 4.2.

Only in a few cases it was possible to compare the results obtained from CN and VCN scattering directly. During the experiment with cold neutrons the temperature cycling and samples with helium mixture were not used.

It should be noted that different instruments were used for the CN and VCN experiments, which also required different measurement methods. Each sample was prepared differently and the analysis was different for the two experiments. Whereas the uncertainties determined in the analysis account for the different experimental situations, the quality of the crystal cannot
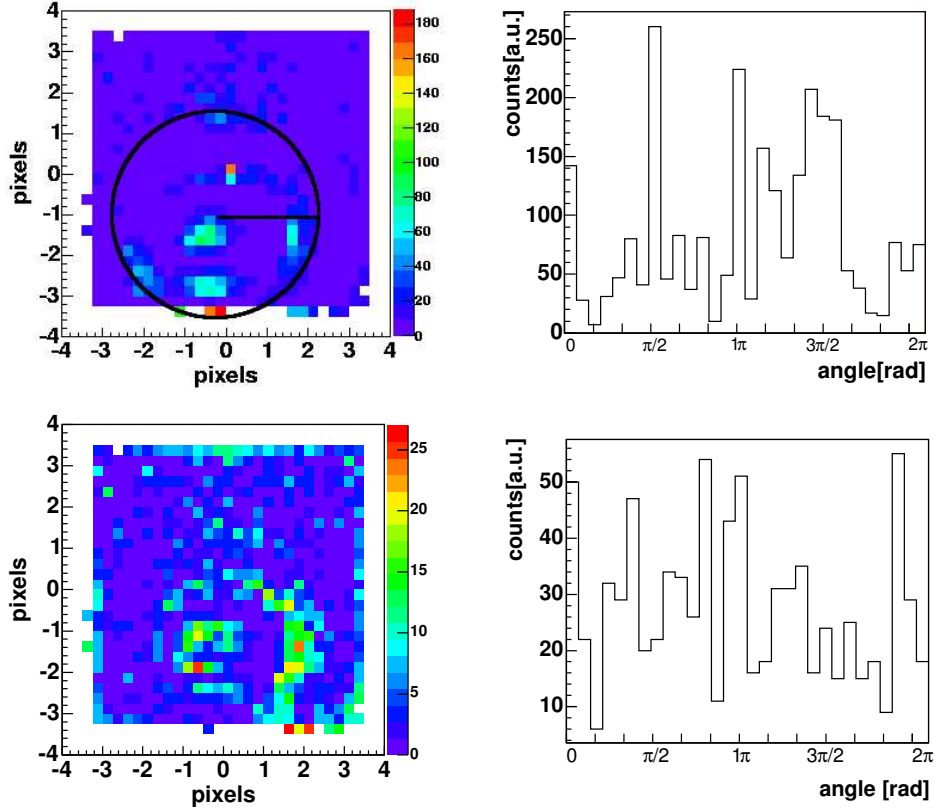
Figure 4.18: The left 2D histograms show the difference between simulation and the data for a deuterium crystal at 5K without bin removing (top) and after bin removing with cut 5 standard deviation (bottom). The colors denote standard deviation scale. The right graphs show the radial sum of the 2D histograms from the left side. The sum is calculated in both cases inside a circle with a given radius (as it is seen in the top left histogram) and anti-clockwise rotation.

be taken into account reliably, especially as we were still learning how to grow crystals properly (compare photograph on Figs. 4.9 and 3.6). In the second experiment, with very cold neutrons, the Deuterium crystals were grown using a much slower procedure (freezing from liquid phase to solid at 18 K are up to 18 hours), and hence the crystals at 18 K were as transparent as liquid and had no visible cracks.

At 18 K both experiments gave a consistent result for the Porod constant. During cooling down, at about 16 K a large number of cracks developed very quickly as can be seen in the two photographs, taken within a few minutes, shown in Fig. 4.19. Cooling down to 5 K resulted in more cracks and a less transparent crystal.

A crystal frozen using a mixture including Helium did not break at 16 K

Table 4.2: Overview of all measured samples in the experiment with very cold neutrons. The value of P_c is a RMS value calculated in the range specified in the brackets (see also Fig. 4.17).

| Sample	Temperature [K]	$P_c \cdot e21 [cm^{-5}]$	Comment
ortho-D_2	18	$0.1(0.0 \div 2.6)$	slow cooling
ortho-D_2	16	$20.3(16.4 \div 28.9)$	slow cooling
ortho-D_2	14	$51.9(13.8 \div 89.4)$	slow cooling
ortho-D_2	12	$59.7(21.0 \div 96.5)$	slow cooling
ortho-D_2	10	$65.7(32.8 \div 103)$	slow cooling
ortho-D_2	7	$68.9(36.1 \div 105)$	slow cooling
ortho-D_2	5	$67.0(30.8 \div 88.7)$	slow cooling
ortho-D_2	18	$44.6(0 \div 76.2)$	fast warming to 18 K
ortho-D_2	5	$322(0 \div 611)$	fast cooling to 5 K
ortho-D_2	5	$565(321 \div 827)$	after I cycling 5-18 K
ortho-D_2	5	$630(455 \div 920)$	after II cycling 5-18 K
sD_2+0.1%He	18	$3.3(0 \div 5.9)$	slow cooling
sD_2+0.1%He	14	$2.6(0 \div 5.9)$	slow cooling
sD_2+0.1%He	10	$14.4(8.5 \div 19.1)$	slow cooling
sD_2+0.1%He	5	$17.7(11.8 \div 23.0)$	slow cooling
sD_2+0.1%He	5	$14.5(6.5 \div 18.4)$	temperature cycling
sD_2+0.1%He	5	$228(120 \div 300)$	temperature cycling
sD_2+1%He	18	$2.6(0.0 \div 4.6)$	slow cooling
sD_2+1%He	5	$53.2(21.0 \div 79.5)$	slow cooling
sD_2+1%He	5	$66.4(34.8 \div 95)$	after cycling 5-10 K
sD_2+1%He	5	$223(120 \div 290)$	after cycling 5-18 K

a)   b)   c)   d)
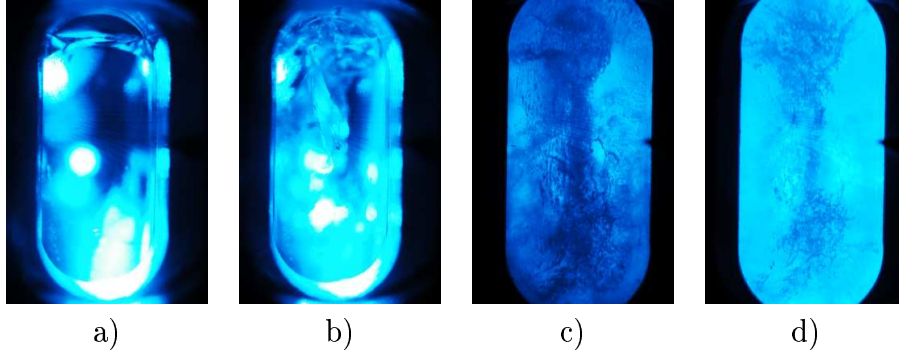
Figure 4.19: Series of photographs showing a) a nice Deuterium crystal at 18 K; b) Deuterium at 16 K after first cracks occurred ; c) Deuterium at 5 K, d) Deuterium at 18 K after fast warming from 5 K.

and generally had less cracks. It was suggested [60] that Helium might help decreased tension in the crystal by providing a better cooling when the crystal contracts. This could result in less cracks and would be the explanation of the smaller Porod constant for the Deuterium sample with 0.1% Helium admixture. Adding more Helium results in a larger asymmetry in the neutron scattering patterns, however the sample was cooled down faster and the result cannot be directly compared. Other sources [61] report that presence of Helium gas had devastating effect for the crystal. One may conclude that producing nice crystals and the effect of He depends on the specific cryostat cell.

Temperature cycling between 5 K and 10 K did not change the Porod constant by much, which is the most important result in the context of the PSI UCN source as it is planned to operate it between 5-8 K. The measurements show that the temperature should be kept below 10 K otherwise the crystal could be destroyed, resulting in a significantly decreased UCN extraction. The effect of different D_2 treatment can also be seen from the VCN beam spots as is shown in Fig. 4.20.

4.3 Analysis of ultracold neutron scattering

In the third experiment, the scattering cross sections of UCN on solid Deuterium were measured at the Institut Laue-Langevin (ILL) at the PF2 instrument at the UCN-TES beamline. The setup for the experiments described in sec. 4.1 and 4.2 was modified for the different energy range of neutrons and the different beamline. Neutrons with energies in the UCN regime behave more like a gas rather than collimated beam. Thus, the direct measurement of the angular distribution of UCN, using 2D position sensitive detector, is difficult. Instead, a UCN guide with an adjustable reflecting tube inside an absorbing outer tube was mounted in the flightpath between sample and detector. By moving the (specularly) reflecting neutron guide tube closer to and further from the Deuterium sample, the accepted solid angle was changed allowing scattered neutrons to be counted at the different solid angle. The advantage of using a moving tube was that the neutron flight path was always the same, independent on the position, (see Figs. 3.16 and 3.17). The detector in the UCN experiment was the same as in VCN experiment, but here used only as a neutron counter. For the time-of-flight measurement we used a chopper that was optimized for UCN [52]. The analysis of the scattering data was carried out using an extended version of the Monte Carlo model applied to the CN (sec. 4.1) and VCN scattering (sec. 4.2) analysis.
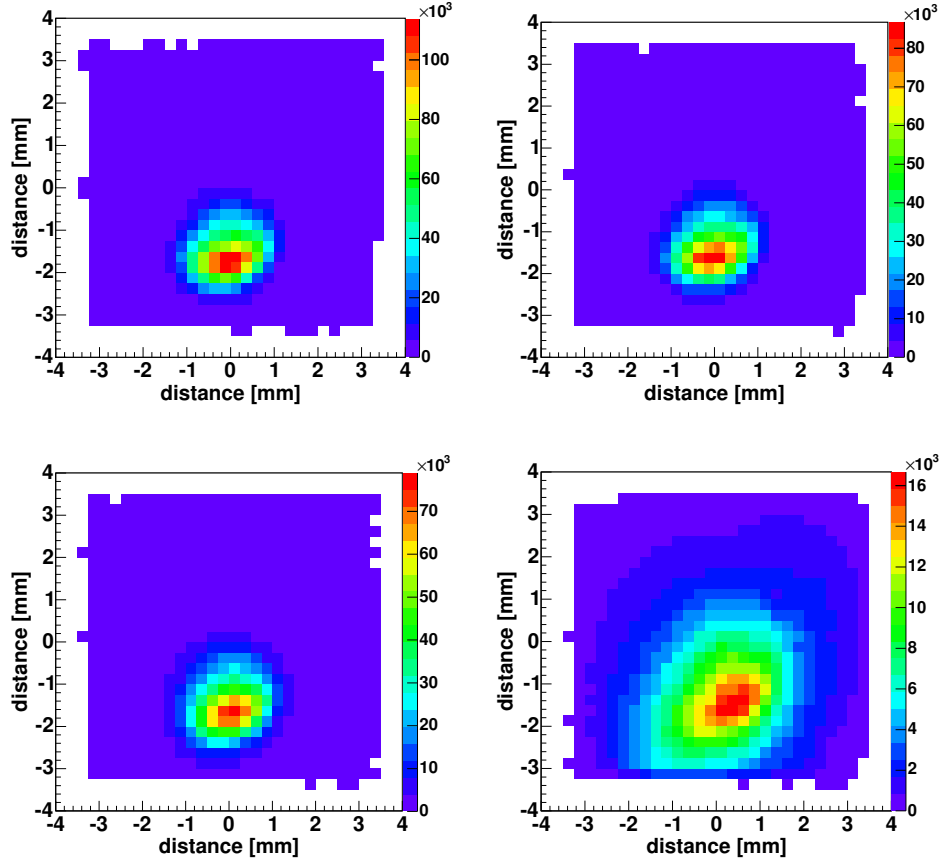
Figure 4.20: Series of the detector images: top left empty cell, top right Deuterium crystal at 18 K, bottom left Deuterium at 5 K, d) Deuterium at 5 K after temperature cycling 5-18 K.

4.3.1 Simulation of the UCN beam

In order to simulate the scattering data, the UCN beam had to be parametrized. Gravity and the complete geometry of the experimental setup together with the adjustable flight path was implemented in Geant4. The initial parameters of the beam were chosen as follows: (i) the wavelength distribution for all momentum directions was assumed to be similar to that measured with TOF technique and calculated by sampling a measured TOF spectrum, (ii) the initial position of neutrons was assumed homogeneous over the whole beam cross section, and (iii) the initial direction followed a cosine distribution around the beam axis. The cosine distribution is the most appropriate for the neutron distribution in neutron guides [5].

In order to reproduce the empty cell measurement for the different re-

flecting tube position for 0, 20, 60 and 100 mm (for details see Fig. 3.17), it was necessary to add diffuse scattering by the thermal Al shield with roughness parameter $\sigma = 25°$ (as was found in [62]) and on the Al windows equal $\sigma = 45°$. The windows are less smooth than Al foil, because they are produced from a piece of Aluminum without polishing.

4.3.2 UCN scattering

In addition to scattering caused by the surface roughness of the Al windows and Al foils, the following processes were treated in the simulation: (i) absorption on Deuterium and on Hydrogen contamination (the maximum possible Hydrogen contamination c_H was 0.0005). Here, the scattering cross sections for Deuterium and Hydrogen were taken from [19], (ii) incoherent scattering on solid Deuterium, using cross section data from [19], (iii) temperature dependent upscattering of UCN on Deuterium molecules according to [57], (iv) upscattering on para-Deuterium (by absorbing energy from conversion of para-Deuterium into the lower energy state ortho-Deuterium), as it was calculated by [17], (v) small angle scattering, using the model from the CN and VCN analysis (see secs. 4.1 and 4.2). Because of the limited angular resolution of the scattering data (only four different tube positions were measured), the analysis is based on completely reproducing in the simulation the measured time-of-flight for all positions of the tube.

In order to reproduce the measured TOF data, it was necessary to add an additional isotropic elastic scattering process (similar to incoherent elastic scattering), which was independent of wavelength, and the cross section for this process was changed with each sample.

For a nicely prepared, transparent Deuterium crystal at 18 K, the additional scattering cross section is equal to 2.5 barn and it increased to 9.67 barn when the temperature is lowered to 5 K. After temperature cycling between 5-10-5 K, the cross section increased to more than 11 barn and after cycling 5-18-5 K to about 33 barn (see also [57] and Appendix B Fig. B.2).

In Figs. 4.21 and 4.22 the measured and the simulated neutron spectra for 18 K and 5 K are shown respectively. A comprehensive list of UCN measurements is given in Table 4.3.

68

Table 4.3: Overview of the different samples measured.

| temperature [K]	P_c 1×10^{21} [cm^{-5}]	I_c [barn]	tube position [cm]	comments
18	$0 \div 1$	2.44 ± 0.38	0, 100	slowly cooling
16-14	$0 \div 2$	5.5 ± 0.3	0	slowly cooling
14-12	$0 \div 2$	7.52 ± 0.5	0	slowly cooling
12-10	$0 \div 4.6$	8.86 ± 0.4	0	slowly cooling
10-8	$0 \div 4.6$	9.53 ± 0.5	0	slowly cooling
8-6	$0 \div 4.6$	9.6 ± 0.5	0	slowly cooling
5	3.09 ± 1.97	9.67 ± 0.3	0, 20, 60, 100	slowly cooling
5	3.94 ± 1.05	11.76 ± 0.38	0, 20, 60, 100	after cycling 5-10 K
5	48.6 ± 3.29	33.05 ± 0.05	0, 20, 60, 100	after cycling 5-18 K
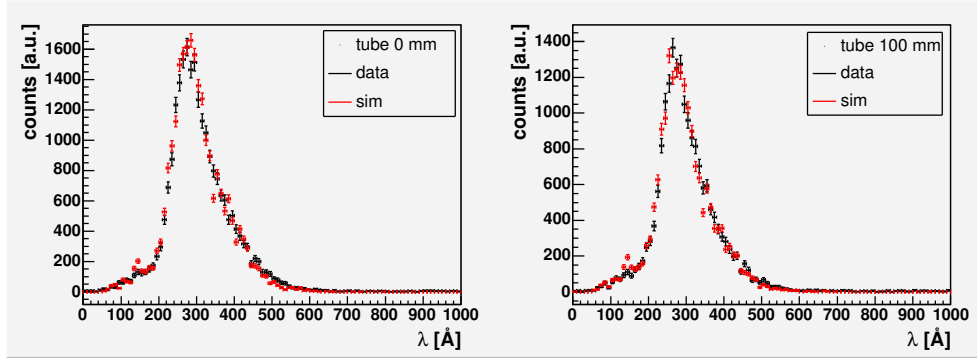
Figure 4.21: The graphs show the measured neutron spectrum together with the result of the simulations for the deuterium crystal at 18 K, for two tube positions.

4.4   Summary of the analysis

In this section the results of the analysis of the CN, VCN and UCN will be summarized.

- The first experiment using cold neutrons was performed at the SANS I instrument at SINQ. This instrument is commonly used to investigate structure of the samples, thus the method of the analysis as well as the statistical and the systematic effects are well understand. The scattering data, which was obtained, can be described using the function $I_{incoh} + P_c \cdot Q^{-4}$, referred to as the Porod-law. The value of the Porod parameter was found to be $P_c = (1.54 \pm 0.24) \cdot 10^{21}$ cm^{-5} for
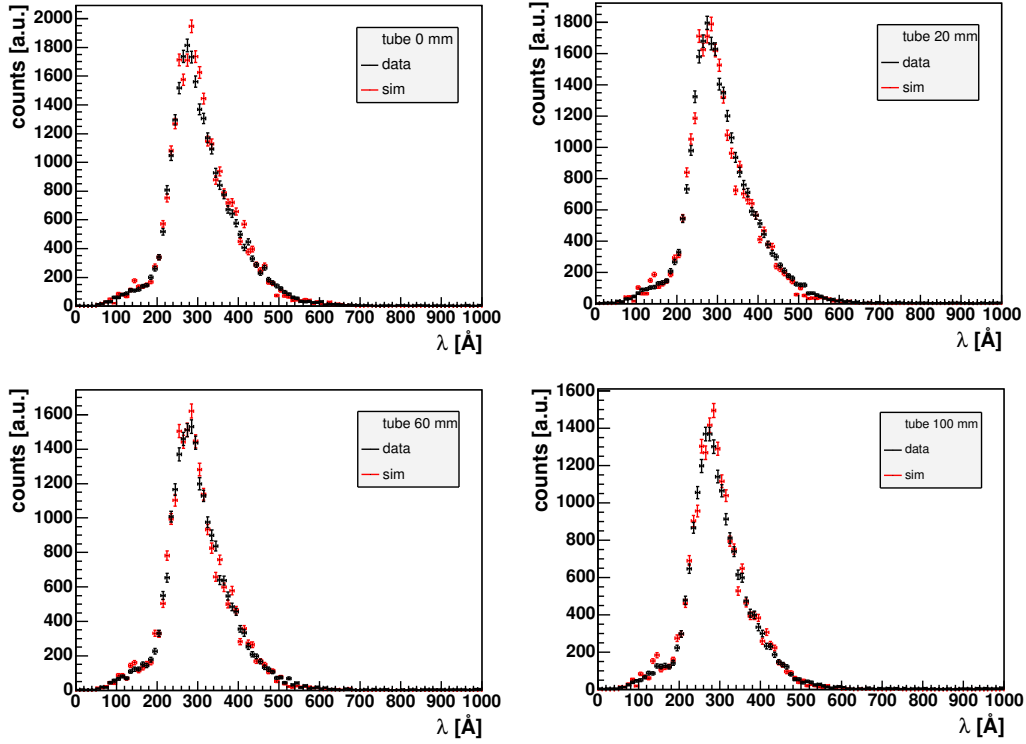
Figure 4.22: The graphs show the measured neutron spectrum together with the result of the simulations for the deuterium crystal at 5 K, for various tube positions.

ortho-Deuterium at 18 K and $P_c = (6.57 \pm 0.47) \cdot 10^{21}$ cm^{-5} for the ortho-Deuterium at 5 K. The Porod constant is proportional to the specific surface S_p, and was found that it is about four times larger for the crystal at 5 K than at 18 K. This means that either the number of cracks increases during cooling or the cracks increase their size four times. Since our measured data does not cover the region of the absolute maximum (which should appeared at some small Q) the exact solution and size of the scatter object is not known. It was concluded that scattering occurs on the cracks and based on that the model of the Deuterium was built.

- The second experiment was based on a similar concept but used a different experimental setup, modified for scattering of very cold neutrons on similar samples. The experiment was carried out at the PF2 instrument at ILL. The neutron beam was very inhomogeneous in space and momentum, varying with wavelength, thus requiring an elaborate Monte Carlo simulations. Most scattering happened within the spacial dimen-

70

sions of the beam which made analysis difficult. The results from this measurement confirm the results from the cold neutron experiment, however, with reduced accuracy due to the larger systematic effects. The most interesting results are: at 18K $P_c = 0.67\,(0 \div 2.63) \cdot 10^{21}$ cm^{-5} and at 5K $P_c = 67\,(30.9 \div 88.7) \cdot 10^{21}$ cm^{-5}. Additionally, measurements with Helium added to the sample have been performed. It turns out that in the presence of Helium, less scattering is observed. This leads to the conclusion that Helium acts as a catalyst to avoid thermal stress. However, it was reported by [61] that already small amounts of Helium completely destroy the crystal. This is in contradiction with our observations and indicates that the actual cryogenic setup influences this behavior. With this sample, temperature cycling between 5-10-5 K and 5-18-5 K have been performed. These measurements confirm the optical investigation that in the first case no significant difference in the crystal quality is observed, whereas in the latter case the sample is completely destroyed. The obtained Porod constant are $P_c = 14.5\,(6.57 \div 18.4) \cdot 10^{21}$ cm^{-5} and $P_c = 228\,(120 \div 300) \cdot 10^{21}$ cm^{-5} after cycling 5-10-5 K and 5-18-5 K, respectively.

- The third experiment deployed ultra-cold neutrons to measure the scattering behavior at very large wavelengths. It is very hard to measure angular distributions at these wavelengths, so a new technique with an adjustable neutron guide tube applied to allow for at least a rough measurement of the scattering distribution. The scattering information was obtained by moving the adjustable neutron guide along the flight-path, changing the acceptance of the solid angle of the detector. Only four tube positions have been measured. The complete scattering information was obtained by comparing simulation with measured data. The result confirms our model following the Porod-law, but for a complete description an additional isotropic scattering parameter has to be added, which takes into account totally reflected very long wavelength neutrons from crack surfaces. Additionally, temperature cycling for pure Deuterium was carried out and the result confirms the result from the cold neutron measurement. The most interesting results for Deuterium are given in the Table 4.4:

The result from the UCN analysis given in the Table 4.4 will be taken to the simulation of extraction of UCN from the UCN PSI pulsed source. The details will be discussed in the next chapter.

71

Table 4.4: Overview of the different samples measured in the UCN experiment. The values for 5K will be taken to the simulation of the UCN extraction.

temperature [K]	P_c [cm^{-5}]	I_c [barn]	comments
18	$(0 \div 1) \cdot 10^{21}$	2.44 ± 0.38	slowly grown
5	$(3.09 \pm 1.97) \cdot 10^{21}$	9.67 ± 0.3	slowly cooled
5	$(3.94 \pm 1.05) \cdot 10^{21}$	11.76 ± 0.38	after 5-10-5K
5	$(48, 6 \pm 3.29) \cdot 10^{21}$	33.05 ± 0.05	after 5-18-5K

Chapter 5

Simulation of UCN extraction

The simulation of the UCN extraction was based on the results from the CN, and UCN analysis. However, for the calculation of the Deuterium temperature during the proton pulse and CN flux in the moderator, results from Ref. [63] were taken. For the thermal upscattering cross section of UCN and upscattering on para-Deuterium cross sections were taken from the previous studies of solid deuterium (for details see Refs. [17, 57] and sec. 4.3). The UCN are generated inside the solid Deuterium moderator and tracked until they are lost or leave the top surface. The simulations were done for different parameters of the crystal. The result may be used as input for a storage container optimization.

5.1 Geometry of the source

The geometry of the moderator was built as an annulus with the inner diameter of 44 mm, outer diameter of 487 mm, and height $z = 160$ mm. The container contains $\sim$30 liters of solid Deuterium with mass of about 5.9 kg.

5.2 Initial parameters

5.2.1 Temperature of Deuterium during pulse

It is assumed that during the time spent by a generated UCN in the Deuterium, its temperature is constant. This is a valid approach because the time the UCN spend within the D_2, typically some 10 ms, is short in comparison with the rate of increase temperature (<0.5deg/sec). The D_2 temperatures T_f after switching proton beam on are calculated from the equation
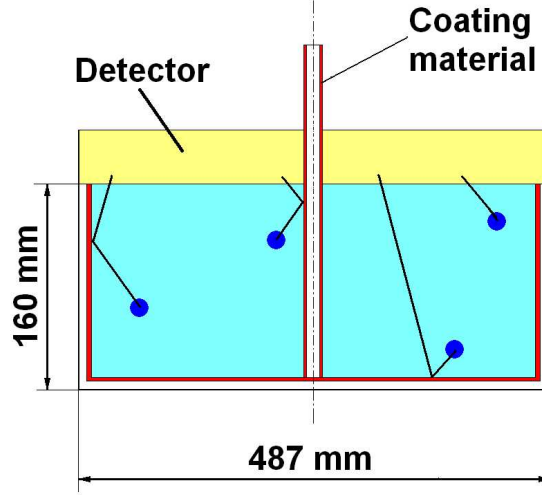
$$q = cm\Delta T \tag{5.1}$$

Figure 5.1: The picture shows the schematic view of the geometry of the moderator. The red color indicate a coating material. The UCN in the simulation are counted when they reach the detector.

where q is heat energy, c is specific heat (at low temperature proportional to T^3) and T_i initial temperature of the deuterium. The final temperature T_f is calculated as a integral of Δq from T_i to T_f and is equal:

$$T_f = \left[4 \left(\frac{I_p \cdot t_s \cdot W}{5.08 \cdot 10^{-4} \text{J/g/K}^4} + \frac{T_i^4}{4} \right) \right]^{\frac{1}{4}} \tag{5.2}$$

where I_p and t_s are scaling factors for the proton beam and time after switch it on, respectively, W is a power density and $c = 5.08 \cdot 10^{-4} T^{-3}$ J/g/K^4. The values were taken from the Ref. [63].

5.2.2 Initial momentum and energy spectrum

The applied model treats the cold neutron flux and UCN separately. It is assumed that UCN are generated by incoming cold neutrons in a downscattering process described in Refs. [7, 11]. This assumption is corroborated also by the experiment Ref. [15]. The calculated cold neutron flux in solid Deuterium (which is proportional to the generated UCN) is taken from Ref. [63] and use the formula:

$$\begin{aligned} P(z) \quad = \quad & -1.49535 \cdot 10^{-7} \text{cm}^{-4} z^4 + 5.61873 \cdot 10^{-6} \text{cm}^{-3} z^3 \\ & -8.76499 \cdot 10^{-5} \text{cm}^{-2} z^2 + 5.07419 \cdot 10^{-4} \text{cm}^{-1} z \\ & +2.37852 \cdot 10^{-3} \end{aligned} \tag{5.3}$$

The momentum of the UCN is assumed to be isotropic with UCN spectrum to be $N(v) \propto v^2 dv$.

5.3   Physical processes involved

The generated UCN are tracked until they are lost or detected at the top surface. The following processes inside the moderator were implemented in the simulations.

Losses

- Transmission of the side wall or the bottom in case the incident perpendicular UCN velocity exceeds the critical velocity v_c of the container wall (two cases have been studied: $v_c = 6.8$ m/s as for Ni, Be or DLC, and $v_c = 3.2$ m/s as for Al);

- Thermal up-scattering cross section was taken from Ref. [57] (see also Appendix B) and is the same as was used in the analysis described in sec. 4.3. The up-scattering contribution was calculated using:

$$
\begin{aligned}
\sigma_{up}(T)v &= (5.93101 - 2.16749 \text{ K}^{-1}T + 0.1819 \text{ K}^{-2}T^2 + \\
&\quad 0.01874 \text{ K}^{-3}T^3)[\text{barn m/s}]
\end{aligned}
\tag{5.4}
$$

- The para-D_2 upscattering cross section rate is:

$$
\sigma_{para}v = (1 - c_0) \cdot 2200[\text{barn m/s}]
\tag{5.5}
$$

  in accordance with Ref. [17]; where c_0 is a concentration of ortho-Deuterium.

- The Deuterium and Hydrogen absorption cross sections are equal:

$$
\begin{aligned}
\sigma_{abs_D}\ v &= 1.14[\text{barn m/s}] \\
\sigma_{abs_H}\ v &= c_H \cdot 732[\text{barn m/s}]
\end{aligned}
\tag{5.6}
$$

  where c_H is concentration of Hydrogen.

Scattering

- On collision with the side walls or the bottom UCN with perpendicular velocity component smaller than the critical velocity v_c are specularly reflected;

- Isotropic elastic UCN scattering (elastic in the sense that the UCN kinetic energy does not change because the interaction takes place with nuclei fixed in the infinitely heavy crystal) is implemented for deuterons and protons using the incoherent cross section of $\Sigma_{inc} = (4.08 + 2 \cdot c_H \cdot 82) \cdot 10^{-2} \mathrm{cm}^{-1}$;

- Small Angle Neutron scattering described by the Porod constant was taken from the UCN analysis 4.3;

- Additional incoherent elastic scattering on crystal cracks was taken from the UCN analysis (for details see sec. 4.3).

5.4 Results

5.4.1 Variation of the UCN extraction probability.

The simulations have been done for different times after switching the proton beam on. The proton beam current was in all the simulation fixed to 2 mA. The initial Deuterium temperature was set to be 5K and the UCN velocity range inside Deuterium was 0–7 m/s. The rest of the parameters (critical velocity of the coating material v_c, ortho-Deuterium concentration c_o, Hydrogen contamination c_H, Porod constant P_c, additional incoherent scattering I_c) has values appriopriate to the conditions being simulated. At the beginning the simulation has been performed for four different parameter sets called crystal A, B, C, D and the results are presented in Table 5.1.

- The crystal A was assumed to have grown from the liquid phase and slowly cooled down to 5K. The parameters for P_c and I_c were taken from the UCN analysis for the Deuterium after temperature cycling between 5-10-5K see sec. 4.3 and the parameters were equal: $P_c = 3.94 \cdot 10^{21}$ cm^{-5}, $I_c = 11.76$ barn, $v_c = 6.8$ m/s.

- The crystal B was assumed to have grown form the gas phase at 10K and then cooled down to 5K. The parameters for the $P_c = 0$ cm^{-5} and $I_c = 2.44$ barns were taken from the analysis of the nicely prepared crystal (without visible cracks) at 18K.

- The crystal C was assumed to be ideal without any cracks with $P_c = I_c = 0$. For this set of the simulation there was only ortho-Deuterium and no Hydrogen contamination ($c_H = 0$).

- The crystal D was assumed to be after temperature cycling 5-18-5K and had very bad quality, $P_c = 48.6 \cdot 10^{21}$ cm^{-5}, $I_c = 33$ barn.

Other simulations have been done only for the crystal A with a varying one of the parameter (c_H, c_0, v_c). The results are presented in the Table 5.2.

Table 5.1: Simulated extraction probabilities as a function of time after switching on the proton beam on the spallation target. The description for the crystal A, B, C, D are in the text. 50000 UCN have been generated each time.

time [s]	crystal A	crystal B	crystal C	crystal D
0	0.122	0.172	0.331	0.075
1	0.101	0.141	0.237	0.063
2	0.088	0.119	0.186	0.057
3	0.079	0.104	0.155	0.053
4	0.071	0.093	0.134	0.047
5	0.066	0.085	0.118	0.044
6	0.061	0.079	0.105	0.040
7	0.057	0.074	0.097	0.038
8	0.053	0.069	0.091	0.036

Table 5.2: Simulated extraction probabilities as a function of time after switching on the proton beam on the spallation target. The columns refer to the crystal A with one parameter changing. 50000 UCN have been generated each time.

| time [s] | crystal A | | | |
	$c_H=0.2\%$	$c_o=95\%$	$c_o=100\%$	$v_c = 3.4$ [m/s]
0	0.099	0.070	0.180	0.102
1	0.086	0.063	0.138	0.088
2	0.076	0.058	0.114	0.078
3	0.069	0.055	0.098	0.070
4	0.064	0.051	0.086	0.066
5	0.059	0.048	0.078	0.061
6	0.055	0.046	0.071	0.057
7	0.052	0.043	0.066	0.053
8	0.050	0.041	0.062	0.050

A few conclusion can be immediately drawn from the result of Tables 5.1 and 5.2.

- The Deuterium should be as pure as possible: Hydrogen contamination should be kept below 0.05%.

- The ortho-concentration should be as high as possible. More than 98.5% leads to a significant gain in UCN output, a smaller c_o has to be avoided.

- The quality of the crystal should be as good as possible, however if the temperature of the crystal is kept below 10K this influence is not as strong as contamination by Hydrogen and para-D_2.

- The moderator wall should be coated with highly reflective material with a high Fermi potential.

- The temperature of the deuterium should be kept low. The production at the beginning of the proton beam pulse of 2 mA is 2-3 times larger than after 8 s, depending on D_2 quality.

5.4.2   The origin of extracted UCN

As expected the major fraction of extracted UCN come from the upper part of the Deuterium moderator. Fig. 5.2 display the vertical z-coordinate at which escaped UCN have been generated (for a crystal A at different time after switching of the proton beam) compared to the initial distribution of all generated UCN.
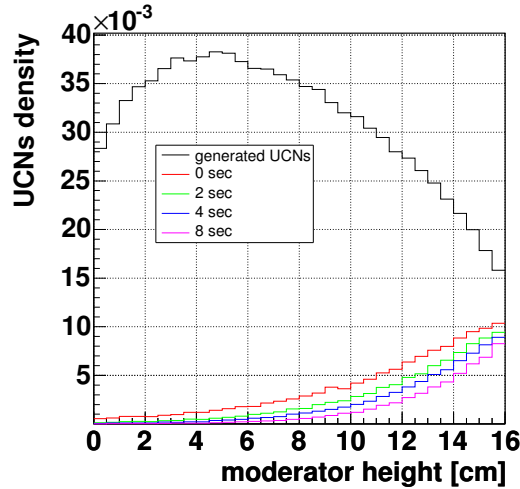

Figure 5.2: The black curve shows the initial vertical UCN distribution corresponding to the cold neutron flux distribution. The color curves show the "height of born" distribution of these UCN which were successfully extracted.

5.4.3 The distribution of escape velocity.

The next four Figs. 5.3, 5.4, 5.5, 5.6 show the 2D distribution of the escape direction and speed of extracted UCN for different time after switching proton beam off: 0, 2, 4, 8 sec, respectively. Together with 2D distribution the projections on speed and cos(θ) are presented.
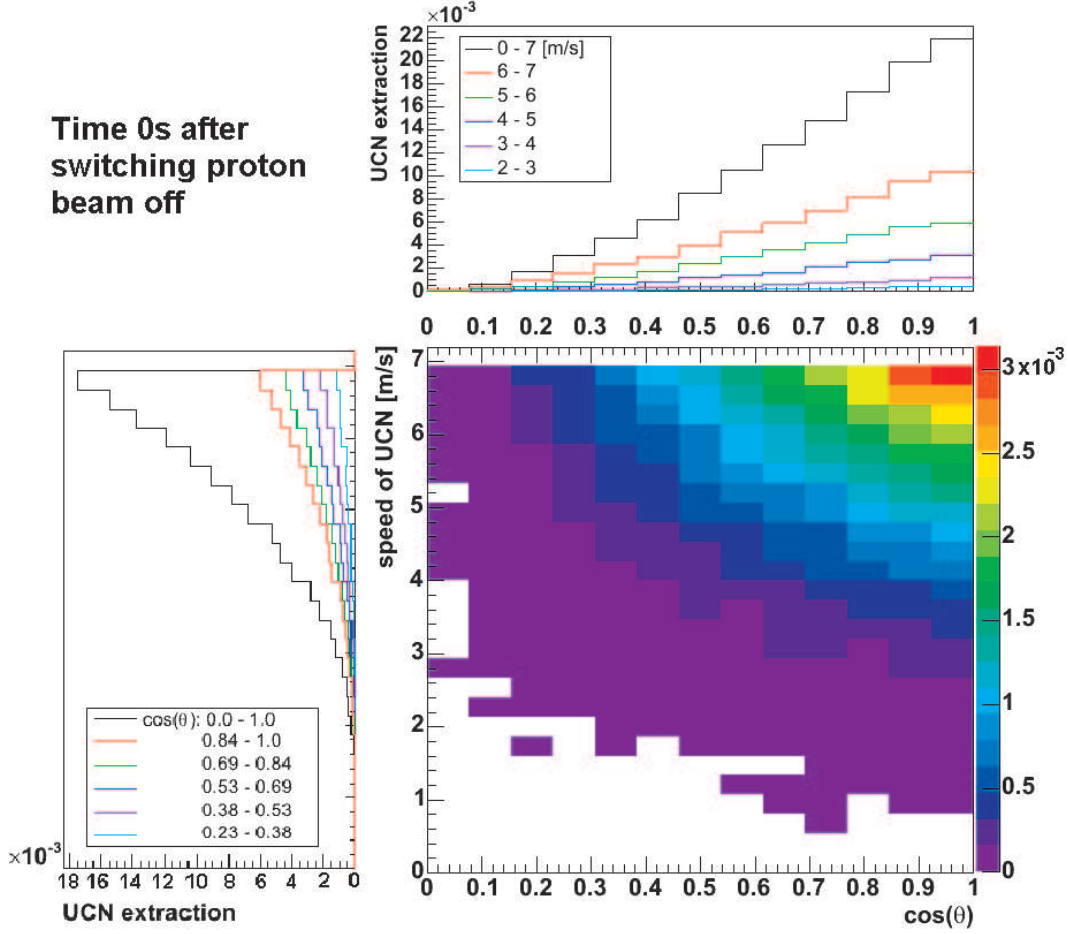

Figure 5.3: The 2D histogram shows the distribution of the escape direction and speed of extracted UCN for the time equal 0 s after switching off the proton beam. The histograms on the left and the top show the projection of the 2D distribution on X-direction (cos(θ)) and Y-direction (speed of UCN), respectively.
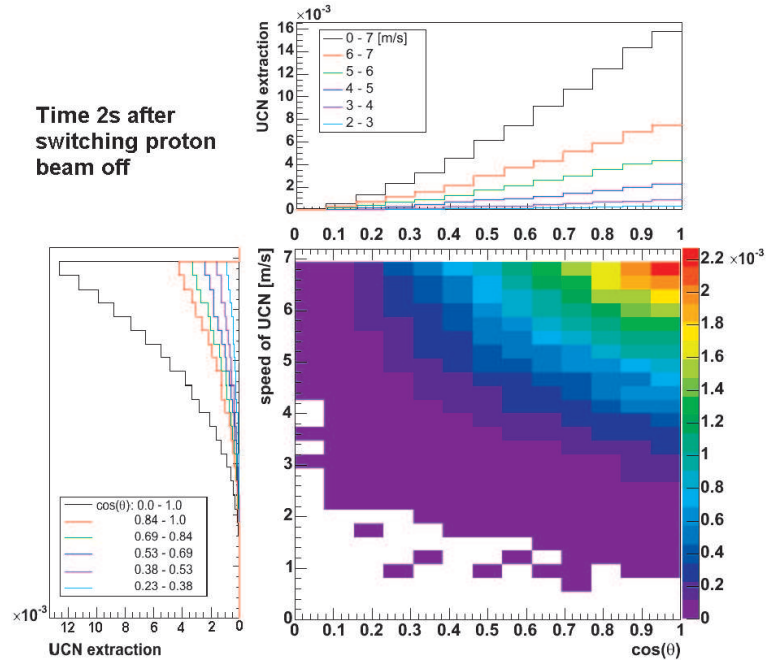
Figure 5.4: The same as Fig. 5.3 but for the time equal 2 s after switching proton beam off.
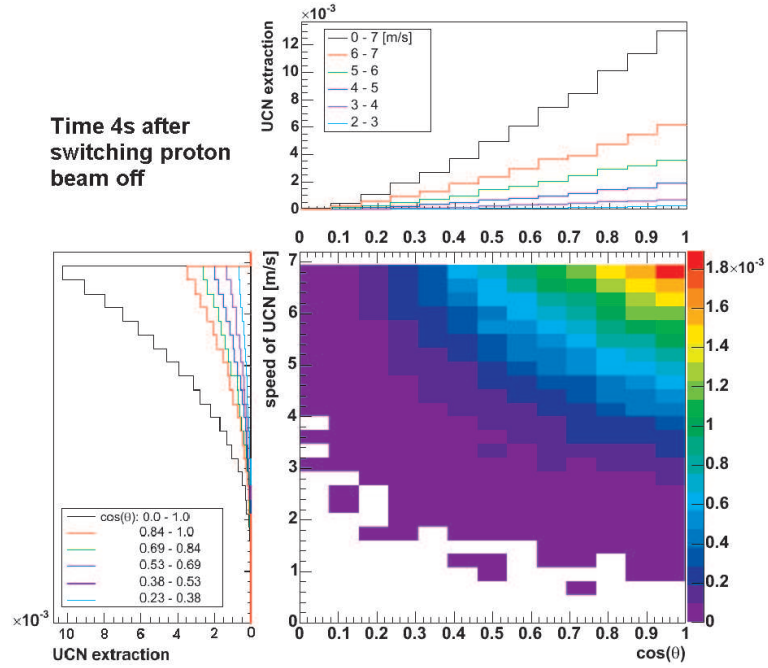

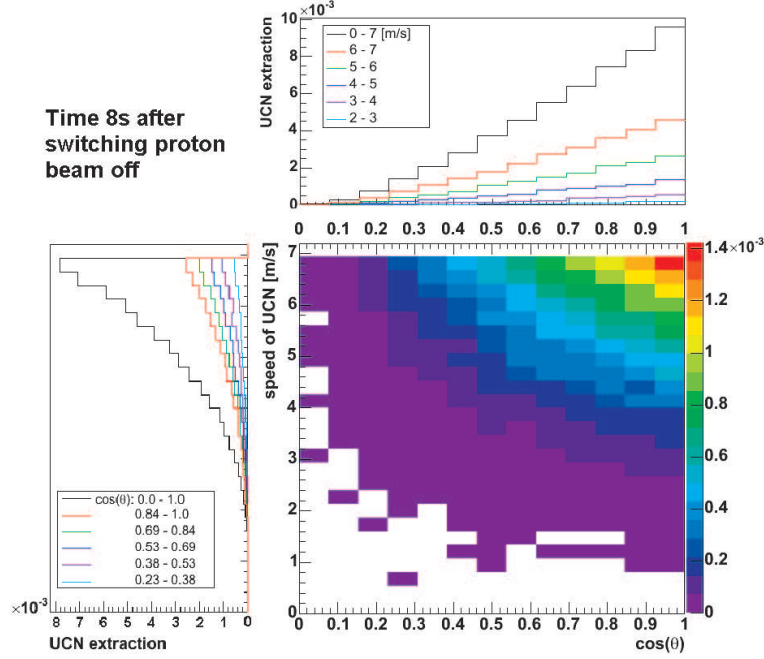Figure 5.5: The same as Fig. 5.3 but for the time equal 4 s after switching proton beam off.

Figure 5.6: The same as Fig. 5.3 but for the time equal 8 s after switching proton beam off.

The initial direction of UCN were generated isotropically. The direction of the escaping neutrons are necessarily peaked upwards, i.e. in direction of the positive z-axis and positive $\cos(\theta)$. Knudsen's Cosine-law (see [64]) states that the rate of ejection from a surface, for particles with "no memory" of how they arrived, will follow a cosine distribution independent of surface properties (like roughness). The graphs on Figs. 5.7 and 5.8 show distributions which are larger and thus suggest that UCN have some "memory". This is natural because of the built-in loss mechanisms, which give preference to shorter trajectories and thus the upward direction. To the distributions of $\cos(\theta)$ and speed of UCN the function $A_1 \cos(\theta)^{B_1}$ and $A_2 v^{B_2}$ was fitted, respectively. The results for the 0, 2, 4, 8 s after switching proton beam off are presented on Figs. 5.7 and 5.8. The uncertainties of the coefficients A_1, B_1, A_2, B_2 are always below 1% not presented on Figs. The power coefficients B_1, B_2 are independent on time when the proton beam was switched off. The coefficients A_1 and A_2 as a function on time are presented on Figs. 5.9 and 5.10, respectively.
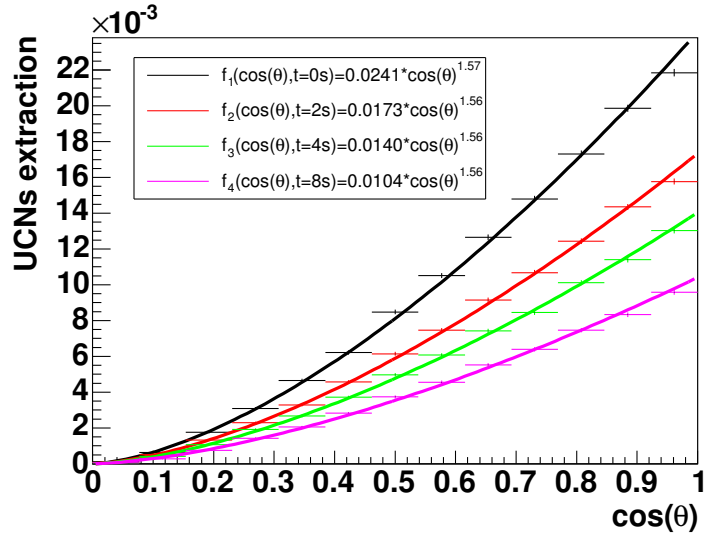
Figure 5.7: The histogram shows the distribution of $\cos(\theta)$ of the UCN escape direction with respect the vertical z-axis for different time after switching proton beam off (0, 2, 4, 8 s respectively). The lines represent the fitted functions listed in the legend. The simulation was done for parameters used in crystal A.
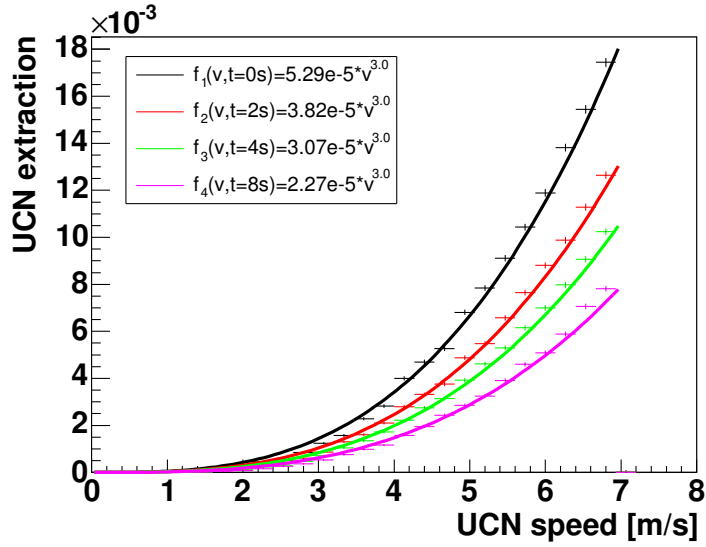

Figure 5.8: The histogram shows the distribution of speed of the UCN escape with respect the vertical z-axis for different time after switching proton beam off (0, 2, 4, 8 s respectively). The lines represent the fitted functions listed in the legend. The simulation was done for parameters used in crystal A.

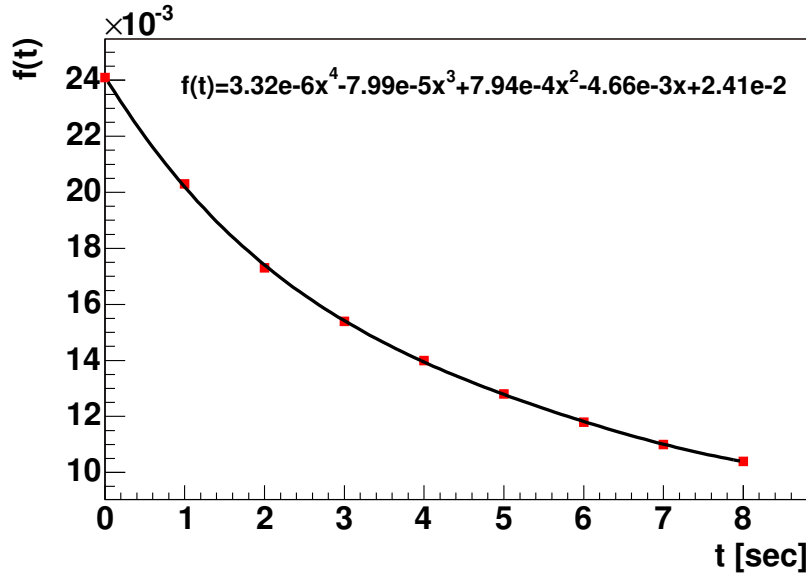$$f(t)=3.32e\text{-}6x^4\text{-}7.99e\text{-}5x^3+7.94e\text{-}4x^2\text{-}4.66e\text{-}3x+2.41e\text{-}2$$

Figure 5.9: The graph shows A_1 coefficients obtained from the fitted function $A_1 \cos(\theta)^{B_1}$ to the distribution of $\cos(\theta)$ of the UCN escape direction as a function of time after switching proton beam off. The line represent the fitted polynomial of 4th order.

$$f_\theta(t)=6.58e\text{-}9t^4\text{-}1.66e\text{-}7t^3+1.7e\text{-}6t^2\text{-}1.01e\text{-}5t+5.29e\text{-}5$$
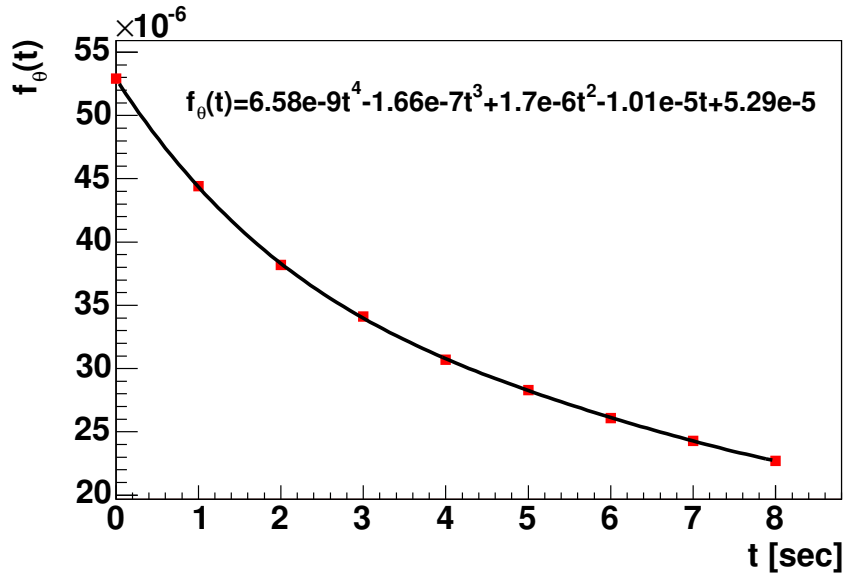
Figure 5.10: The graph shows A_2 coefficients obtained from the fitted function $A_2 v^{B_2}$ to the distribution of speed of the UCN escape as a function of time after switching proton beam off. The line represent the fitted polynomial of 4th order.

Chapter 6

Conclusion and outlook

For the construction and design at PSI of the new high intensity ultracold neutron source based on solid Deuterium at PSI, many components have to be optimized (e.g. intensity and the pulse length of the proton beam, material and size of the spallation target, UCN converter material and many others; for details see Ref. [65]).

A series of experiments have been performed to investigate the neutron scattering properties of solid deuterium which will be used as a UCN converter: (i) at the SANS I instrument at PSI with cold neutrons, (ii) at PF2 at ILL with very cold and (iii) with ultra-cold neutrons. Although the conceptual idea of these experiments was similar, a new technique was developed which for the first time allows measurement of cross sections for neutrons with energies below 1 meV. In this thesis, a description of the experiments has been given and the analysis of the scattering data is discussed in detail.

The main conclusion is that the measured scattering data can be described by the so called Porod-law ($I_{incoh} + P_c \cdot Q^{-4}$), were I_{incoh} is the incoherent elastic scattering cross section, P_c the Porod constant, proportional to the specific surface of the scattering object, and Q the momentum transfer. For neutrons with large wavelengths (> 100 Å) an additional parameter has to be added in order to properly describe the total scattering including the contribution from the scattering on cracks inside the sample. The results obtained from the three experiments are collected in tables 4.1, 4.2 and 4.3.

One further important result of the analysis was the description of the crystal after temperature cycling. Temperature cycling between 5 and 10 K did not significantly influence the optical quality of the crystal as well as its neutron scattering properties, whereas cycling between 5 and 18 K produced many cracks in the crystal resulting with increasing neutron scattering. This is an important result, as the pulsed source will be operated in a temperature range from 5 to 8 K. An increase of temperature above 10 K will produced

so many cracks that extraction of UCN decrease to about 50%. The reason of the crystal creation after temperature cycling is the 2 % density difference between 5 K and 18 K, while the density difference between 5 and 10K is only 0.2 %.

Based on our experimental results and the results obtained from Refs. [17, 56, 57, 63] a model for the description of the scattering behavior of Deuterium crystals was constructed. The model includes of the following processes:

- thermal phonon up-scattering on solid Deuterium,

- nuclear absorption on Deuterium and on Hydrogen,

- incoherent scattering on Deuterium and Hydrogen molecules,

- up-scattering on para-Deuterium (by changing the state from para- to ortho-Deuterium,

- small angle neutron scattering described by the Porod-law,

- additional scattering on cracks in the Deuterium crystal.

Based on this model, the probability for the extraction of UCN from a solid Deuterium UCN converter has been simulated. The simulation uses the simplified geometry of the PSI UCN source. The probability is calculated as a function of time starting at the beginning of the proton pulse. The number of generated UCN are proportional to the CN flux with isotropic distribution. The calculation was performed for four different crystals:

- **Crystal A**, with parameters obtained from the UCN analysis gave extraction probabilities of 0.195 immediately after switching proton pulse on and decrease to 0.054 after 8 s.

- **Crystal B**, using parameters as if the Deuterium crystal had been created from the gas phase. The Porod constant and additional scattering are expected to be like for 18K (or less). The extraction probability has 0.172 after switching proton pulse on and decreases to 0.069 after 8 s.

- **Crystal C**, an ideal crystal without Hydrogen and para-Deuterium. The para-Deuterium after several years of source operation at 10K should be converted to about 99.97 % ortho-Deuterium. The extraction probability is equal to 0.331 after switching proton pulse on and decreases to 0.091 after 8 s.

- **Crystal D**, a crystal created from the liquid phase and then cycled 5 and 18K (i.e. "destroyed" crystal). The result is equal to 0.075 at 0 s and decrease to 0.036 after 8 s.

The result of the simulation also includes the z-component of the UCN velocity and their angular distribution. These parameters can be used for simulation and optimisation of the storage tank and shutter system allowing for the calculation of the storage time, UCN density as a function of storage container dimension and material. Such a simulation can also include the guide tubes from the storage tank and can give an estimated density of UCN delivered to the experiment.

Appendix A

The extraction of results from neutron experiments often requires computer simulation. The results of the simulation, based on some theory, that best fits the data from the experiment, can be used to fix parameters of the model. There are different methods of simulation and different ways to confirm or predict the experimental results. Simulations in neutron physics mostly work on a probabilistic (Monte Carlo) approach. This uses the trajectories of many individual particles through a more or less detailed model of the experimental setup. It is clear that the procedure can become extremely involved and time-consuming when complex geometries and scattering conditions are to be handled; analytic solution may not be obtainable or may involve several approximations.

A.1 GEANT4 toolkit for ultracold simulation

The Monte Carlo simulation of the experiment has been made using an external version of the GEANT4 [22] application. This is a versatile, widely used toolkit for tracking particles through matter. Its application areas include high energy and nuclear physics experiments, medical, accelerator and space physics studies. As such, it can handle many physically possible processes, including decay and particle production. An interesting feature is that it allows the tracking of all particle and decay products, e.g. for neutron decay experiments. The GEANT4 package is designed to be easily extended to new particles and fields. This means the "technical" parts of the Monte Carlo simulation (geometry simulation, tracking, processes, fields etc.) are made using well established and tested modules.

A.2 UCN modification

The basic modifications to be made to the GEANT4 toolkit, in order to use it for simulation of UCN physics, were (i) the introduction of a new type

of particle, a neutron that is affected by gravity and (ii) the introduction of suitable potential. The full description of modifications used in Geant4 and some UCN application can be found in [66, 67, 68]. Three processes, not included in the mentioned literature were developed for scattering neutrons on solid Deuterium: (i) thermal up-scattering, (ii) small angle neutron scattering and (iii) diffuse scattering on a rough surface. The up-scattering is calculated using a Debye model for solid Deuterium similar to that used in [11, 17]. The details about the up-scattering can be found in Appendix B. The small angle scattering is calculated using the Porod approximation, valid when the momentum transfer Q goes to infinity. The model was developed in the CN analysis and the details can be found in sec. 4.1. The details about cross section calculation required by Geant4 are presented in Appendix D. Whether a UCN is reflected from the material depends on the neutron energy E, its angle of incidence θ and the Fermi potential V_F. The Fermi potential is a material property depending on its density and the averaged bound coherent scattering length [5], From this the critical velocity v_c of the material is calculated (corresponding to the maximum velocity for total reflection at normal incidence) and compared to the normal velocity component v_n. The neutron can be either reflected ($v_n < v_c$) or enters the material ($v_n > v_c$). In both cases the new direction of the neutron is calculated. For the diffuse scattering the new direction is randomized according to Gauss function. The σ of the Gauss is a roughness parameter determined from experiment. A typical value of σ for Aluminum foil was found, e.g in the experiment [62] and equal to $\sigma = 25° \pm 3°$.

One advantage of using Geant4 is that even rather complex geometries of the experiments can be easily defined and modified.

Appendix B

B.1 Result of the transmision experiment

The total scattering cross-sections for slow neutrons with energies in the range $100\,\mathrm{neV}$ to $3\,\mathrm{meV}$ for solid ortho-D_2 at $18\,\mathrm{K}$ and $5\,\mathrm{K}$, frozen from the liquid, have been measured. The $18\,\mathrm{K}$ cross-sections are found to be in excellent agreement with theoretical expectations and for ultra-cold neutrons dominated by thermal upscattering. At $5\,\mathrm{K}$ the total scattering cross sections are found to be dominated by the crystal defects originating in temperature induced stress but not deteriorated by temperature cycles between 5 and $10\,\mathrm{K}$.

We report here on measurements of neutron transmission through solid deuterium targets prepared by freezing from the liquid phase. The crystals were grown slowly (over about $12\,\mathrm{hours}$) at a temperature close to the triple point (see [43]) and then either held at $18\,\mathrm{K}$ or further cooled slowly to $5\,\mathrm{K}$. The $5\,\mathrm{K}$ crystals were also subjected to thermal cycles between 5-10 K and 5-18 K, respectively.

The measurements have been performed using cold neutrons (CN) at the SANS-I instrument [50] of the SINQ facility at PSI and with very cold neutrons (VCN) and UCN at the PF-2 instrument [69] of the ILL. The total cross-sections have been measured using the transmission technique:

$$\sigma = \frac{\ln(I_0/I)}{Nd} \tag{B.1}$$

where I_0 and I are the transmitted intensities for the target cell empty and full, N is the number density and d the thickness of the target. Neutron energy (E) measurements have been made using velocity selection and time-of-flight; E was converted to in-medium kinetic energy $E' = E - U$ (see e.g. [24]), using the Fermi potential $U = \frac{2\pi\hbar^2}{m_n} N\,b_{\mathrm{coh}} = 104\,\mathrm{neV}$ for solid deuterium with the density $N = 3.0 \times 10^{22}\,\mathrm{cm}^{-3}$ [61] and the bound coherent scattering length $b_{\mathrm{coh}} = 2 \times 6.67\,\mathrm{fm}$ [19].

The D_2 had a purity of at least 99.95%. It was prepared with a high ortho-concentration of $c_o = (98.6 \pm 0.4)\%$ using OXISORB® [44] at temperatures

around the triple point (18.7 K) as a catalyst. The c_o value was measured in situ with Raman spectroscopy of the solid deuterium [43]. The para-D_2 fraction contributes about $1/v \times (1 - c_o) \times 220$ b·m/s to the measured cross-sections (estimated using [17]). The maximum possible H-contamination $c_H = 0.0005$ contributes $c_H \times 82$ b incoherent scattering and $1/v \times c_H \times 730$ b·m/s absorption cross-section. These contributions are comparable to the absorption on deuterons ($1/v \times 1.1$ b·m/s) and close to negligible (see measured cross-sections below).

The measurements have been performed with the deuterium target at (18.2 ± 0.1) K and (5.3 ± 0.1) K, respectively. The solid D_2 densities $\rho_{18K}^{-1} = (20.38 \pm 0.02)$ cm^3/mol and $\rho_{5K}^{-1} = (19.93 \pm 0.01)$ cm^3/mol were taken from [61]. Solid angle corrections are small and range between 10^{-2} and 10^{-3}. A major experimental uncertainty is the actual target thickness d, due to using thin windows, which bulge. We used windows machined from Aluminum alloy (AlMg3/AA5754) rods to thicknesses of 150-200 μm. The windows must withstand, typically, a pressure of 1 atm against vacuum. The target thickness for flat windows is $d = 10$ mm. In the analysis effective target thicknesses were used, $d = 10$ mm for the CN and VCN data for one set of windows and $d = 11.1$ mm for the UCN data taken with another set of windows (These values are in agreement with our findings during the measurements of liquid deuterium [70]). The resulting overlap of the data sets is good, however, we estimate a common systematic uncertainty of 5-10% for the target thickness of the three individual data sets and the corresponding cross section values.

The results of the measurements for a target at 18 K are displayed in Fig. B.1 together with those from the only other solid D_2 cross section measurement made to date, for neutrons in the energy range 1.4 to 80 meV and at a temperature of 17 K, by Seiffert [71]. The two sets of results are in good agreement in the overlapping energy region below about 2 meV. Above 2 meV coherent (Bragg) scattering is possible (cut off wavelength 0.61 nm [71, 72]) but depends on details of the particular target crystal; in addition Bragg peaks are suppressed in our experiment due to the poor velocity resolution (about 10%) in the SANS measurement. Also included in Fig. B.1 is the calculated cross section taking into account thermal up-scattering and the minor contributions of up-scattering in para-D_2 and absorption (These contributions are maximal at the lowest neutron energies and there amount to an increase in cross section by 2.5%). The thermal up-scattering contribution has been calculated using a simple Debye model for solid deuterium, similar to that used by e.g. [11, 17].

The normalized phonon density of states is taken to be $Z(\omega) = 3 \, \omega^2/\omega_D^3$, where the effective maximum phonon frequency $\omega_D = k_B \theta_D / \hbar$ and the Debye temperature, $\theta_D = 110$ K [73]. At the low temperatures considered here, the
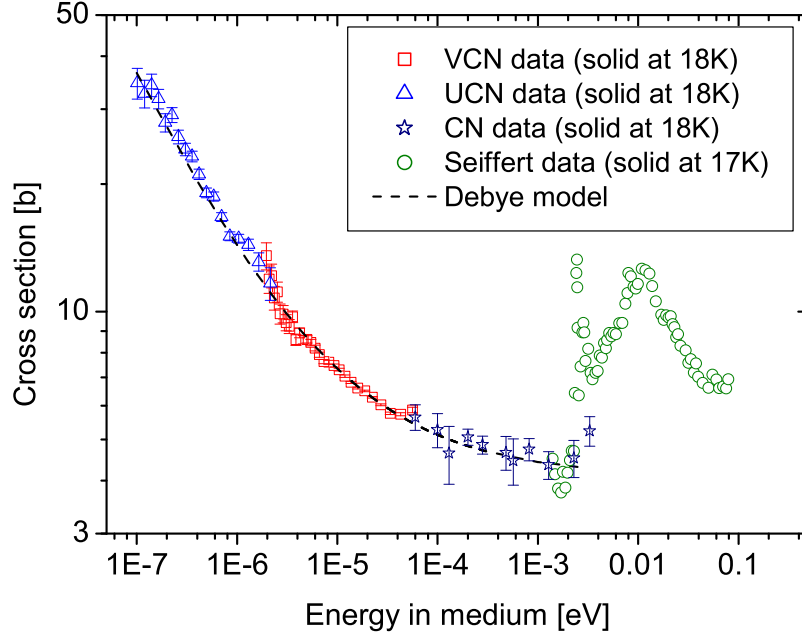
90

Figure B.1: Measured cross sections per deuterium molecule. Included in the plot is the data of [71]. The expected cross section is dominated by thermal upscattering and calculated using the Debye model.

ortho-deuterium molecule is in its ground state and spherically symmetric; it may be considered as a single particle with a bound scattering length $2\,b\,j_0(\frac{Qa}{2})$ [72] in which $b^2 = b_{coh}^2 + 5/8\,b_{inc}^2$ (following from the statistical weights of the nuclear spin configurations $S = 0, 2$ of ortho-D_2; see also [74, 75, 76]), the spherical Bessel function j_0, the distance of the deuterons in the molecule, $a = 0.74\,\text{Å}$, and the momentum transfer $Q = |\,\mathbf{k} - \mathbf{k}'\,|$, where $\mathbf{k}$ and $\mathbf{k}'$ are the wave vectors of initial state and final state of the neutron, respectively. Following [17] we use results for a cubic lattice, rather than the actual hcp structure [72], so that the single phonon scattering cross section

is written as

$$
\left(\frac{d^2\sigma}{d\Omega dE'}\right)_{inc}^{1\ phonon} = \frac{1}{2M_{D_2}}\ \left[2\,b\,j_0\left(\frac{Qa}{2}\right)\right]^2
$$

$$
\times \frac{k'}{k}\exp[-2W(\mathbf{Q})]\ Q^2
$$

$$
\times \frac{Z(\omega)}{\omega}
\begin{cases}
n(\omega)+1 & \text{if } \omega \geq 0, \text{ phonon creation} \\[2mm]
n(\omega) & \text{if } \omega < 0, \text{ phonon annihilation}
\end{cases}
\tag{B.2}
$$

The population number $n(\omega) = \left(\exp(\frac{\hbar\omega}{k_B T}) - 1\right)^{-1}$ of phonons with the frequency $\omega = \hbar Q^2/(2M_n)$ is given by Bose-Einstein statistics, while the Debye-Waller factor, $\exp[-W(\mathbf{Q})]$, with $W(\mathbf{Q}) = \frac{1}{6}\,Q^2\,\langle\mathbf{u}^2\rangle$ [32] and $\langle\mathbf{u}^2\rangle = 0.25\,\text{Å}^2$ [72] being the mean squared displacement of the nuclei, describes the zero phonon expansion of the cubic lattice. The upscattering cross section is obtained by integrating Eq. B.2 over all final energies starting from the initial neutron energy.

The good agreement between the measured and calculated cross sections for VCN and UCN is a direct validation for the scattering model, which could only be inferred indirectly from earlier measurements [13, 15]. A direct consequence of this agreement is that the deuterium crystals produced at 18 K would seem to be close to 'ideal'.

Figure B.2 shows the results for three different sets of measurements with deuterium at 5 K, (i) with very slow cooling (less than 1 K per hour), (ii) after temperature cycling between 5 K and 10 K and (iii) after temperature cycling between 5 K and 18 K: In contrast to the measurements at 18 K, the model does not describe the measured data and the way the crystal is treated dominates the results to the point where applying Eq. B.1 is no longer meaningful. The probable cause is scattering by crystal imperfections introduced by cooling from 18 K to 5 K and exacerbated by the temperature cycling.

The first evidence for this explanation is that the change in molar volume over the temperature range 5 to 10 K is 0.2% and over the range 5 to 18 K is 2% [61]: Solidifying at 18 K and then cooling to 5 K cannot avoid introducing strain and temperature cycling to 18 K involves a strain cycle a factor of 10 larger than for cycles over the temperature range 5 to 10 K. Support for this explanation comes from the similar behaviour of the light transmission of solid D_2 [43] under similar thermal treatment. Crystals produced at 18 K were optically transparent with few visible imperfections, while those
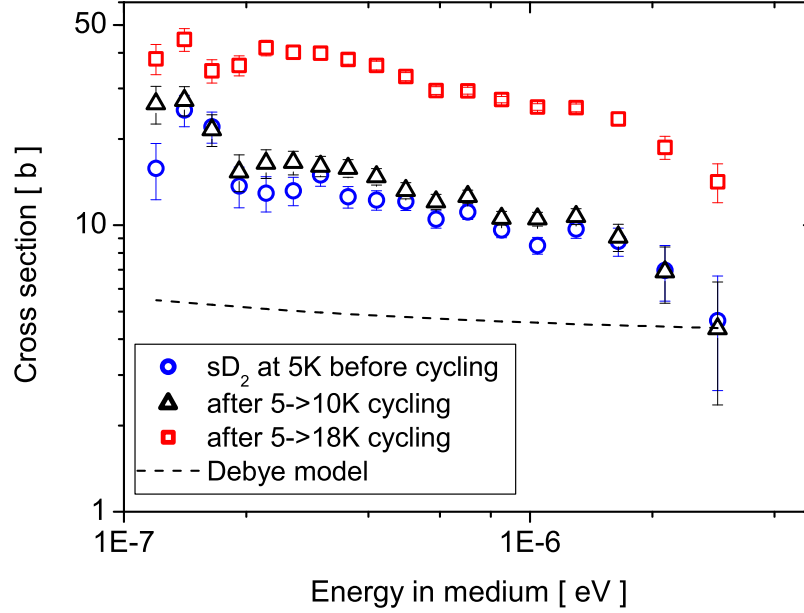
Figure B.2: Measured cross sections per deuterium molecule for UCN energies. The data sets correspond to the differently treated target crystals measured at 5 K, either after careful cool-down only, or after thermal cycles between 5 and 10 K or between 5 and 18 K. The expected cross section for the ideal crystal can obviously not describe the measured data.

cooled from 18 to 5 K were always cloudy, irrespective of the amount of care taken. Thermal cycling between 5 and 18 K results in a reduction of the light transmission by a factor of 10 compared to a 10% reduction in the case of cycles between 5 and 10 K; this is illustrated in Fig. B.3 where the measured light transmission through a solid D_2 sample over the period of a sequence of thermal cycles similar to those used in the neutron experiment is plotted. Starting with a crystal at 5 K prepared using the most careful procedures (similar to that used for case (i) of the neutron measurements), regions A and C are with the sample held at a constant temperature of 5 K, region B is a sequence of 7 temperature cycles between 5 and 10 K and region D a sequence of 7 temperature cycles between 5 and 18 K. For the larger temperature cycles some recovery of the transmission can be seen in each cycle but the trend is for a fast reduction. Sequences with 10 and more cycles showed almost the same relative transmission losses, indicating that the full reduction of transmission loss is reached after 7 or so cycles.

Although one needs to be cautious about drawing general conclusions
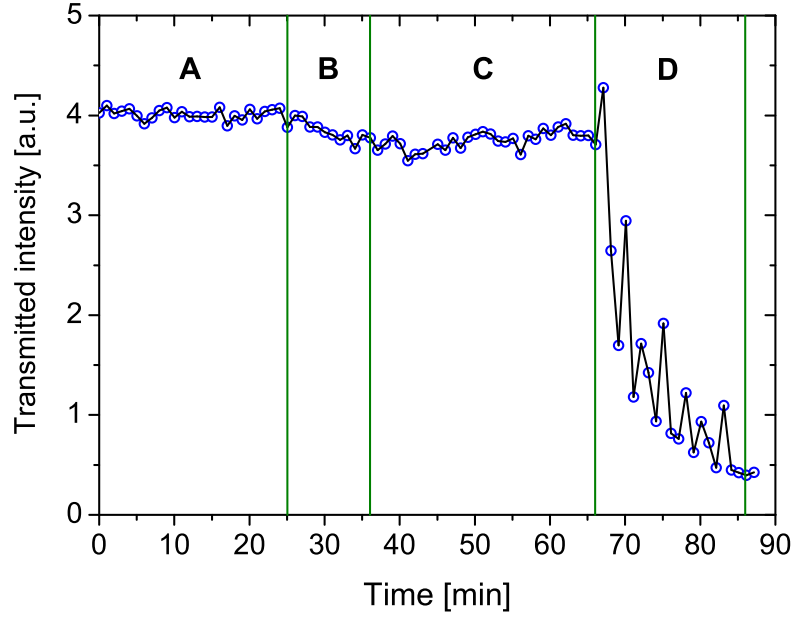
93

Figure B.3: The variation of the intensity of 488 nm light from an argon-ion laser transmitted by solid D_2 crystals subjected to a sequence of thermal cycles. See text for explanations and [43] for details of the measurement method.
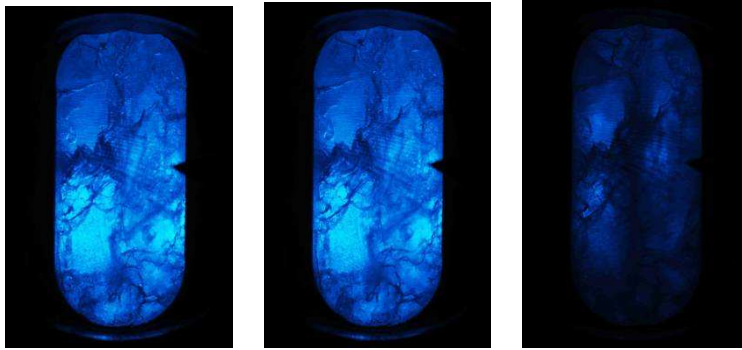

Figure B.4: The photographs show the transparency of the crystal for a nice prepared crystal at 5K (left), after temperature cycling between 5K-10K-5K (middle) and after temperature cycling between 5K-18K-5K (right). The pictures correspond to region A,C and D respectively in the Fig. B.3.

from results obtained from crystals grown in a specific target cell, the evidence is that the lowest values measured at 5 K probably set the limit for

what can be achieved with crystals prepared from the liquid phase. The best chance for producing 'ideal' solid deuterium at 5 K will be freezing directly from the gas phase to a temperature below 10 K; this was not possible with the target cell used in this experiment. Another important practical result for UCN source design from the measurements is that the solid D_2 should be kept below 10 K at all times, otherwise a systematic deterioration of the performance of the converter can result (or new D_2 crystals will have to be produced regularly if the performance of the source is to be maintained). In the case of the UCN source at PSI [77, 2], the UCN production will be in pulses of several seconds duration at 1% duty cycle. During an 8 s production pulse the temperature of the D_2 is calculated to increase from 5 to 9 K. It is re-cooled to 5 K over the next 800 s.

Appendix C

The VCN beam distribution was very inhomogeneous and wavelength dependent. Thus the measured spectrum was divided into small slices of about 4 Å each and both deconvolution and back propagation treat each slice independently. Both procedures contain uncertainties. The uncertainties were added up and treated as a systematic effect.

C.1   2D deconvolution algorithm

The Point Spread Function (PSF) describes the response of an imaging system to a point source or point object. A more general term for the PSF is a system's impulse response. The PSF in many contexts can be thought of as the extended blob in an image that represents an unresolved object. In functional terms it is the spatial domain version of the modulation transfer function. It is a useful concept in Fourier optics, astronomical imaging, electron microscopy, position sensitive detectors and other imaging techniques. The degree of spreading (blurring) of the point object is a measure for the quality of an imaging system.

The Bidim80 [53] detector used in the VCN experiment. It consists of MSCG plates with addmixture of ^{3}He in the counting gas. The charge division readout method was used to determine the neutron position. In the analysis, the deconvolution of the measured image was applied. The 2D deconvolution algorithm is based on the Point Spread Function (PSF) which was found experimentally (see sec. 4.2.1).

The flow diagram of the deconvolution algorithm is shown in Fig. C.1. At the beginning the H_{temp} is equal to the original one. Then from the H_{temp} the PSF is subtracted as seen in the Fig. C.1.

The deconvolution algorithm was not quite satisfactory (all 2D deconvolution algorithms give some uncertainties). After hundred steps of running the subtraction procedure negative counts appeared although the counts in the H_{temp} were not yet equal zero.

H$_{ORG}$- measured 2D histogram
H$_{PSF}$- 2D histogram of PSF
H$_{DEC}$- 2D deconvoluted histogram of the H
H$_{CON}$- 2D convoluted histogram of the H
H$_{TMP}$- temporary 2D histogram

H$_{TMP}$ = H$_{ORG}$

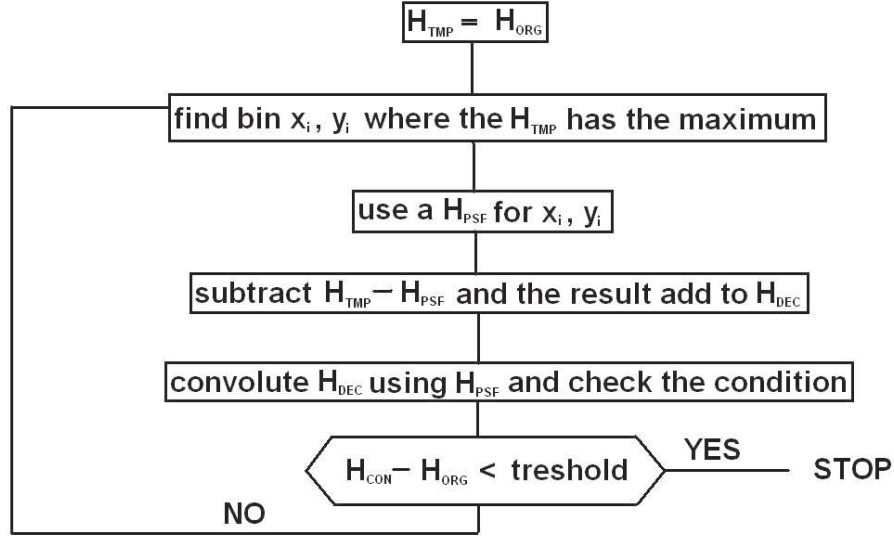find bin x$_i$, y$_i$ where the H$_{TMP}$ has the maximum

use a H$_{PSF}$ for x$_i$, y$_i$

subtract H$_{TMP}$− H$_{PSF}$ and the result add to H$_{DEC}$

convolute H$_{DEC}$ using H$_{PSF}$ and check the condition

H$_{CON}$− H$_{ORG}$ < treshold   YES ── STOP

NO

Figure C.1: The graph shows the algorithm of the 2D deconvolution using Point Spread Function.

C.2   Back propagation method

For the back propagation the simulation with Geant4 was used and consists of few steps

- Build the complete geometry of the experimental setup see Fig. 3.15.

- Track neutrons from the output of the VCN guide to the detector. The original neutrons had a homogeneous position distribution and an isotropic momentum distribution.

- Compare neutrons form the simulation with the empty cell measurement and reject redundancy. The rejection was done for each pixel of the detector separately by randomly chosen neutrons with additional condition that at the top of the VCN output guide should be more neutrons that at the bottom like it is visible in Fig. 4.14.

- The neutrons which were not rejected carry information about initial position and momentum and thus can be used as a VCN beam in the

scattering simulations.

It must be mentioned that the rejection gave only one possible solution of the initial parameters of the VCN beam. Another criteria will lead to different initial parameters and thus different parameteristion of the beam.

Appendix D

D.1   Calculation of the SANS cross section

From the CN neutron experiment the intensity of the scattered neutrons as a function of momentum transfer Q (for ortho-Deuterium at 5K) was found:

$$I(Q) \sim \frac{\mathrm{d}\Sigma}{\mathrm{d}\Omega} = A + B \cdot Q^{-4} \tag{D.1}$$

In order to find the SANS scattering cross section, Σ, the integration over full solid angle the Eq. (D.1) must be calculated. Then the macroscopic cross section can be written as:

$$
\begin{aligned}
\Sigma &= \int_0^{2\pi} \int_0^\pi \frac{\mathrm{d}\Sigma}{\mathrm{d}\Omega} \sin\theta \mathrm{d}\theta \mathrm{d}\phi = 2\pi \int_0^\pi \frac{\mathrm{d}\Sigma}{\mathrm{d}\Omega} \sin\theta \mathrm{d}\theta \\
&= 2\pi \int_0^\pi \frac{\mathrm{d}\Sigma}{\mathrm{d}\Omega} 2\sin\frac{\theta}{2} \cos\frac{\theta}{2} \mathrm{d}\theta
\end{aligned} \tag{D.2}
$$

$$Q = \frac{4\pi}{\lambda} \sin\frac{\theta}{2} \quad \Rightarrow \quad \sin\frac{\theta}{2} = \frac{Q\lambda}{4\pi} \tag{D.3}$$

$$\mathrm{d}Q = \frac{1}{2}\frac{4\pi}{\lambda} \cos\frac{\theta}{2} \mathrm{d}\theta \Rightarrow \cos\frac{\theta}{2} \mathrm{d}\theta = \frac{2\lambda}{4\pi} \mathrm{d}Q \tag{D.4}$$

Thus

$$\Sigma = 4\pi \int_0^{4\pi/\lambda} \frac{\mathrm{d}\Sigma}{\mathrm{d}\Omega} \frac{Q\lambda}{4\pi} \frac{2\lambda}{4\pi} \mathrm{d}Q = \frac{\lambda^2}{2\pi} \int_0^{Q_{max}=4\pi/\lambda} \frac{\mathrm{d}\Sigma}{\mathrm{d}\Omega} Q \, \mathrm{d}Q \tag{D.5}$$

In order to find only the small angle scattering cross section the first term in the Eq. (D.1) must be omitted. This term describes the incoherent cross section and in not connected to the SANS cross section. In the simulations this term is also separated from the SANS process.

The function described in Eq. (D.1) for the $Q \to 0$ goes to infinity. So, the special way for calculation the integral in (D.5) must be taken. We cut
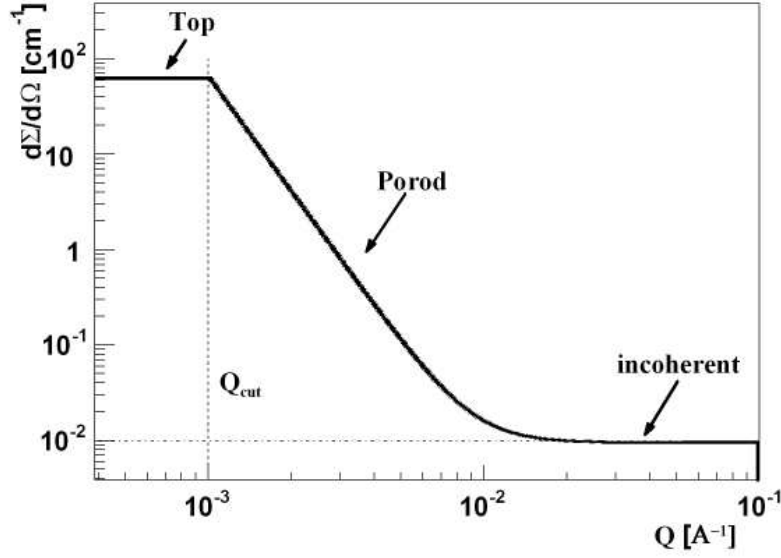
Figure D.1: The figure shows the double differential scattering cross section as a function of momentum transfer Q. The function shows the Porod behavior of the scattered neutrons. The function has three parts: (i) the Top from which the size of the scattered object can be determined, (ii) the Porod scattering and (iii) the flat incoherent scattering (equal for Deuterium 4 barn/molecule). The behavior of the scattering function below Q_{cut} is not known and was assumed to be flat (Top part).

the function in (D.1) for the $Q_{cut} = 0.001$ and the integration is calculated from the Q_{cut} to the $Q_{max} = 4\pi/\lambda$. The $Q_{cut} = 0.001$ is the last measured value form the CN experiment and below this value the exact behavior of the function is not know. However, it is known that the power of this function below Q_{cut} decrease and for some Q the function become constant. From the Q value where the function becomes constant the size of the scattered object can be determined. For the integration the simplest assumption was taken where the function $d\Sigma/d\Omega$ below the Q_{cut} is constant, as is drawn in the figure D.1.

The integration of Eq. (D.5) is now separated into two parts, the first Σ_1 from the $Q = 0$ to $Q = Q_{cut}$ and the second Σ_2 from the $Q = Q_{cut}$ to $Q = Q_{max}$:

$$\Sigma = \frac{\lambda^2}{2\pi} \int_0^{Q_{cut}} \frac{d\Sigma}{d\Omega}(Q_{cut})\, Q\, dQ + \frac{\lambda^2}{2\pi} \int_{Q_{cut}}^{Q_{max}=4\pi/\lambda} \frac{d\Sigma}{d\Omega}\, Q\, dQ \qquad (D.6)$$

The first integral Σ_1 is equal:

$$\Sigma_1 = \frac{\lambda^2}{2\pi} \int_0^{Q_{cut}} C_1\, Q\, dQ = \frac{\lambda^2}{4\pi} C_1\, (Q_{cut})^2 \qquad (D.7)$$

100

where $C_1 = \frac{d\Sigma}{d\Omega}(Q_{cut})$. The second integral Σ_2 is equal:

$$
\begin{aligned}
\Sigma_2 &= \frac{\lambda^2}{2\pi} \int_{Q_{cut}}^{Q_{max}=4\pi/\lambda} \frac{d\Sigma}{d\Omega} Q \, dQ = \frac{\lambda^2}{2\pi} \int_{Q_{cut}}^{Q_{max}=4\pi/\lambda} B \, Q^{-3} \, dQ \\
&= \frac{\lambda^2}{4\pi} B \left[(Q_{cut})^{-2} - (Q_{max})^{-2} \right]
\end{aligned}
\tag{D.8}
$$

If we put values for $Q_{cut} = 0.001\text{Å}^{-1} = 0.001 \cdot 10^8$ cm^{-1} then for solid ortho-Deuterium at 5K $C_1 = 65.7$ cm^{-1}, $B = 6.57 \cdot 10^{21}$ cm^{-5}. If $\lambda = 4\pi\text{Å} = 12.56 \cdot 10^{-8}$ cm then the $Q_{max} = 1\text{Å}^{-1} = 10^8$ cm^{-1} and $\Sigma_1 + \Sigma_2 = 1.6504 \cdot 10^{-3}$cm^{-1} The cross section for the small angle neutron scattering is then equal:

$$
\sigma = \frac{\Sigma}{\rho} = \frac{1.6504 \cdot 10^{-3} \, \text{cm}^{-1}}{0.03 \cdot 10^{24} \, \text{cm}^{-3}} = 0.055 \cdot 10^{-24} \, \text{cm}^2 = 0.055 \text{ barn}
\tag{D.9}
$$

D.2 Generation of the momentum distribution in SANS

The macroscopic cross section for the small angle neutron scattering was calculated. The obtained result is equal to:

$$
\Sigma(Q) = \begin{cases}
\dfrac{\lambda^2}{2\pi} \displaystyle\int_0^{Q_{cut}} C_1 Q \, dQ\,, & 0 < Q < Q_{cut} \\[2ex]
\dfrac{\lambda^2}{2\pi} \displaystyle\int_{Q_{cut}}^{Q_{max}} B Q^{-3} \, dQ\,, & Q_{cut} < Q < (Q_{max} = 4\pi/\lambda)
\end{cases}
\tag{D.10}
$$

A method of finding the Q distribution according to the function defined in Eq. (D.10) is the inverse transform sampling which use the cumulative distribution function (CDF) of the target random variable. Alternative methods have been devised for the cases where the CDF is not known in closed form. One such method is the rejection sampling.

According to the definition (see e.g. [78]) the cumulative distribution func-

tion of the Eq. (D.10) is equal:

$$
F(Q) = \begin{cases}
0, & 0 < Q \\[2ex]
\dfrac{1}{\Sigma}\left(\dfrac{\lambda^2}{2\pi}\displaystyle\int_0^Q C_1 Q'\,dQ'\right), & 0 < Q' < Q_{cut} \\[3ex]
\dfrac{1}{\Sigma}\left(\dfrac{\lambda^2}{2\pi}\displaystyle\int_0^{Q_{cut}} C_1 Q'\,dQ' + \dfrac{\lambda^2}{2\pi}\displaystyle\int_{Q_{cut}}^Q B Q'^{-3}\,dQ'\right), & Q_{cut} < Q' < (Q_{max} = 4\pi/\lambda) \\[3ex]
1, & Q_{max} < Q
\end{cases}
$$
$$(D.11)$$

The integration can be carried out which led to:

$$
F(Q) = \begin{cases}
0, & 0 < Q \\[2ex]
\dfrac{1}{\Sigma}\left(\dfrac{\lambda^2}{4\pi} C_1 Q^2\right), & 0 < Q' < Q_{cut} \\[3ex]
\dfrac{1}{\Sigma}\left(\Sigma_1 + \dfrac{\lambda^2}{4\pi} B(Q_{cut}^{-2} - Q^{-2}),\right) & Q_{cut} < Q' < (Q_{max} = 4\pi/\lambda) \\[3ex]
1, & Q_{max} < Q
\end{cases}
$$
$$(D.12)$$

From the Eq. (D.12) the inverse function $x = F(Q)$ could be calculated and the following result was obtained:

$$
Q = \sqrt{\dfrac{x\Sigma 4\pi}{\lambda^2 C_1}}, \qquad\qquad x < \dfrac{\Sigma_1}{\Sigma}
$$
$$(D.13)$$
$$
Q = \sqrt{\left(Q_{cut}^{-2} - \left(x - \dfrac{\Sigma_1}{\Sigma}\right)\left(\dfrac{4\pi\Sigma}{\lambda^2 B}\right)\right)^{-1}}, \quad x > \dfrac{\Sigma_1}{\Sigma}
$$

If the x numbers have the uniform distribution between $0 < x < 1$ the Q numbers will have the distribution according to the function defined in the Eq. (D.10)

102

Bibliography

[1] PSI UCN webpage, http://ucn.web.psi.ch/ .

[2] F. Atchison, M. Baumann, B. Blau et al., Proc. of the 18th Meeting of the Int. Coll. on Advanced Neutron Sources, ICANS-XVIII, Dongguan, Guangdong, R P China (2007).

[3] A. Steyerl, Phys. Lett. **B29**, 33 (1969).

[4] A. Steyerl, Nucl. Instr. Meth. **125**, 461 (1975).

[5] R. Golub, D. J. Richardson, S. K. Lamoreaux, Ultra-Cold Neutrons (Adam Hilger, Bristol 1991).

[6] R. Golub, Phys. Lett. **A53**, 133 (1972).

[7] R. Golub and K. Böning, Z. Physik B **51**, 95 (1983).

[8] I. Altarev Y. Borisov, A. Brandin *et al.*, Phys. Lett. **80A**, 413 (1980).

[9] A. Serebrov, V. Mityukhlyev, A. Zakharov et al., Sov. Phys.-JETP **62**, 785 (1995).

[10] J. Carpenter, W Yelon, Methods of Experimental Physics 23 A (Academic Press Inc., New York, 1986).

[11] Z.-Ch. Yu, S.S. Malik, R. Golub, Z. Physik B **62**, 137 (1986).

[12] A. Serebrov, V. Mityukhlyaev, A. Zakharkov et al., Nucl. Instr. Meth. A **440**, 658 (2000).

[13] C. Morris, J. Anaya, T. Bowles et al., Phys. Rev. Lett. **89**, 272501 (2002).

[14] A. Saunders, J. Anaya, T. Bowles et al., Phys. Lett. B **593**, 55 (2004).

[15] F. Atchison, B. van den Brandt, T. Brys et al., Phys. Rev. C **71**, 054601 (2005).

[16] M.Wohlmuther, G. Heidenreich, Nucl. Instr. Meth. A **564**, 51 (2006).

[17] C.-Y. Liu, A.R. Young, and S.K. Lamoreaux, Phys. Rev. **B62**, R3581 (2000).

[18] R. Golub, M. Pendlebury, Phys. Lett. **62A**, 337 (1977).

[19] V. F. Sears, http://www.ncnr.nist.gov/resources/n-lengths/, Neutron News **3**, 29 (1992).

[20] A. Serebrov, V. Mityukhlyaev, A. Zakharkov et al., PNPI preprint **2415** (2001).

[21] Los Alamos UCN collaboration, unpublished (2000).

[22] S. Agostinelli, J. Allison, K. Amako et al., Nucl. Instr. Meth. A **506**, 250 (2003).

[23] F. Atchison, T. Brys, M. Daum et al., Nucl. Instr. Meth. A **552**, 513 (2005).

[24] V. K. Ignatovich, The Physics of Ultracold Neutrons (Clarendon Press, Oxford, 1990).

[25] I. B. Khriplovich, S. K. Lamoreaux, CP Violation without Strangeness (Springer, Berlin, 1997).

[26] F. L. Shapiro, Sov. Phys. Usp. **11**, 345 (1968).

[27] V. I. Lushikov, Yu. N. Pokotilovski, A. V. Strelkov, F. L. Shapiro, JETP Letters **9**, 23 (1969).

[28] C. A. Baker, D. D. Doyle, P. Geltenbort et al., Phys. Rev. Lett. **97**, 131801 (2006).

[29] G. Ban, K. Bodek, T. Brys, M. Daum et al., http://nedm.web.psi.ch/ (2005).

[30] N. F. Ramsey, Molecular Beams, Oxford University, New York (1956).

[31] J.Pendlebury, E. Hinds, Nucl. Instr. Meth. A **440**, 471 (2000).

[32] S. W. Lovesey, Theory of neutron scattering from condensed matter, Clarendon Press, Oxford (1984).

[33] G.L.Squires, Introduction to the Theory of Thermal Neutron Scattering, Dover publications INC, New York (1996).

[34] L. Feigin, A. Svergun, Structure Analysis by Small-Angle X-Ray and Neutron Scattering, Plenum Press, New York, (1987).

[35] A. Guinier, G Fournet C. Walker et al, Small-Angle Scattering of X-Rays, New York:Wiley, (1955).

[36] I. I. Gurevich, Low-Energy Neutron Physics, North-Holland Publishing Company (1968).

[37] V. F. Sears, Neutron Optics (Oxford University Press, New York, 1989).

[38] L. Van Hove, Phys. Rev. **95**, 249 (1954).

[39] P. Schmidt, A. Rennie, O. Glatter et al, Modern Aspects of Small-Angle Scattering, Ed. by H. Brumberger (Kluwer, Dordrecht, 1995), NATO ASI Series, Ser. C 451, (1994).

[40] G. Porod, Kolloid-Zeitschrift and Zeitschrift fur Polymere **124**, 83 (1951).

[41] P. Debye, Ann. Physik **46**, 809 (1915).

[42] A. Erdélyi, (Asymptotic Expantions, New York: Dover 1956).

[43] K. Bodek *et al.*, Nucl. Instr. Meth. A **491**, 533 (2004).

[44] OXISORB is obtained from the MESSER company and in Switzerland distributed by Sauerstoffwerke Lenzburg AG.

[45] N.S. Sullivan, D. Zhou and C.M. Edwards, Cryogenics **30**, 734 (1990).

[46] D. Zhang, K.N. Jallad and D. Ben-Amotz, Appl. Spectrosc. **55**, 1523 (2001).

[47] J. V. Kranendonk, Solid Hydrogen (Plenum Press, New York, 1983).

[48] F. Atchison, P. Beaud, T. Bryś et al., Phys. Rev. **B68**, 094114 (2003).

[49] C.-Y. Liu, S.K. Lamoreaux, A. Saunders et al., Nucl. Instr. Meth. A **508**, 257 (2003).

[50] J. Kohlbrecher, W. Wagner, J. Appl. Cryst. **33**, 804 (2000).

[51] W.R.Leo, Techniques for Nuclear and Particle Physics Experiments (Springer-Verlag New York Berlin Heidelberg, 1994).

[52] P. Fierlinger, A. Pichlmaier, H. Rauch, Nucl. Instr. Meth. A **557**, 572 (2006).

[53] J. Clergeau, P. Convert, D.Feltin et al., Nucl. Instr. Meth. A **471**, 60 (2001).

[54] M. S. C. Bus, http://midas.psi.ch/mscb .

[55] The Mount John CCD image acquisition software, www.phys.canterbury.ac.nz/mjuo/astronomy_mount_john .

[56] Malgorzata Kasprzak, Diploma thesis, Jagiellonian University (2004).

[57] F. Atchison, B. Blau, B. Van Den Brandt, et al., Phys. Rev. Lett. **95** (2005).

[58] Gerbrand van der Zouw, Dissertation, Universität Wien (2004).

[59] M. Hino, M. Utsuro, Private communication .

[60] A. Serebrov, Private communication .

[61] P. Souers, University of California Press, Berkeley (1986).

[62] F. Atchison, B. Blau, M. Daum, et al., Nucl. Instr. Meth. B (in press).

[63] F. Atchison, Internal report, TM-14-02-02, Part I and II (2002).

[64] J. Pendlebury, Kinetic Theory, Adam Hilger, Bristol, 1985.

[65] http://ucn.web.psi.ch/.

[66] Peter Fierlinger, Dissertation, Universität Zürich (2004).

[67] F. Atchison, T. Brys, M. Daum, P. Fierlinger et al., Nucl. Instr. Meth. A (2005).

[68] F. Atchison, B. van den Brandt, T. Brys, M. Daum et al., Phys. Lett. B **625**, 19 (2005).

[69] A. Steyerl, H. Nagel, F.-X. Schreiber et al., Phys. Lett. A **116**, 347 (1986).

[70] F. Atchison et al., Phys. Rev. Lett. **94**, 212502 (2005).

[71] W.-D. Seiffert, Euratom report EUR 4455 d (1970).

[72] M. Nielsen and H. B. Moller, Phys. Rev. B **3**, 4383 (1971).

[73] I. F. Silvera, Rev. Mod. Phys. **52**, 393 (1980).

[74] J. Schwinger, E. Teller, Phys. Rev. **52**, 286 (1937).

[75] M. Hammermesh, J. Schwinger, Phys. Rev. **69**, 145 (1946).

[76] James A. Young, Juan U. Koppel, Phys. Rev. **135**, A603 (1964).

[77] At PSI we are presently setting up a high intensity source of UCN using solid deuterium (http://ucn.web.psi.ch/). Other efforts, known to us, are under way at Los Alamos National Laboratory, at Technical University Munich, at North Carolina State University, at Mainz University.

[78] S.Brandt, *Data Analysis* (Springer, New York, 1999).

Acknowledgements

Peer reviewed publications

Atchison F, Brys T, Daum M, et al. *Structural characterization of diamond-like carbon films for ultracold neutron applications*, Diamond and Rel. Mat. **16** 334-341 (2007).

Brys T, Daum M, Fierlinger P, et al. *Diamond-like carbon coatings for Ultracold Neutron applications*, Diamond and Rel. Mat. **15** 928-931 (2006).

Brys T, Daum M, Fierlinger P, et al. *A novel apparatus for the investigation of material properties for the storage of ultracold neutrons*, Nucl. Instr. Meth. **A** 550 637-646 (2005).

Brys T, Czekaj S, Daum M, et al. *Magnetic field stabilization for magnetically shielded volumes by external field coils*, Nucl. Instr. Meth. **A** 554 527-539 (2005).

Atchison F, Brys T, Daum M, et al. *The simulation of ultracold neutron experiments using GEANT4*, Nucl. Instr. Meth. **A** 552 513-521 (2005).

Atchison F, Blau B, van den Brandt B, et al. *Measured total cross sections of slow neutrons scattered by solid deuterium and implications for ultracold neutron sources*, Phys. Rev. Lett. 95 182502 (2005).

Brys T, Daum M, Fierlinger P, et al. *Magnetron-sputtered Be coatings as reflectors for ultracold neutrons*, Nucl. Instr. Meth. **A** 551 429-447 (2005).

Bodek K, Ban G, Beck M, et al. *Search for time reversal violating effects: R-Correlation measurement in neutron decay*, Journal of Research of the NIST 110 461-464 (2005).

Atchison F, Bodek K, van den Brandt B, et al. *Investigation of solid D-2 for UCN sources*, Journal of Research of the NIST 110 491-494 (2005).

Atchison F, Brys T, Daum M, et al. *First storage of ultracold neutrons using foils coated with diamond-like carbon*, Phys. Lett. B 625 19-25 (2005).

Brys T, Czekaj S, Daum M, et al. *Magnetic field stabilization for magnetically shielded volumes by external field coils*, Journal of Research of the NIST 110 173-178 (2005).

Brys T, Daum M, Fierlinger P, et al. *Measurement of the loss and depolarization probability of UCN on beryllium and diamond like carbon films*, Journal of Research of the NIST 110 279-281 (2005).

Atchison F, van den Brandt B, Brys T, et al. *Measured total cross sections of slow neutrons scattered by gaseous and liquid H-2*, Phys. Rev. Lett. 94 212502 (2005).

Atchison F, van den Brandt B, Brys T, et al. *Production of ultracold neutrons from a cold neutron beam on a H-2 target*, Phys. Rev. C 71 054601 (2005).

Atchison A, Baumann P, Brys T, et al. *On the use of lead/tin alloys as target material for the production of spallation neutrons*, Nucl. Instr. Meth. **A** 539 646-653 (2005).

Bodek K, van den Brandt B, Brys T, et al. *An apparatus for the investigation of solid D-2 with respect to ultra-cold neutron sources*, Nucl. Instr. Meth. **A** 533 491-504 (2004).

Atchison F, Beaud P, Brys T, et al. *Ortho-para equilibrium in a liquid D-2 neutron moderator under irradiation*, Phys. Rev. B 68 094114 (2003).

CURRICULUM VITAE

Tomasz Bryś

Prsonal:

Date of Birth:	13.12.1973
Place of Birth:	Tarnobrzeg, Poland
Nationality:	Polish

Education:

1981-1982:	Primary School nr 4, Tarnobrzeg, Poland
1982-1988:	Primary School nr 2, Tarnobrzeg, Poland
1988-1993:	Technical Secondary School, Tarnobrzeg, Poland
1988-1992:	Music School, clarinet class, Tarnobrze, Poland
1993-1999:	University of Science and Technology, Kraków, Poland, Diploma thesis: "Laboratory data acquisition system for nTRV experiment - Time Reversal Violation in nDecay", Supervisor Prof. Dr. Andrzej Kos
1995-2000:	Master Degree in Physics at the Jagiellonian University in Kraków, Poland. Specialization Computer Physics. Diploma thesis: "Fast ADC converters for Bragg detector readout". Supervisor Dr. Stanisław Kistryn
2001-2007:	PhD student at the Jagiellonian University under the supervision of Prof. Dr. Kazimierz Bodek
2003-2007:	PhD student at the Swiss Federal Institute of Technology, ETH-Zürich and Paul Scherrer Institut, under the supervision of Prof. Dr. Alexander Wokaun

111